

HARVARD UNIVERSITY  
Graduate School of Arts and Sciences



DISSERTATION ACCEPTANCE CERTIFICATE

The undersigned, appointed by the  
Department of Physics  
have examined a dissertation entitled

A Fast  ${}^7\text{Li}$ -based Quantum Simulator

presented by Jesse Amato-Grill

candidate for the degree of Doctor of Philosophy and hereby  
certify that it is worthy of acceptance.

Signature

A handwritten signature in black ink, appearing to read 'Markus Greiner', written over a horizontal line.

Typed name: Professor Markus Greiner, Chair

Signature

A handwritten signature in black ink, appearing to read 'W. Ketterle', written over a horizontal line.

Typed name: Professor Wolfgang Ketterle (MIT), Co-Chair

Signature

A handwritten signature in black ink, appearing to read 'Eugene Demler', written over a horizontal line.

Typed name: Professor Eugene Demler

Date: May 6, 2019



# A Fast ${}^7\text{Li}$ -based Quantum Simulator

A dissertation presented

by

Jesse Amato-Grill

to

The Department of Physics

in partial fulfillment of the requirements

for the degree of

Doctor of Philosophy

in the subject of

Physics

Harvard University

Cambridge, Massachusetts

May 2019

© 2019 Jesse Amato-Grill

All rights reserved.

## A Fast ${}^7\text{Li}$ -based Quantum Simulator

The work presented in this thesis is the design and characterization of a new apparatus for quantum simulation using bosonic Lithium in optical lattices, along with proposals for simulations of the spin-1 Heisenberg model and the results of initial exploratory experiments. The topic itself falls under the general category of adiabatic analog quantum computing with neutral atoms: a physical instantiation of a simple quantum mechanical Hamiltonian is built out of  ${}^7\text{Li}$  atoms near zero temperature and results are measured directly from the model system. While the techniques employed in this work are inspired by progress and discoveries in atomic physics, its applications are to the study of condensed matter systems, and similar approaches may one day be used to address a wider range of computational problems.

The strategy of adiabatic analog quantum computing comprises evolving the system through a chain of different ground states until the desired state is reached, and the structure of this thesis reflects that progression. Chapter 1 situates this work in the context of the larger effort to build computational devices, and introduces the approach followed in this work. Chapter 2 documents the design and construction of the apparatus for cooling  ${}^7\text{Li}$  to quantum degeneracy, with emphasis on the apparatus' unique features, including fast evaporative cooling and tunable magnetic bias fields with low curvature. Chapter 3 discusses the role and implementation of the optical lattice, as well as continuing efforts to characterize and mitigate decoherence mechanisms. Finally, Chapter 4 reports the results of a new lattice-based spectroscopic method for determining the strength of atomic contact interactions and further suggests how these results can be used to perform a simulation of the spin-1 Heisenberg model.

# Contents

<b>Title</b>	<b>i</b>
<b>Copyright</b>	<b>ii</b>
<b>Abstract</b>	<b>iii</b>
<b>Table of Contents</b>	<b>iv</b>
<b>Acknowledgments</b>	<b>viii</b>
<b>1 Introduction</b>	<b>1</b>
1.1 Analog Computing . . . . .	2
1.2 A <i>Quantum</i> Analog Computer . . . . .	4
1.2.1 The Heisenberg Model . . . . .	5
1.2.2 Analogs . . . . .	7
1.3 Adiabatic Quantum Computing . . . . .	9
1.3.1 Reaching a Ground State . . . . .	10
1.3.2 Transforming the Ground State . . . . .	11
1.4 Why Lithium? . . . . .	11
<b>2 Initialization</b>	<b>13</b>
2.1 Why Cooling ${}^7\text{Li}$ is Difficult . . . . .	14
2.2 Overview of the Apparatus . . . . .	18
2.2.1 Cooling and Imaging Laser System . . . . .	18
2.2.2 Chamber Design . . . . .	22

2.2.3	Coil Design . . . . .	25
2.2.4	Computer Control and Data Collection . . . . .	36
2.3	Laser Cooling . . . . .	37
2.4	Evaporation . . . . .	46
2.4.1	Magnetic Trap Evaporation . . . . .	46
2.4.2	Optical Dipole Trap Evaporation . . . . .	53
2.5	Summary of Cooling Results . . . . .	55
<b>3</b>	<b>A Platform for Simulations</b>	<b>57</b>
3.1	An Atom in an Optical Lattice . . . . .	58
3.1.1	Optical Lattice Potentials . . . . .	58
3.1.2	Wavefunctions in a Lattice: The Momentum Basis . . . . .	59
3.1.3	Wavefunctions in a Lattice: The Position Basis . . . . .	63
3.2	Many Atoms in an Optical Lattice . . . . .	64
3.2.1	The Bose-Hubbard Model . . . . .	65
3.2.2	Ground State of the Hubbard Model . . . . .	68
3.3	Lifetimes and Coherences . . . . .	74
3.3.1	Inter-band Heating Mechanisms . . . . .	74
3.3.2	Intra-band Heating Mechanisms . . . . .	82
3.4	Implementation . . . . .	84
<b>4</b>	<b>Towards Simulations of Spin-1 Heisenberg Chains</b>	<b>91</b>
4.1	Spin Models . . . . .	92
4.1.1	Effective Hamiltonians and the Two-component Bose-Hubbard Model . . . . .	92
4.1.2	Ingredients for an atomic spin-1 model . . . . .	100
4.2	Interactions in ${}^7\text{Li}$ . . . . .	103
4.2.1	Interactions on a Lattice Site . . . . .	103
4.2.2	Interaction Spectroscopy . . . . .	105
4.3	Considerations for Spin-1 Experiments . . . . .	111
4.3.1	Coherent Control and State Preparation . . . . .	111
4.3.2	Magnetic Field Stability . . . . .	112

4.3.3	Decoherence Mechanisms . . . . .	115
4.3.4	First Experiments . . . . .	117
<b>5</b>	<b>Conclusion and Outlook</b>	<b>119</b>
	<b>Bibliography</b>	<b>122</b>

# Acknowledgments

None of the work included in this thesis (nor any that has been left out of it) would have been possible without the encouragement, support, and collaboration of a number of remarkable individuals, whom I am lucky enough to call friends, mentors and family. Two physicists in particular deserve special mention: Ivana Dimitrova and Niklas Jepsen, my labmates and physics siblings. Through countless days and nights of close collaboration, they could always be counted on to join in brainstorming sessions, debugging debacles, and marathons of data-taking. They have always been the first people to celebrate my best ideas, and to graciously explicate my worst, while the combined impetus of Ivana's get-it-done attitude and Niki's perfectionism helped us scale to ever-greater heights of experimental complexity and scientific insight. Many thanks are owed to Wolfgang Ketterle, my Ph.D. research advisor, for granting me the opportunity to participate in the bleeding edge of quantum mechanics research as a graduate student, and for creating and stewarding the intellectually fertile and emotionally supportive environment in which I came of age as a physicist. He has ever been my teacher, my mentor, and my sponsor, and his unique insight into, and enthusiasm for physics and problem-solving will always continue to inspire my research and renew my curiosity.

I have been lucky to have many other close collaborators, who have spent a great deal of time discussing physics with me and a great deal of effort to help design and construct the experimental platform described in this work. I would especially like to thank David Weld, who gave me my first on-the-job crash course in experimental atomic physics; Michael Messer, whose helped the experimental build during its first year and whose energetic presence can still be felt in the lab; Yichao Yu, who even as an undergraduate provided invaluable help getting the experiment up and running, and with whom I got to share the excitement of our first  ${}^7\text{Li}$  BEC; and Will Lunden, whose

talents and effort came to our aid just at a moment when we were really struggling to master the technical challenges of working with  $^7\text{Li}$  in an optical lattice. Many thanks also to Mark Belanger, master machinist of the MIT Edgerton Shop, who nurtured my love of making things, and without whose mentorship the experimental hardware would not be nearly as sophisticated. The Harvard-MIT Center for Ultracold Atoms has been my home for many years, and my work there would not have been nearly as fruitful nor quite as fun without the many colleagues and friends from I learned and borrowed, and with whom I commiserated celebrated. Lawrence, Timur, Colin, Sebastian, the Thomases, the Borises, Tarik, Waseem, Claire, Julian, Matt, Vinay, Peter, Alex, Sepehr, and Woo Chang, thanks for all the illuminating discussions and all the laughs!

I would also like to thank David Grier, my undergraduate research advisor, for starting me on this path and for providing sage and salient advice along the way, even up to the present. And I am deeply grateful for the support and encouragement of my friends and family, including Camille and Joey, who first taught me to be curious; Shonte, who shares my opinion on nearly everything, and reassures me that I'm not completely crazy; Anik, who has patiently put up with all of my complaints about the vicissitudes of lab work and kept my spirits up; Tarun, who has shared and promoted my desire to be a well-rounded scientist; and Ben and Kelly, who took special care that I didn't work *too* hard. To all of you, a heart-felt "thank you."

# Chapter 1

## Introduction

## 1.1 Analog Computing

The work reported in this thesis concerns the design, construction and evaluation of an adiabatic analog quantum computer. Before discussing parameter requirements, tolerances, sample problems and results, it is worth taking a short detour in order to explain precisely what is meant by those words. To begin, there exist two sorts of computers: analog and digital. The former is far older, with archaeological examples dating back thousands of years, while the second has become so prevalent that it now dominates the very meaning of *computer*. As a result, the word analog has itself picked up a new meaning in this context. The Oxford English Dictionary, a venerable source of wisdom on such topics, suggests the following definitions [1]:

*adjective*

Relating to or using signals or information represented by a continuously variable physical quantity such as spatial position, voltage, etc.

*noun*

A person or thing seen as comparable to another.

and also, somewhat amusingly,

*adjective*

Not involving or relating to the use of computer technology, as a contrast to a digital counterpart.

Despite its colloquial usage, the third definition is not an entirely fair characterization. As the first two definitions might suggest, the term analog, as it applies to computing, really has two distinct meanings: analog in the sense of continuous and proportional, as opposed to discrete, and analog in the sense of analogous, as opposed to algorithmic. The former is a categorization of the underlying hardware components, while the latter is a computing paradigm. In a *stored program* computer, the internal structure of the device does not change when the computer is tasked with solving one problem or another; instead, the device iterates over a sequence of inputs stored in memory, which constitute an algorithm. The operation of an analog computer is markedly different, for the internal structure of the device reflects the structure of the problem, and must be reconfigured to model each class of problem to be solved. Given that most computers with digital components are stored-program computers and most computers built of analog parts are model-based, it is not surprising that the distinction between problem-solving paradigm and technological

implementation has been lost in the vernacular. It is nonetheless possible to have computers built of digital components, which solve problems in an analog fashion (for example, on an FPGA), and it may be possible to build stored-program computers out of analog components (such as a gate-based quantum computer) [2].<sup>1</sup>

The design of an analog computer is instead inspired by the simple but powerful idea that systems may be described by the same mathematics without actually sharing any of their physical components. For example, the New Zealand economist Bill Phillips noticed a correspondence between the set of coupled differential equations in a certain model of national economies and those describing fluid flow through a system of connected pressurized reservoirs and orifices, and the MONIAC hydrodynamic computer he designed in 1949 saw much use over the following decade, demonstrating and predicting aspects of the economy of the United Kingdom [3]. Throughout the first half of the twentieth century, there were increasingly sophisticated attempts to modularize the components of analog computers, especially in order to build general-purpose differential equation solvers. There are mechanical, electrical, and even hybrid devices which integrate, scale and differentiate their inputs, and these can be connected in series and parallel in order to perform a particular computation. At MIT, the university which hosted the work reported in this thesis, Vannevar Bush and colleagues constructed in 1923 an electromechanical “differential analyzer” that could solve systems of coupled differential equations, which proved so useful that it was soon replicated at research institutions around the world [2].

The first example of such a device, however, is an astrolabe recovered from the remains of a shipwreck off the Greek island of Antikythera. Its thirty-seven brass gears are supposed to have modeled the universe as the Greeks saw it, with stars traveling in fixed orbits around the earth, and the known planets traveling in epicycles within their own orbits. Gear ratios have nothing to do with the functioning of the heavens, even in the ancient Greeks’ perspective, and yet the device reproduced the motions of the planets while relying on completely different physical principles. The Antikythera device’s likely date of origin, c. 100 BCE, is made all the more amazing by the fact that no computer of similar complexity is thought to have been made at any time during the

---

<sup>1</sup>It can be argued, for example, that finite state machines and neural networks employing Heaviside activation functions are digital-analog computers: the nodes exist in one of two possible states, but rather than behaving as a stored program computer, they implement some functional “in hardware.” Either can, of course, be simulated on stored program computers, with significant overhead.

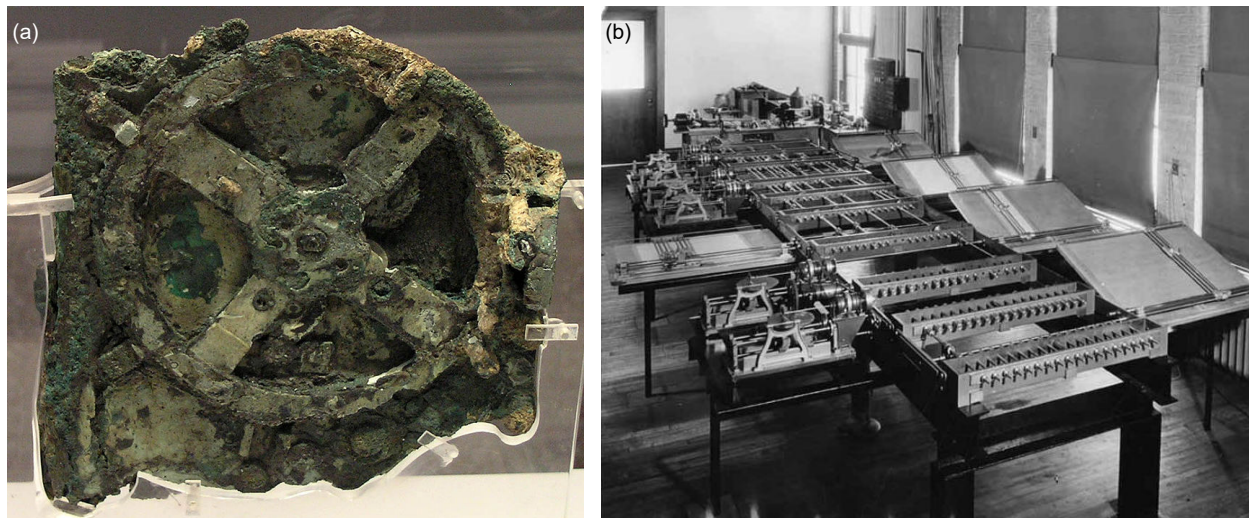


Figure 1.1: (a) A detail of the Antikythera device and (b) Bush's differential analyzer at MIT. (a) is a figure in the public domain, reproduced from [4]. (b) is reproduced courtesy of the MIT Museum archives.

following millennium [2, 5, 6]. Happening upon the device in an archaeological museum in Athens in 1980, none other than Richard Feynman was so struck with its sophistication that he wrote to his family that he had seen “among all those art objects [...] one thing so entirely different and strange that it is nearly impossible.” He concluded: “I wonder if it is some kind of fake” [7].

## 1.2 A *Quantum* Analog Computer

One year later, it was again Richard Feynman who proposed, in a landmark paper, that a computer which solved quantum mechanical problems ought to itself operate quantum mechanically *at a hardware level*— that is, that the quantum rules of one system can be used to build an analog computer which models the behavior of some other quantum system [8]. The kind of computer (or “simulator,” in the paper’s language) to which Feynman referred is one that is analog in at least the sense of proportionate. A collection of  $n$  two-level systems (or *qubits*) can exist in any superposition of  $2^n$  possible states. The existence of such superposition states is the advantage which quantum computers hold over their classical counterparts, and is the very reason that quantum computers are necessary to solve some problems in quantum mechanics. Yet the superposition state is encoded in the phase relationships between the qubits, and phase is an analog quantity. Whether this situation is fundamentally the case or not is well outside the scope of this thesis, but is nonetheless

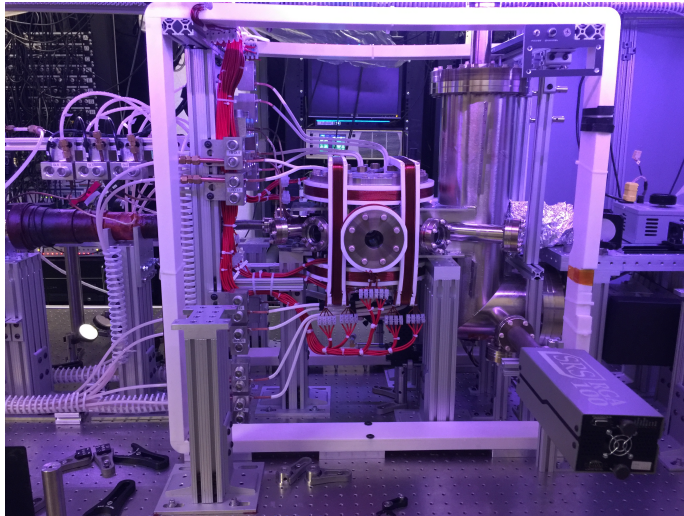


Figure 1.2: Detail of the central vacuum chamber of a modern analog computer (in fact, the one discussed in this thesis), photographed with magnetic coils installed but with all of the optics removed.

an important question: the growth of digital classical computing power has been a direct result of the fact that digital logic is implemented by using the saturated (i.e. digital) regime of transistors, which relaxes manufacturing tolerances enough to allow for the creation of billions of microscopic, logical (that is, error-free) bits on a single device. At least for now, the development of quantum computers lacks this distinct advantage. While in principle it is possible to design a stored-program computer out of analog qubits (and such an approach is being actively pursued), the manufacturing tolerances remain tight enough that it is not yet possible to create meaningfully large numbers of logical qubits [9]. It is also possible, however, to have the qubits interact directly, via physical processes that are analogs of the processes in the system to be modeled. That is the approach followed in this work, and it is therefore in the spirit of the Antikythera device and of Feynman's proposal that the apparatus described in the next chapter was conceived.

### 1.2.1 The Heisenberg Model

While the apparatus is intended to be a multi-purpose platform for quantum simulation with bosons in optical lattices, it will prove useful to keep in mind a particular quantum problem to be solved, in order to provide context for the design and to begin to evaluate its capabilities. One such class

of quantum problems involve the spin-spin interaction

$$H = \sum_{\substack{i,j \\ \sigma=x,y,z}} J_{ij}^{\sigma} S_i^{\sigma} S_j^{\sigma} , \quad (1.1)$$

where  $\mathbf{S}_i$  is a three-dimensional spin vector with components  $S^{\alpha}$  located on a lattice site  $i$ , and  $J_{\alpha}$  is a potential energy which in general depends on the distance between sites  $i$  and  $j$ . This deceptively simple *Heisenberg Hamiltonian* features an incredible range of ground states and excitation spectra. Depending on the sign of  $J$  (which reflects the quantum statistics of the particles and whether the interactions between them are attractive or repulsive), the coupling may be ferromagnetic or anti-ferromagnetic, leading to magnetically ordered ground states with gapless excitation spectra of spin waves. In a square lattice, the anti-ferromagnetic ground state is predicted and observed to have extremely shallow overlap with the classical anti-ferromagnet, due to quantum fluctuations[10, 11]. The magnetic order may be frustrated, leading to glassy phases, depending on the coordination number of the lattice, and also on whether the interactions are long range or restricted to nearest neighboring sites. Anisotropy in the exchange coupling leads to competition and ultimately phase transitions between ordering on different axes. Not least surprising is the prediction that for integer-spin particles in one dimension, the Heisenberg model features a gapped ground state with string order in the bulk and degenerate edge states, which is not what one would expect from mean field calculations— i.e., a magnetically ordered state, as is found in spin-1/2. This prediction, first made by Duncan Haldane in 1983 [12], suggests that the ground state of the spin-1 Heisenberg model is one of the simplest examples of a symmetry protected topological state, featuring order that is robust against perturbations that preserve the symmetry of the Hamiltonian [13].

With the addition of simple extra terms, the Heisenberg model can further describe a vast array of real-world behaviors. For example, with the addition of tunneling between sites, it captures the essential behaviors of electrons in strongly interacting materials, and can serve as design guides for materials with novel properties, such as high temperature superconductors[10, 11, 14–16]. It has also been shown that problems in the difficulty class NP map to a subset of the Heisenberg model with exchange coupling only between the  $z$ -component of the spins and with additional tunable bias fields on each site, i.e. the quantum Ising model [17, 18]. While some of these variations are solvable in certain parameter regimes on classical digital hardware, analog quantum hardware— such

as the ultra-cold atoms platform presented here— offers a unique opportunity to directly simulate the most intractable cases.

### 1.2.2 Analogs

The work described in this thesis rests on many analogs— physical systems that are made of different parts, or whose parts are arranged differently, but whose behavior is comparable in some way. The components out of which this computer can be built—in effect, the analogs— are the interactions of the atoms with electromagnetic fields (both DC and AC, resonant and far-detuned) and interactions between the atoms themselves. This section is intended to provide a flavor of these analogs and suggest how they may be used to simulate the Heisenberg model and other models like it; each will be described in greater detail later on.

#### Phase space density

It is often said that quantum mechanics is the physics of the very small. This is only part of a larger truth: it is the physics of the very small *or* the very cold. The essence of this statement is captured by the thermal de Broglie wavelength

$$\lambda_T = \frac{h}{p} = \frac{h}{\sqrt{2\pi m k_B T}}, \quad (1.2)$$

which shows how the size of the wavefunction of a particle will increase with decreasing temperature (or kinetic energy).<sup>2</sup> It is the overlap of the wavefunctions which determines the behavior of quantum particles, characterized by the phase space density

$$\rho = n\lambda_T^3. \quad (1.3)$$

where  $n$  is the number density of particles. Thus there is already reason to suspect that the behavior of electrons in a solid packed at  $10^{21} \text{ cm}^{-3}$  near the Fermi temperature  $T_F \approx 10,000 \text{ K}$  is as strongly influenced by quantum effects as is the behavior of dilute clouds of atoms, with densities of  $10^{13} \text{ cm}^{-3}$  and cooled to within 100 nK of absolute zero.

---

<sup>2</sup>Assuming there are no internal degrees of freedom.

## Conservative external potentials

The potential energy landscape experienced by the atoms is crafted using a combination of DC magnetic fields and off-resonant light, both of which exert conservative forces. While these provide the trapping geometries needed to initially confine and cool the atoms, they are also responsible for implementing the external potential of a model Hamiltonian. For example, a far-detuned standing wave of light with wavevector  $\mathbf{k} \equiv 2\pi/\lambda\hat{z}$  creates an AC Stark shift potential proportional to  $\sin^2 kz$ , which mimics the Coulomb potential of the lattice of nuclei in a solid material, at least in the tight binding approximation. As a result, the dynamics of an atom in such a standing wave are described by the same band structure model as a tightly bound electron moving in a real crystal (see section 3.1.1).

## Pseudospin

The spin-1/2 variant of the Heisenberg Hamiltonian introduced in the previous section describes the behavior of quantum mechanical particles which can exist in one of two possible states, or a superposition between the two. At least in the absence of interactions between the states (i.e. in a single-particle picture), these states might as well be any quantum mechanical two-level system with a driving term. The description of the system would be the same if it were two hyperfine states connected by an RF transition, or two electronic states connected by an optical transition. The descriptive equivalence of isolated two-level systems even extends to *external* states the particles, such as localization in two potential wells connected by tunneling (e.g. in [19]). The same argument applies in general to  $n$ -level systems.

## Interactions

Unlike electrons in a solid or magnetic dipoles, neutral atoms do not have any long-range interactions. At most, the electronic polarizability that arises from admixing the spherically symmetric electronic ground state with higher angular momentum orbitals gives rise to an induced dipole-dipole, or van der Waals interaction. The strength of this interaction scales as  $1/r^6$ , and can effectively be treated as a contact interaction in dilute atomic systems.<sup>3</sup> Despite neutral atoms'

---

<sup>3</sup>The effective range of this interaction can, however, be dramatically increased by promoting the outermost electron to a highly excited, or *Rydberg* state [20]. This approach, distinct from the work discussed in this thesis,

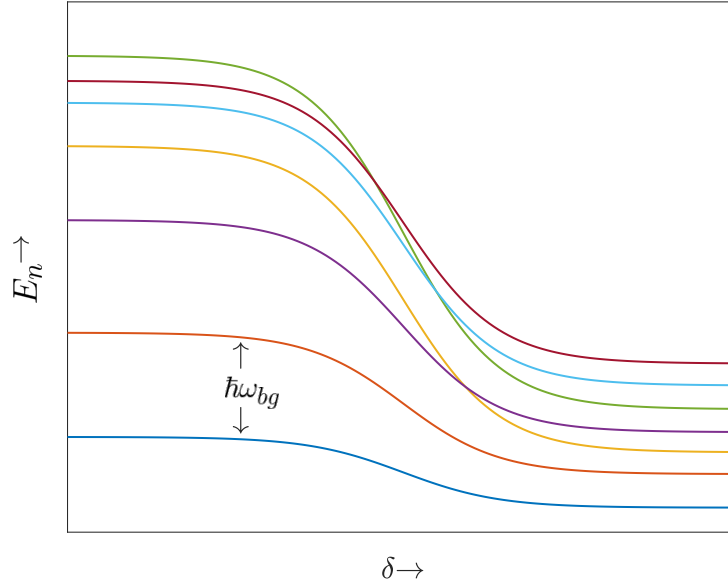


Figure 1.3: Adiabatic state preparation

lack of long-range interactions, it is possible to implement exchange interactions of the type featured in the Heisenberg Hamiltonian by arranging the system so that the pseudospins can *physically* exchange places. This *super-exchange* process [23] is discussed in greater detail in section 3.2.2.

### 1.3 Adiabatic Quantum Computing

A computing device intended to find the ground state of some quantum mechanical Hamiltonian requires both a way to implement the model, and a way to reach the ground state. The strategy of adiabatic quantum computing is to perform all the cooling necessary to reach degeneracy in some system where cooling is easy, and then evolve the system into a system of interest [24, 25]. For example, a system amenable to cooling may feature large bandgaps, increasing the critical temperature, or may have a small number of degrees of freedom that easily exchange entropy. The target system may inhabit a much larger Hilbert space, the low energy portion of which is interesting but difficult to reach because of small energy gaps or entropy distributed between different, uncoupled sectors. Under certain conditions, it is possible to create the ground state of the target system by creating the ground state of the original system, rather than by attempting to cool directly into the ground state of the target system.

---

comes with its own set of trade-offs and is an area of active research and development [21, 22].

Consider the Hamiltonian

$$H = (1 - \delta) \cdot H_1 + \delta H_2 \quad (1.4)$$

whose ground states are protected by a bandgap  $\hbar\omega_{bg}(\delta)$ . As long  $H_1$  does not commute with  $H_2$ , it is possible to vary  $\delta$  in such a way that a system which starts in the quantum mechanical ground state of  $H_1$  when  $\delta = 0$  *remains* in the ground state for all  $\delta$  (figure 1.3). The adiabatic theorem supplies the speed limit, which is that  $\omega_{bg}$  should vary slowly enough to prevent Landau-Zener transitions out of the ground state:

$$\left| \frac{\partial \omega_{bg}(t)}{\partial t} \right| \ll (\omega_{bg}(t))^2 . \quad (1.5)$$

This condition is fulfilled by a exponential ramp of  $\omega_{bg}$  with a time constant that depends on the difference between the initial and final bandgaps. For systems with small bandgaps, this can take a very long time; nonetheless, it provides a something of a side door into what may prove an otherwise inaccessible ground state.

### 1.3.1 Reaching a Ground State

In order to make use of this scheme, it must be possible to produce the ground state of some quantum system— that is, to make it Bose- or Fermi-degenerate, depending on the quantum statistics of its components. In 1995, it was shown by Eric Cornell and Carl Wieman [26] and by Wolfgang Ketterle [27] that it is possible to create the quantum ground state of a dilute gas of composite bosons (atoms with integer total spin), via a combination of laser cooling and forced evaporative cooling in a conservative potential. The critical temperature for this phase transition can be derived in the context of the Grand Canonical Ensemble [28] by considering the difference between the total number of atoms  $N$  and the number of condensed atoms  $N_0$ :

$$N - N_0 = \int_0^\infty dE \frac{g(E)}{\exp[\beta(E - \mu) - 1]} , \quad (1.6)$$

where  $g(E) = 0.5 E^2 / (\hbar\bar{\omega})^3$  is the density of states in a harmonic trap with geometric mean trap frequency  $\bar{\omega} \equiv (\omega_x\omega_y\omega_z)^{1/3}$ , and the denominator is the Bose-Einstein distribution function for energy  $E$ , chemical potential  $\mu$  and inverse temperature  $\beta = 1/(k_B T)$ . When  $\mu = 0$ , none of the  $N$

atoms are in the condensed state, leading to the relation

$$N = \left( \frac{k_B T}{\hbar \bar{\omega}} \right)^3 \text{Li}_3 [\exp(\beta \mu)] \quad (1.7)$$

and a critical temperature of

$$k_B T_c \approx 0.94 \hbar \bar{\omega} N^{1/3}, \quad (1.8)$$

which works out to be about 500 nK for  $10^6$   ${}^7\text{Li}$  atoms in a 100 Hz spherical trap. The condensed fraction is  $N_0/N = 1 - (T/T_c)^3$ , so that a 99% pure condensate requires  $T/T_c \approx 1/5$ . Chapter 2 will describe a new apparatus and strategy for producing a Bose-Einstein condensate (BEC) of  ${}^7\text{Li}$  atoms, as a starting point for adiabatic state preparation of eigenstates of spin models.

### 1.3.2 Transforming the Ground State

The strategy of adiabatic quantum computing suggests that these massively occupied quantum degenerate systems can be used as a computational resource. By ramping on a three-dimensional optical lattice, for example, one transforms the external confinement of the trap into a grid of approximately harmonic traps connected by tunneling, which introduces a band structure, and simultaneously increases the on-site interactions relative to other energy scales in the system by squeezing the atomic wavefunctions. In precisely this way, it is possible to transform a superfluid BEC— the ground state of many weakly-interacting atoms in a large harmonic trap— into a Mott Insulator, which is rather the ground state of a strongly interacting system in a periodic potential [29, 30]. While the final ground state looks nothing like the original ground state, it is nonetheless possible to connect them adiabatically by turning up the strength of the lattice at an appropriate rate. This very step will be the first in a chain of several such adiabatic transitions proposed in this work, which connect a single-component BEC to the ground state of the spin-1 Heisenberg spin chain.

## 1.4 Why Lithium?

Despite the fact that  ${}^7\text{Li}$  was one of the first atoms to be cooled to degeneracy (after Rb and Na) [31], it has not, to this author’s knowledge, been previously used in a lattice-based quantum

simulator. The difficulties both in cooling lithium to degeneracy, discussed further in chapter 2, and in keeping it cool in a lattice, discussed in chapter 3, may both be contributing factors. The fundamental motivation to use  ${}^7\text{Li}$  in an adiabatic quantum simulator, however, is the enabling features it brings to simulations of strongly interacting systems. Firstly, the Feshbach resonances within and between hyperfine states of  ${}^7\text{Li}$  [32–36], discussed in detail in chapter 4, mean that the inter- and intra-state interactions vary with respect to one another as a function of the external magnetic field. For example, for some states  $a$  and  $b$  and characteristic interaction energy  $U$ , the ratio  $U_{aa}(B)/U_{bb}(B)$  may vary between  $\pm\infty$  as a function of the magnetic field  $B$ . This tunability will prove to be instrumental in transforming the system being modeled between different ground states.

Secondly, the Hamiltonian description of atoms in optical lattices is made dimensionless when all distances are in units of the lattice spacing  $\lambda/2$  and all energies are in units of the atomic recoil energy  $E_R \equiv \hbar^2 k^2 / (2m)$  (see section 3.2.1 for a full derivation), which means that all temperature and timescales vary as the inverse of the atomic mass. The particle exchange coupling introduced in the previous section therefore generates dynamics which are faster in Lithium than in nearly any other atom; for example, particle exchange is enhanced by about a factor of ten compared to what can be achieved with  ${}^{87}\text{Rb}$ , and the ground state in a lattice is protected by a bandgap ten times larger. In principle, choosing a light atom is extremely beneficial in overcoming the time constraints imposed by technical sources of heating that might cause a system to leave its ground state during an adiabatic sweep.

## Chapter 2

# Initialization

## Making a ${}^7\text{Li}$ BEC

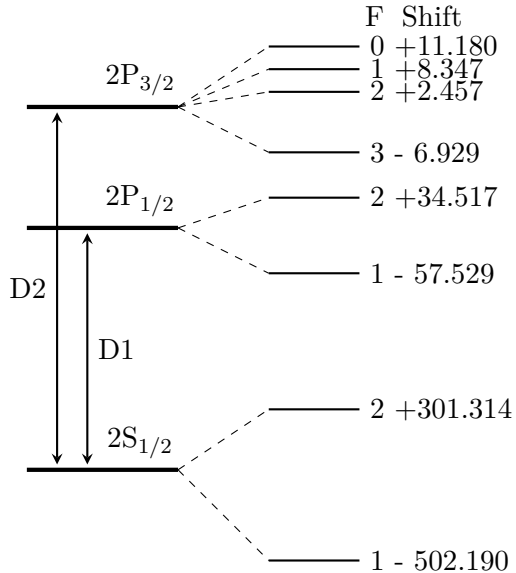


Figure 2.1: Hyperfine structure of  ${}^7\text{Li}$ . Shift frequencies are given in megahertz. The center of gravity of the D1 and D2 transitions are 446,800,132.006 MHz and 446,810,184.005 MHz respectively (D-line data taken from [37]). The natural linewidth  $\Gamma = 2\pi \times 5.87$  MHz [38].

## 2.1 Why Cooling ${}^7\text{Li}$ is Difficult

Despite the advantages  ${}^7\text{Li}$  offers for quantum simulation, several of its unique features constrain both the design of the apparatus and the path to degeneracy.  ${}^7\text{Li}$  was the third atomic species in which Bose-Einstein condensation was demonstrated, and then only after overcoming significant (and unforeseen) difficulties [31]. The particular challenges posed by cooling these atoms are described in this section.

### Nearly-degenerate ${}^2P_{3/2}$ hyperfine levels

Unlike most other alkali elements, the hyperfine levels of the  ${}^2P_{3/2}$  excited state of  ${}^7\text{Li}$  are separated by less than a natural linewidth (see figure 2.1). This coincidence of atomic structure has two consequences. Firstly, the transition which would usually provide the cooling and trapping in a magneto-optic trap (MOT) is not closed, as a transition to the  $F' = 2$  manifold is almost as likely as the transition to  $F' = 3$  and the former can decay to the  $F = 1$  manifold in the ground state. As a result, nearly as much power is necessary on the transition out of  $F=1$  in the ground state as out of  $F=2$  (hereafter, these transitions will be referred to as F1 and F2), rendering nearly pointless the usual labels of “repumping” and “cooling” light, although for convenience the convention is

maintained here. This condition requires extra laser amplifiers and forces the repumpers to be configured as cooling beams. The second consequence of the excited state hyperfine structure is that it precludes the use of standard sub-Doppler cooling techniques using the D2 transition, which rely on coherences within hyperfine levels and thus on the distinguishability of the excited state manifold. Fortunately, the two hyperfine levels of the  $^2P_{1/2}$  state are separated by nearly  $16\Gamma$ , which leaves the D1 line as an option for sub-Doppler cooling.

### Small and attractive triplet scattering length

The strength of the scattering process between two low-temperature atoms is characterized by a scattering length  $a$  [39, 40]. This length scale arises from considering the asymptotic form of the wavefunction in the relative coordinate  $r$  and reduced mass  $\mu$ :

$$\psi(\mathbf{r}) \propto e^{ikz} + f(\theta) \frac{e^{ikz}}{r}, \quad (2.1)$$

where the first term describes an incoming plane wave in the  $\hat{z}$  direction, and the second term describes a spherical wave scattered off the spherical atomic potential  $V(r)$ . The symmetry of the outgoing wave can be used to write an expansion in terms of spherical waves with angular momentum  $l$

$$f(\theta) = \sum_{l=0}^{\infty} (2l+1) \left( \frac{e^{2i\delta_l} - 1}{2ik} P_l(\cos\theta) \right), \quad (2.2)$$

where  $P_l(\cos\theta)$  are the Legendre polynomials and  $\delta_l$  is the spatial phase shift added by each partial wave. At temperatures below which the kinetic energy of the atom  $E_{\text{kin}} = \hbar^2 k^2 / (2\mu)$  does not overcome the centrifugal barrier  $V_{\text{eff}} = V(r) + \hbar^2 l(l+1) / (2mr^2)$ , only the  $l=0$  partial wave contributes to the scattered wavefunction. This limit is safely reached for all the collisions considered in this work. It can then be written that

$$f(\theta) \approx \frac{e^{2i\delta_0} - 1}{2ik} = e^{i\delta_0} \frac{\sin(kr + \delta_0)}{kr}, \quad (2.3)$$

while scattering length is defined by

$$a = - \lim_{k \rightarrow 0} \frac{\tan \delta_0(k)}{k}. \quad (2.4)$$

In  ${}^7\text{Li}$ , this scattering length  $a$  is approximately  $-27a_0$ , where  $a_0$  is the Bohr radius [41]. This relatively small magnitude (three times lower than  ${}^{87}\text{Rb}$ ) limits the scattering cross-section  $\sigma = 8\pi a^2$ , which in turn limits the two-body collision rate  $n\sigma v$ . Thermalization in a trap depends on elastic collisions, so evaporative cooling proceeds more slowly in the case of small scattering length. One can attempt to mitigate this issue by compressing the cloud to high densities, e.g. by using a magnetic quadrupole trap.

The sign of the interactions further requires that Bose-Einstein condensation take place in the vicinity of a Feshbach resonance, so that the interactions can be made repulsive and the condensate prevented from collapsing. As the Feshbach resonances of  ${}^7\text{Li}$  are found at magnetic fields above 700 G, one must work at high magnetic field, requiring large magnetic coils placed near the atoms and ruling out the use of a magnetic quadrupole trap for condensation.

### Temperature-dependent zero-crossing of the scattering cross-section

The difficulties caused by the small magnitude of the background scattering length are compounded by the fact that atoms with negative background scattering lengths exhibit a zero-crossing of the two-body cross-section as a function of temperature. It is straightforward to see where this effect comes from in the context of scattering off a rectangular well potential of depth  $V_0$  and width  $R$  (the same argument applies to the pseudopotential that more closely describes the interactions of neutral atoms) [39]. The wavefunction at  $r > R$  is proportional to the scattered wavefunction (2.3), while inside the potential

$$\psi_{\text{in}} \propto \sin k'r \tag{2.5}$$

for  $k'$  determined by  $E - V_0 = \hbar^2 k'^2 / (2m)$ .<sup>1</sup> The amplitude must further go to zero at  $r=0$ , while  $\psi_{\text{tot}}$  and  $\psi'_{\text{tot}}$  must be continuous at  $R$ , which determines the behavior of the wavefunction for all  $r$ . Either by increasing  $k$  or making  $V_0$  deeper, it is possible to reach a situation in which  $\delta_0 = \pi$ , resulting in complete destructive interference of the incident and scattered wavefunctions for all  $r > R$  and consequentially zero scattering cross-section (figure 2.2). For  ${}^7\text{Li}$ , the  $k$  at which this *Ramsauer-Townsend effect* takes place corresponds to a temperature of approximately 10 millikelvin, which is just an order of magnitude higher than the lowest temperature achievable

---

<sup>1</sup>For  $V_0 > R$ ,  $\psi_{\text{in}} \propto \sinh k'r$  and  $k'$  is rather determined by  $V_0 - E = \hbar^2 k'^2 / (2m)$

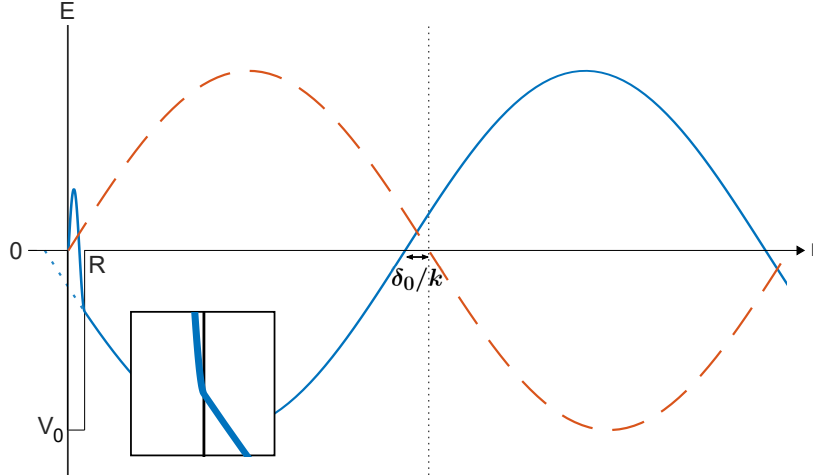


Figure 2.2: Cartoon of scattering off a rectangular well. The scattered wavefunction (solid blue line) is phase-shifted by  $\delta_0$  with respect to the unscattered wavefunction (dashed red line). The inset shows the point at which the wavefunction crosses the potential.

in the MOT,<sup>2</sup> necessitating some form of sub-Doppler cooling.

### High three-body loss coefficient

The three-body coefficient of  ${}^7\text{Li}$  is  $1 \times 10^{-27} \text{ cm}^6/\text{s}$  [42], compared to  $4.3 \times 10^{-29} \text{ cm}^6/\text{s}$  for  ${}^{87}\text{Rb}$  [43], or  $1.1 \times 10^{-30} \text{ cm}^6/\text{s}$  for  ${}^{23}\text{Na}$  [44]. At densities of  $10^{13} \text{ cm}^{-3}$ , typical for magnetic trap evaporation in other atoms, the characteristic loss time is approximately one second— a time much shorter than the length of evaporative cooling in most cold atoms experiments. As the inelastic collision rate scales with  $n^2$  but the elastic collision rate only with  $n$ , one might be tempted to reduce the density of the cloud in order to avoid losses, but sacrifices overall speed of evaporation.

### Path to degeneracy

After laser cooling, the cloud should be compressed in a tight magnetic trap in order to increase the two-body collision rate, yet doing so without sub-Doppler cooling would be futile because the temperature of the compressed cloud would approach the zero-crossing of the scattering cross-section. A simple polarization-gradient cooling step will not work due to  ${}^7\text{Li}$ 's level structure, so it is replaced by scheme on the D1 line involving a motional dark state, which is known in the

<sup>2</sup>Although the Doppler limit  $\hbar\Gamma/(2k_B) \approx 140 \mu\text{K}$  in  ${}^7\text{Li}$ , the high optical density of the laser-cooled cloud requires large detunings and engenders rescattering, both of which contribute to raising the temperature of the MOT to about 1.2 mK.

literature as a Gray Molasses. These two steps require significant laser power on both the D2 and the D1 lines. Once in the magnetic trap, the density is constrained on one side by three-body loss, and on the other by background gas collisions. The framing of this problem is not unique to  ${}^7\text{Li}$ ; rather, it is the stringency of the conditions that causes unusual difficulty, as the range of acceptable densities and initial temperatures is narrow. Once the phase space density is increased to near-degeneracy, the atomic cloud must be transferred to an optical dipole trap so that a large magnetic bias field may be introduced and the scattering length tuned to a positive value by proximity to a Feshbach Resonance.

## 2.2 Overview of the Apparatus

Before detailing how the unique cooling challenges presented by  ${}^7\text{Li}$  are solved in this experiment, a brief description of the apparatus is in order, with particular emphasis on design decisions that enable unique features of the experiment. A description of the IR laser system and its associated control hardware, which is used for both the optical dipole trap and lattice potentials, will be saved for Chapter 3.

### 2.2.1 Cooling and Imaging Laser System

Lithium laser systems are often power-starved; not only does the atom require high optical power for cooling schemes, but 671 nm lasers are both comparatively weak and expensive. These considerations strongly influence the design of the laser system. Laser light is provided by three external cavity diode lasers (ECDLs) and five tapered amplifiers (TAs). The ECDLs are Toptica models, while the TAs are a combination of Toptica models and home-built designs.

#### Atomic line locks

A Saturated Absorption Spectroscopy (SAS) locking scheme is employed to control the frequencies of the ECDLs which provide D1 and D2 seed light (the two locks are operated in parallel). Approximately counter-propagating pump and probe beams are passed through a nitrogen-buffered cell containing a gas of Lithium atoms heated to 400°C. The pump beam saturates the transition of atoms with a certain longitudinal velocity, resulting in peak transmission of the probe beam

when the laser frequency is swept over the atomic transition. The frequency of the probe light is modulated at 30 MHz using an Electro-optic Modulator (EOM), and demodulated by mixing with a reference signal, as in lock-in amplification. The resulting dispersive feature centered at the peak transmission frequency is an error signal which can be used to lock the imaging laser with a computer-controlled frequency offset with respect to the D2 laser (see figure 2.3).

### **Offset lock**

The imaging laser (Toptica DL100) is locked to the D2 transition using a delay-line offset lock technique described in [45]. The beatnote between the D2 laser and the imaging laser is observed on a fast photodiode and mixed with a local oscillator whose frequency is tunable between 300 MHz and 1.3 GHz. The resulting signal is low-passed and mixed with itself after a 6 ns delay. This produces fringes spaced by about 100 MHz as the frequency of the imaging laser is scanned over the frequency of the D2 laser. The linear region of one such fringe constitutes an error signal which can be used to lock the laser.

### **Optical table layout**

The MOT requires similar intensities of both cooling and repumping light (D2-F2 and D2-F1), while the use of Gray Molasses requires high intensity D1-F2 light. At the same time, while the D1 and D2 transitions in  ${}^7\text{Li}$  are relatively closely spaced compared to other alkalis, their 10 GHz detuning is still beyond the range of Acousto-optic Modulators (AOMs). These constraints can be elegantly satisfied by a modular system in which the same TAs can be seeded by either of two different ECDLs, locked separately to the D1 and D2 transitions. One TA provides F2 light, whose seed frequency is adjustable by means of a tandem AOM pair, while the other TA has its seed frequency shifted by a double-passed AOM so that it provides tunable F1 light. These seed AOMs are responsible for all the frequency tuning of the laser cooling system; the rest of the AOMs may operate at fixed frequency. Imaging light comes from a separate DL whose frequency is controlled by the previously described offset locking scheme. This design has the advantage that all frequency tuning happens before the amplification stage, so that minimum power is sacrificed in the least efficient AOMs in the system. Additionally, there is no dependence of fiber-coupling efficiency on laser frequency.

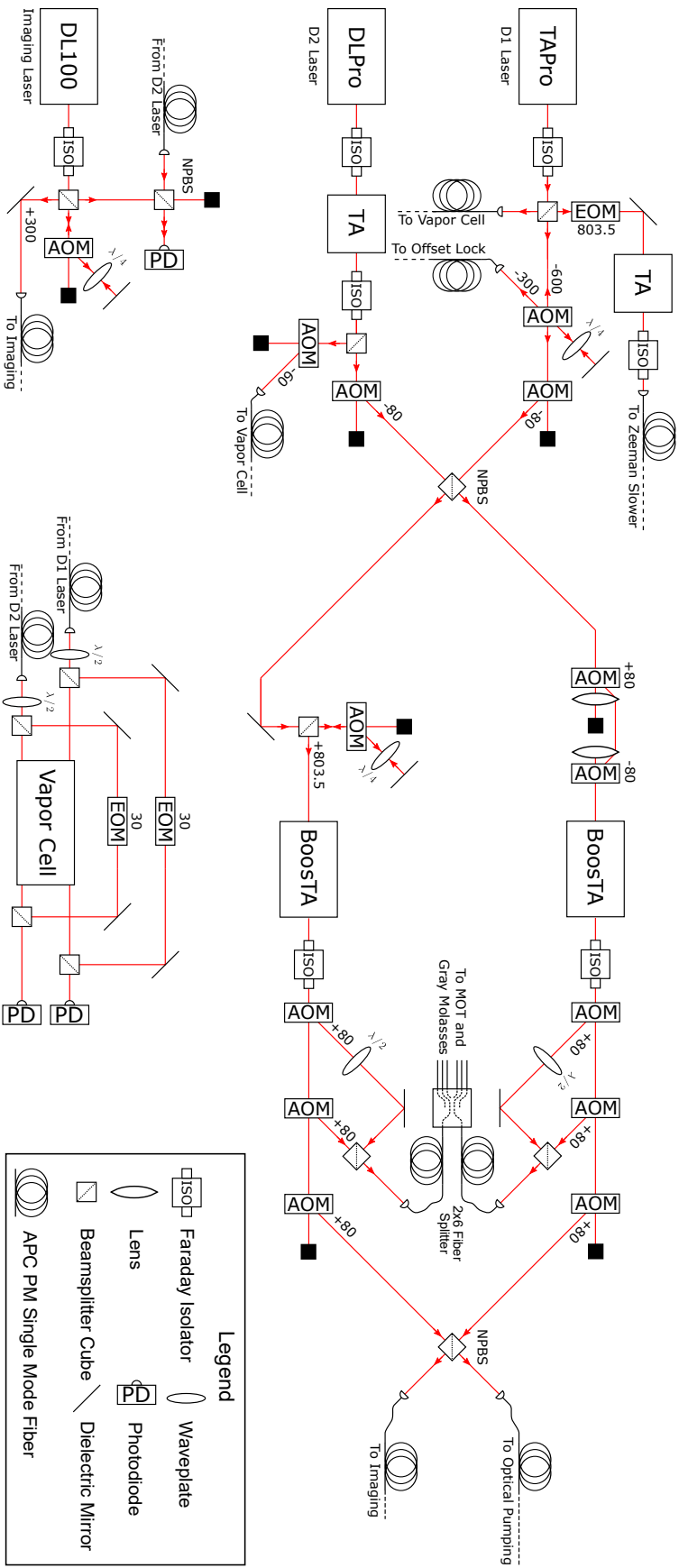


Figure 2.3: Schematic of the optical table layout, including cooling and imaging light generation, atomic line lock, and offset lock. Beamsplitter cubes are polarizing, except where marked as non-polarizing beam splitters (NPBS). The direction of propagation of the light is indicated with arrows. The Topoptica TAPro laser contains both a DLPro ECDL and a tapered amplifier in a single unit. Not pictured are beam-shaping telescopes, coupling lenses, folding mirrors, and polarization cleanup optics.

## Beam delivery

Because the requisite MOT repumping light intensity is almost equivalent to the cooling light intensity, the repumping light must also be configured as a MOT, with six beams and appropriate polarizations. The Gray Molasses light should have the same geometry and polarization as the MOT light, but whereas the MOT should use the largest possible beams in order to increase trapping volume, the GM should have smaller beams in order to maximize intensity and therefore cooling rate. To solve these dual problems, we use a polarization-maintaining 2x6 evanescent wave coupled fiber splitter (Evanescent Optics). Each input fiber receives light from either the F1 or F2 TA, and the six output fibers are arranged in counter-propagating pairs along the spatial axes of the vacuum chamber. At the outputs, polarization-dependent optics send the beams through two different telescopes depending on which axis of the fibers is used. These axes are in turn selected by turning on one of two different AOMs, which couple light through different ports of a polarizing beam splitter (PBS), as in figure 2.3.

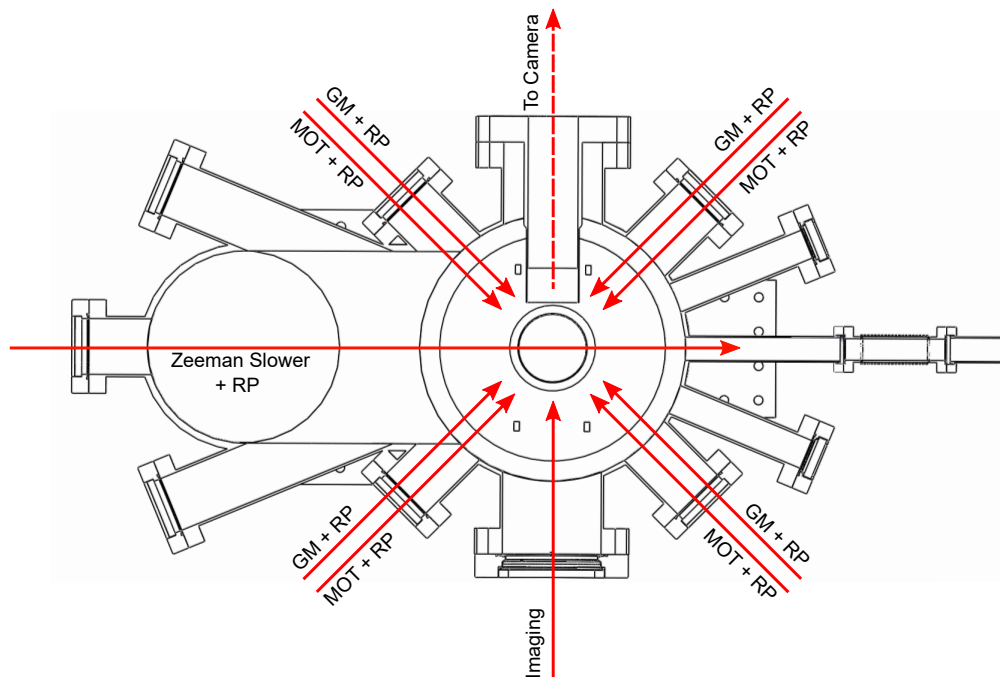


Figure 2.4: Horizontal cooling and imaging beams, and their repumpers (RPs), viewed from above against a horizontal cutaway of the chamber. Not pictured are the vertical MOT and Gray Molasses (GM) beams, or the vertical and auxiliary imaging beams.

### 2.2.2 Chamber Design

The effusive oven source is separated from the main chamber by two stages of differential pumping, with aspect ratios of 10 and 25 (the second stage includes the Zeeman slower tube itself). Vacuum pressures of about  $5 \times 10^2$  times higher than in the main chamber are permitted in the oven chamber, which is important for operating the experiment with fast loading times and low atom loss. The atomic beam is collimated by an orifice before it enters the first differential pumping tube. The Zeeman slower is a spin-flip slower design, which has the simultaneous advantages of detuning the slowing light far from zero-field atomic resonance and minimizing the stray field created by the slower coils at the position of the MOT. The length of the slower is constrained by the maximum deceleration experienced by a  ${}^7\text{Li}$  atom due to saturation-limited scattering,<sup>3</sup>  $a_{\text{max}} = h\Gamma/\lambda/(2m)$ , and the RMS velocity of the atoms leaving the oven  $\bar{v} = 2\sqrt{k_{\text{B}}T_{\text{oven}}/m}$ , so that  $L_{\text{min}} = \bar{v}^2/(2a_{\text{max}}) \approx 1$  m for the parameters of  ${}^7\text{Li}$  and assuming an oven temperature of 700 K [46].

Cycle time is minimized by employing a single-chamber design. Laser cooling light is periscoped into the chamber from below. After the atoms are laser-cooled and transferred to a magnetic trap, the top mirrors of the periscopes retract on stages with compressed air actuators to make room for lattice beams propagating along the same axes. This design replaces the standard technique of moving the atomic cloud from a chamber with laser cooling beams to a chamber with lattice beams, saving time and reducing complexity. Beams for optical dipole traps have independent access through windows offset at  $\pm 22.5^\circ$  on either side from the atomic beam axis. An imaging axis along the perpendicular direction supports 1" lenses with an  $f$ -number of 1 using a re-entrant viewport on one side.

In addition, the top and bottom chamber windows are recessed in so-called “buckets” so that magnetic coils may be placed close to the atoms, ensuring that sufficiently high gradients and fields can be generated without in-vacuum coils. A “chimney” for titanium sublimation pumping is appended to the main chamber; this chimney has the dual requirement that it should have an interior surface area similar to that of the main chamber, and that the titanium sublimation filament should not have line-of-sight to any windows. There are also assorted access ports for

---

<sup>3</sup>Assuming an optimized magnetic field profile that matches the Doppler shift of the slowed velocity group everywhere in the slower.

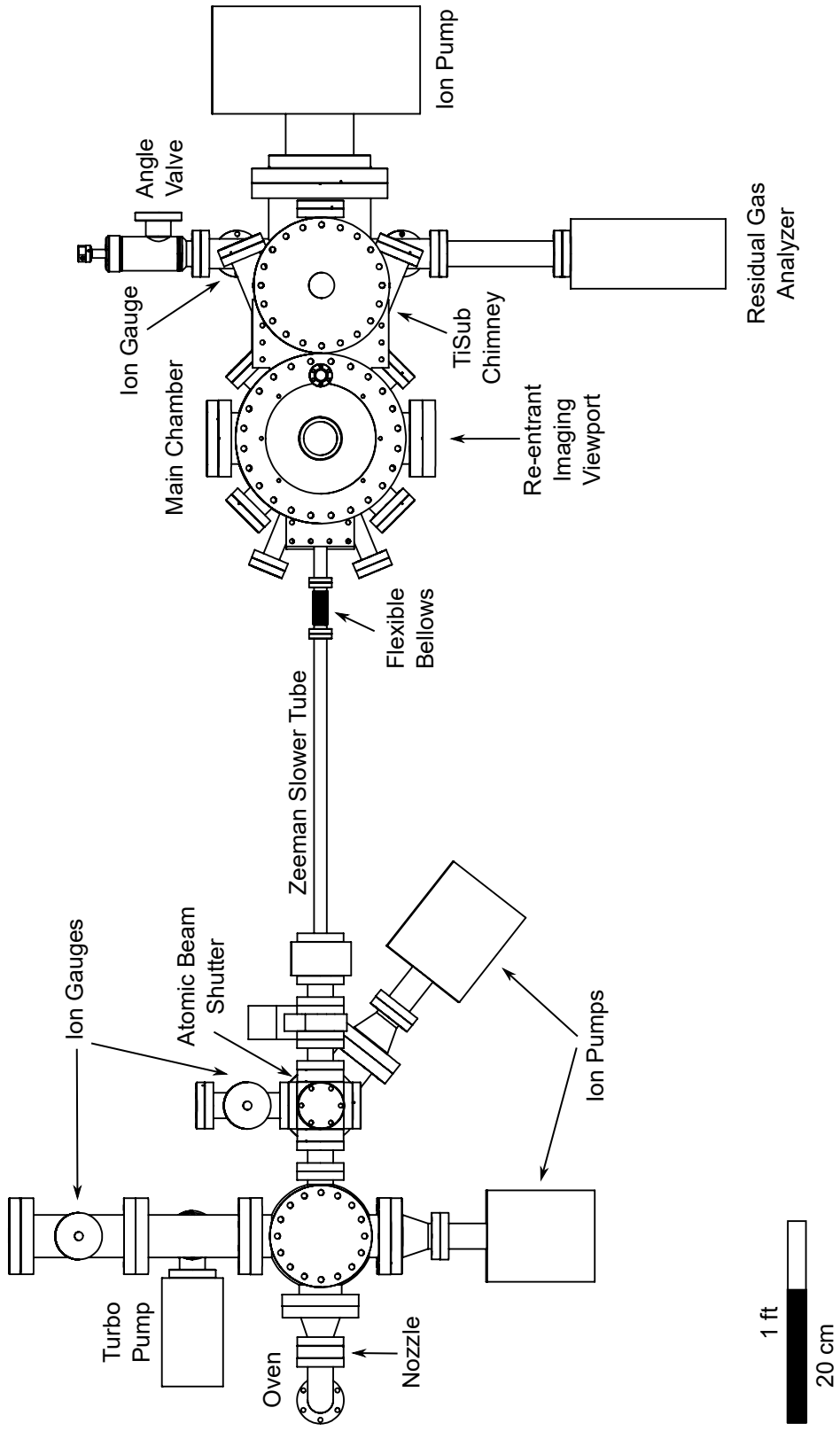


Figure 2.5: A diagram of the vacuum apparatus, viewed from the top. Not pictured are magnetic coils, support structures, or beam optics.

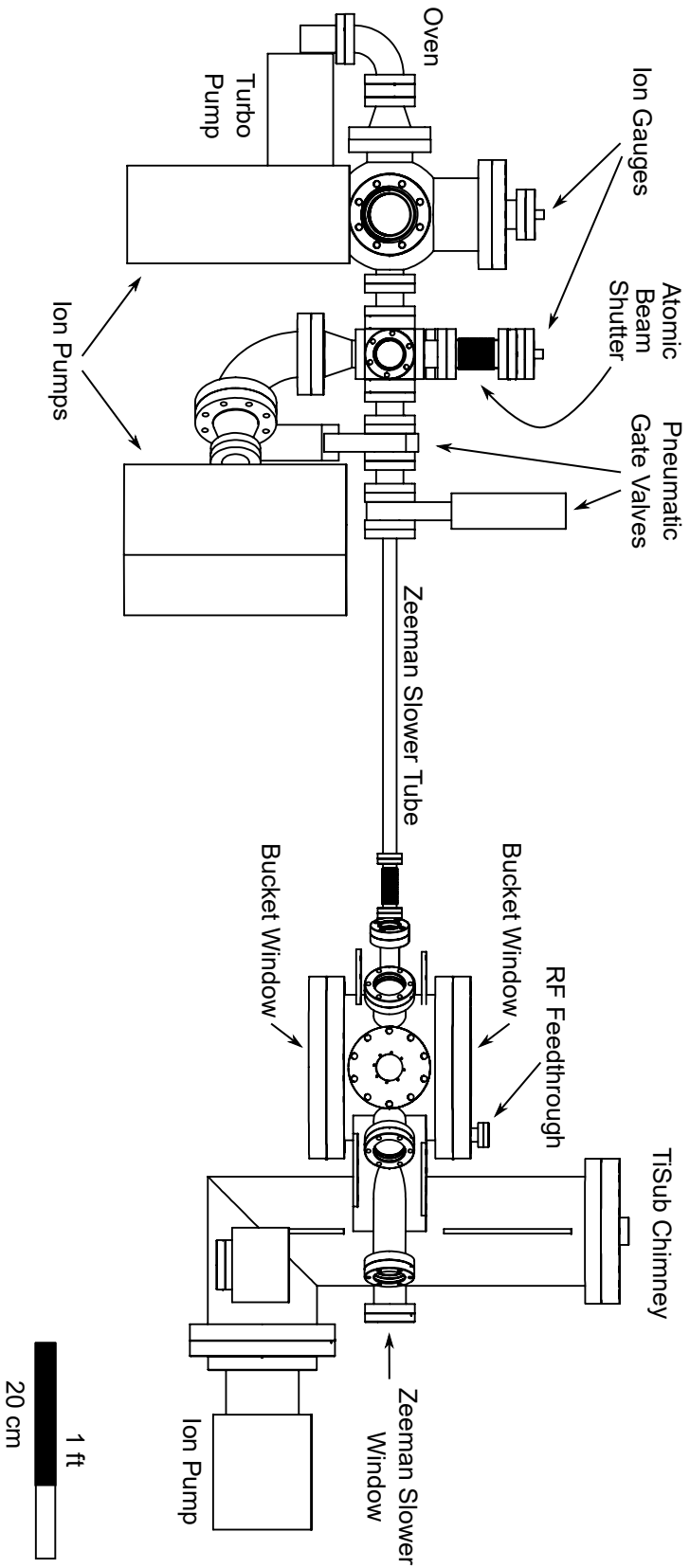


Figure 2.6: A diagram of the vacuum apparatus, viewed from the side. Not pictured are magnetic coils, support structures, or beam optics.

various vacuum pumps and gauges. Ion pressure gauges and ion pumps are operated continuously.

Aside from the coils in the recessed windows (“main coils”), which carry currents up to 500 Amps and are water-cooled, there are also low-current Helmholtz coils wound about the chamber along each axis. These “shim coils” can provide bias fields of up to 20 Gauss when powered by a few Amps of current, and each has several layers which can be controlled independently. They are used to cancel the Earth’s magnetic field (about half a Gauss) and to provide biases for various pumping and imaging steps.

There is also an in-vacuum RF antenna, which is arranged so that it creates AC magnetic fields which are perpendicular to the strong bias field created by the main coils; this orientation is chosen so that it can be used to drive  $\sigma^\pm$  transitions between hyperfine states at high field. It is also used for RF evaporation in the magnetic trap (see section 2.4.1). The antenna is a single loop of uninsulated, 3 mm diameter oxygen-free copper, held in place by MACOR standoffs and powered via a feedthrough on the top bucket window. At low field ( $|B| < 20$  G), this antenna achieves Rabi frequencies of up to  $2\pi \times 20$  kHz on hyperfine transitions when powered by a 10 W RF amplifier.

### 2.2.3 Coil Design

The experiment requires both quadrupole fields for magnetic trapping and bias fields for manipulation of the atomic interactions via Feshbach resonances. Because the Feshbach resonances of  ${}^7\text{Li}$  are located at high fields, the coils must be capable of generating up to 1000 G using reasonable currents ( $< 500$  A). Proximity to the atoms is important both for creating bias fields with the least curvature (fulfilling the Helmholtz condition) and for generating the largest quadrupole fields, so the same coils will be used in two different electrical configurations in order to supply both types of fields: the polarity of some of the top layers can be swapped using four IGBTs configured as an H-bridge (figure 2.7b). Because the Larmor precession is much faster than  $\frac{dB_i}{dt}/B$  for atoms in motion through a trap or bias field with components  $i = x, y, z$ , the axis about which the atoms precess follows the direction of the magnetic field everywhere. Thus the atoms respond to the magnitude of the magnetic field  $|B|$ , which is plotted in figure 2.8 for ideal coils in quadrupole and bias configuration.

Curvature (second derivatives of  $|B|$ ) influences the potential energy landscape experienced by the atoms by creating trapping (or anti-trapping) forces with characteristic trap frequency

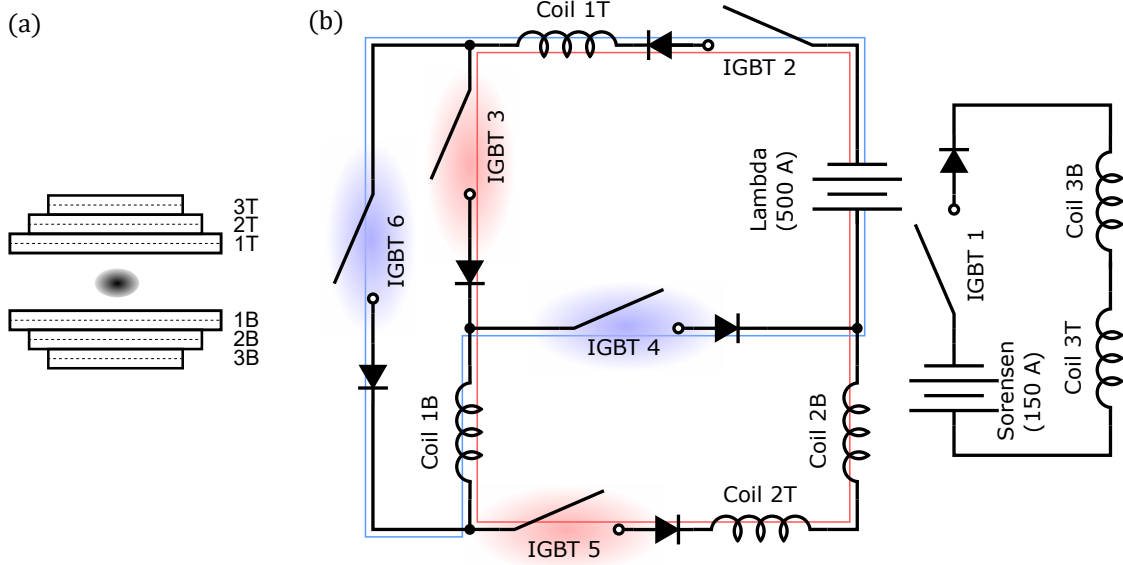


Figure 2.7: (a) The top and bottom coils are each made from three segmented double-layers, pictured here in cross-section from the side. (b) A schematic of the high current circuit for generating magnetic fields. Insulated-Gate Bipolar Transistors (IGBTs) in an H-bridge configuration can switch the circuit between bias field and quadrupole field configurations. When IGBTs 4 and 6 are closed (IGBTs 3 and 5 are open), layer 1 generates a bias field (current follows the blue path). When IGBTs 3 and 5 are closed (IGBTs 4 and 6 are open), layers 1 and 2 generate a quadrupole field as the polarity of the bottom layers has been inverted (current follows the red path). Layer 3 is configured permanently in quadrupole configuration, to provide a quadrupole field for magneto-optic trapping and auxiliary gradients.

$\omega_x = \sqrt{2\mu_B B''/m}$ . Because of its light mass,  ${}^7\text{Li}$  is therefore particularly sensitive to these trapping potentials, which can limit the minimum achievable density of the BEC or the minimum flatness of an applied optical potential. To ensure that the bias fields can be generated with minimum curvature, the coils should be segmented in such a way that the primary layer fulfills the Helmholtz condition as nearly as possible, while the other layers can be used for tuning the curvature (figure 2.7a). The coils should also be able to maintain this field for the duration of the experiment without overheating, and should quickly approach an equilibrium temperature if the experiment is run continuously with some duty cycle.

### A warning about symmetry

Special care should be taken that the center of curvature of the bias field overlaps with the zero of the quadrupole field, so that it is not necessary to transport atoms between the two locations. To meet this condition, the coils need to be wound with inversion symmetry— put another way,

for every bit of  $d\mathbf{I}$  in the top coil, there must be an equivalent  $d\mathbf{I}$  on the bottom coil to which one can draw a line which passes through the origin. If both coils are wound in the same fashion and one is simply rotated about the  $x$  or  $y$  axis and then the  $z$  axis in order to form a coil pair, the resulting setup will not be inversion-symmetric. The distance between the centers of the bias and trapping fields can be quite significant—many millimeters—so that atoms which are to be transferred between a magnetic trap and an optical dipole trap located at the saddle point of a large bias field must be transported over a large distance, which adds time to the cooling sequence and introduces opportunities for heating and atom loss.

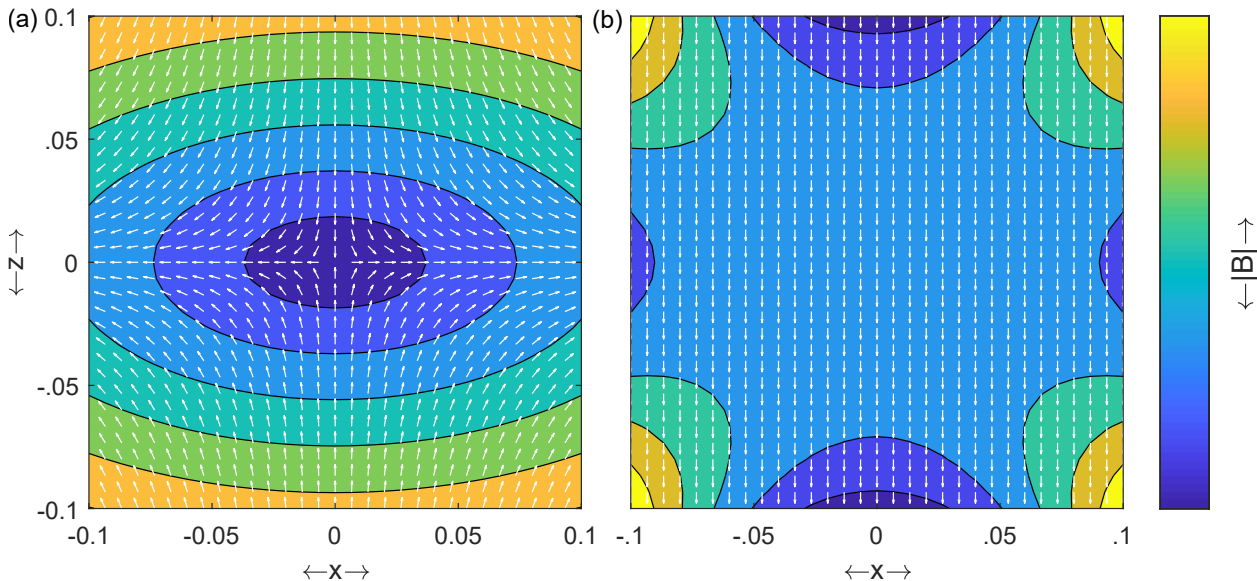


Figure 2.8: A cut through the XZ plane of the fields produced by an ideal coil pair in anti-Helmholtz (a) and Helmholtz (b) configurations. The contours are equipotential lines of  $|B|$  and the arrows are the unit vectors  $\mathbf{B}/|B|$  which indicate the field direction at each point. The scale of the axes is the coil radius.

### Helmholtz condition

The magnetic field due to a static current, according to the Biot-Savart law, is

$$\mathbf{B} = \frac{\mu_0}{4\pi} \int_C \frac{I d\mathbf{l} \times \mathbf{r}'}{|\mathbf{r}'|^3} \quad (2.6)$$

for a current  $I$  following a path  $C$  made of segments  $d\mathbf{l}$  [47]. At a point  $\mathbf{r}$  the field  $\mathbf{B}(\mathbf{r})$  is perpendicular to both the direction of the current  $\mathbf{l}$ , and to the vector connecting the point to the

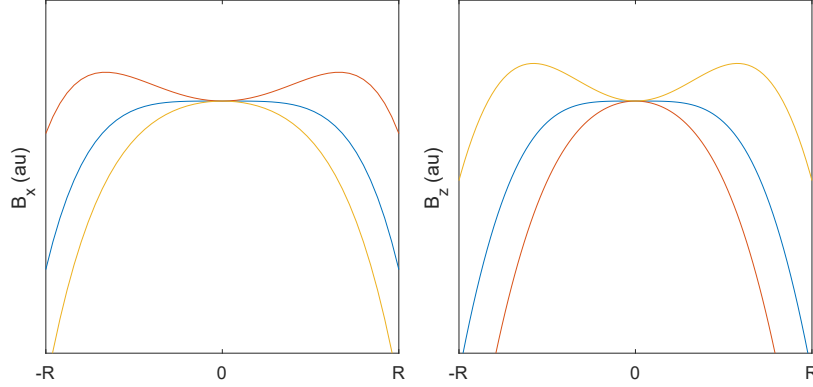


Figure 2.9: A pair of coils fulfills the Helmholtz condition when the separation distance equals the coil radius  $R$  (blue line). The axial field  $B_z$  acquires positive curvature when the separation distance is greater than  $R$  (yellow line) and negative curvature when the separation distance is smaller than  $R$  (red line). The opposite is true for the transverse fields  $B_x$  and  $B_y$ .

current element,  $\mathbf{r}' = \mathbf{r} - \mathbf{l}$ . A circular conductor of radius  $R$  is rotationally symmetric and will therefore create a field that points along the axis of symmetry, everywhere along this axis:

$$\mathbf{B} = \frac{\mu_0 I}{2} \frac{R^2}{R^2 + z^2} \hat{z} \quad (2.7)$$

This field exhibits a magnetic field gradient  $B'_z = \frac{\partial B}{\partial z}$ . In order to generate a quadrupole field, one may add a second such coil with *opposite* polarity at some distance  $a$  along the  $z$ -axis so that all even derivatives of the field cancel everywhere and  $\mathbf{B} = 0$  at the origin (see figure 2.8). If instead another coil is added with the *same* polarity, it is rather the even derivatives of the field which cancel and  $B'_z = 0$  everywhere in the midplane (by reflection symmetry). One may further vary the ratio  $a/R$  in order to vary the curvature of the field  $B''_z$  at the midpoint. A quick calculation shows that  $a/R = 1$  achieves  $B''_z = 0$ , which is known as the Helmholtz condition. In general it is possible to add more coils in order to cancel even higher order derivatives of the field. The residual curvature leads to a trapping (or anti-trapping) potential with the oscillator frequency  $\omega = \sqrt{2B''/m}$ .

### Ideal coils

In general, it is not possible to fulfill the Helmholtz condition with realistic coils. As a first approximation, one may consider infinitely thin, circular coils whose separation deviates from the

Helmholtz condition. In free space, magnetic fields obey the Laplace equation

$$\nabla^2 B_z = 0 . \tag{2.8}$$

Due to cylindrical symmetry,  $B_z$  is the only non-zero component of the field on-axis. Cylindrical symmetry therefore requires that  $\frac{\partial^2 B_z}{\partial x^2} = \frac{\partial^2 B_z}{\partial y^2} = -\frac{1}{2} \frac{\partial^2 B_z}{\partial z^2}$ , so that the form of the magnetic field at the origin is a saddle point. If  $\partial^2 B_z / \partial z^2$  is zeroed, the other two second derivatives of  $B_z$  must be identically zero, again because of cylindrical symmetry. Using two sets of coils whose separations deviate from the Helmholtz condition, it is possible to solve for a ratio of currents  $I_1/I_2$  that gives zero curvature at the origin. It is desirable to have one coil pair spaced by less than the Helmholtz condition and the second spaced by more— that way,  $B_z$  will have the same sign for both coil pairs at the zero curvature condition, requiring less overall current.

### Practical coils

Practical coils offer several obstacles to achieving a curvature-free magnetic field. A pair of coils made from wire of finite thickness cannot meet the Helmholtz condition for every current path contained in the bulk of the wires. Additionally, it is not possible to wind a perfectly symmetric current loop, for at least one must account for leads to bring the current into and out of the loop. Further, if the coils are to be wound from a wire conductor, it may be advantageous to wind the loops as a continuous spiral rather than as a series of concentric circles. These considerations break the cylindrical symmetry of the problem and so it is no longer true that  $\partial^2 B_z / \partial x^2$  and  $\partial^2 B_z / \partial y^2$  are zero when  $\partial^2 B_z / \partial z^2$  is zero; nonetheless, (2.8) still requires they have equal magnitude and opposite sign. It is also no longer true that  $B_x = B_y = 0$  on-axis, although in the high field limit  $|B| \approx B_z$ . The resulting field will have elliptical equipotential lines, where the ellipticity comes from the breaking of circular symmetry and the deviation of the angle of the axis of the ellipse comes from the breaking of inversion symmetry. These problems can be somewhat mitigated by creating a counter-wound bilayer coil (where each “coil” has two layers, one with each handedness), which also has the advantage that the distance between the leads is minimized, along with their contribution to the total field.

## Canceling curvature

Defining the midpoint between the coils to be the origin, one finds

$$|B| = \sqrt{\sum_i (B_i^0)^2} \quad (2.9a)$$

$$\frac{\partial|B|}{\partial x_l} = \frac{1}{|B|} \sum_i B_i^0 B_i^l \quad (2.9b)$$

$$\frac{\partial^2|B|}{\partial x_l \partial x_m} = \frac{1}{|B|} \left( -\frac{\partial|B|}{\partial x_l} \cdot \frac{\partial|B|}{\partial x_m} + \sum_i (B_i^l B_i^m + B_i^0 B_i^{ml}) \right) \quad (2.9c)$$

where  $i, l$  and  $m$  each range over the three dimensions and superscripts indicate a derivative. The components  $B_i$ ,  $B_i^m$  and  $B_i^{ml}$  can be easily calculated from (2.6):

$$dB_i = \frac{dl_j r_k \epsilon_{ijk}}{|r|^3} \quad (2.10a)$$

$$\frac{\partial dB_i}{\partial x_l} = -3 \frac{B_i r_l}{|r|^2} + \frac{dl_j \epsilon_{ijl}}{|r|^3} \quad (2.10b)$$

$$\frac{\partial^2 dB_i}{\partial x_l \partial x_m} = -3 \frac{B_i}{|r|^2} \delta_{lm} - 3 \frac{dl_j (r_m \epsilon_{ijl} + r_l \epsilon_{ijm})}{|r|^5} + 15 \frac{B_i r_l r_m}{|r|^4} \quad (2.10c)$$

where the initial constants  $\frac{\mu_0 I}{4\pi} = 1$  and repeated indices imply summation.

The asymmetry of practical coils means that even if the  $z$ -curvature is zeroed using a multi-coil scheme, there will be residual horizontal curvature, which can lead to trapping frequencies as large as several Hertz for  ${}^7\text{Li}$  atoms. In general, it can be said that every pair of coils spaced by a distance  $d$  can be characterized by a certain ratio of  $\partial_{xx}/\partial_{zz}$  (or equivalently  $\partial_{xx}/\partial_{yy}$ ). It is then clear that zeroing arbitrary curvature requires at minimum three layers, and the minimization procedure is as follows:

1. Measure (or calculate) the ratio  $\partial_{xx}/\partial_{zz}$  for the primary coil pair.
2. Place two more pairs of coils with varying separation on the same axis. Vary the ratio of the current in these two coils until their combined field has the same  $\partial_{xx}/\partial_{zz}$  as the primary coil.
3. Vary the ratio of the currents between the primary coil and the compensation ‘‘super-coil’’ until the  $z$  curvature is canceled.
4. Vary the overall prefactor of the currents in order to achieve the desired magnetic field.

Any remaining curvature should be due entirely to second derivatives of the transverse fields. This problem can be mitigated by minimizing the transverse fields themselves, for  $B_i''$  always appears with the coefficient  $B_i$  in the expressions for the derivatives of  $|B|$ . The residual transverse fields are due to the presence of leads and to the helicity of the coil (approximately in equal parts). It is possible to understand the contribution from the helicity by recognizing that the current flowing in a helical coil has a radially symmetric component *and* a transverse component (the transverse component is proportional to the pitch of the spiral, which is the wire diameter). Both the contributions of the helicity and of the leads can be simultaneously addressed by winding *bilayer* coils, which wind inwards on one layer and then outwards on the other (figure 2.10). The two layers mostly cancel the effect of their helicities, while also minimizing the distance between the input and output leads. Further, specifically at the origin, it would be possible to servo out the small remaining curvature with bias fields, for ultimate control.

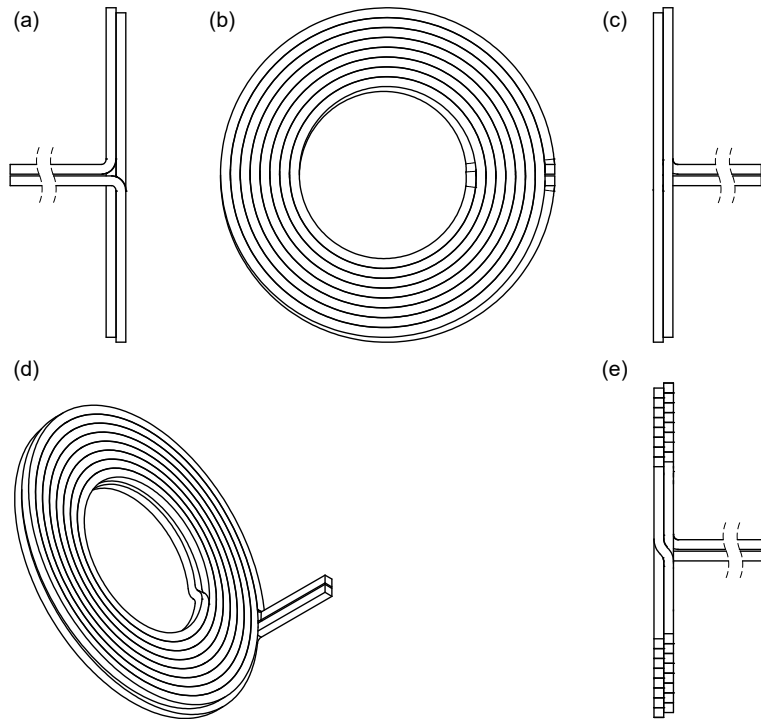


Figure 2.10: Schematic of one of the spiral bilayer coils designed for this experiment, with eight windings, an inner radius of 37 mm and pitch of 5 mm (matching the diameter of the square wire). This coil and its inverse form the pair closest to the atoms, designated layer 1T and 1B in figure 2.7. (a) through (d) show the coil from various angles, while (e) shows view (c) in cross-section.

The fact that  $\partial^2 B_z / \partial x^2 = -\partial^2 B_z / \partial y^2$  when the  $z$ -curvature is zeroed suggests a clever arrangement of coils which uses current most efficiently: if the compensation coils are all similarly wound, rotating one pair of them by 90 degrees will make the horizontal curvatures approximately cancel and allow total curvature cancellation with far less current than would otherwise be required. A further caveat is that the symmetry axes of the field of a coil (the major and minor axes of the generally ellipsoidal equipotential lines) are not aligned with the axes of the coil itself, as defined by the leads. In order to fully exploit the curvature canceling strategy discussed above, the symmetry axes of the fields must be aligned with one another; in this respect, a full numerical simulation of the coil configuration, including thick wires and leads, proves extremely useful.

From equation 2.10c, it is readily apparent that magnetic field gradients are turned into curvature of  $|B|$  in the presence of a bias field. Indeed, if one is bothering to minimize curvature at all, it is quite likely that a gradient will also be necessary to cancel the effect of gravity. In  ${}^7\text{Li}$  at high field, this gradient is about 1.23 G/cm, leading to residual transverse curvature of  $5 \times 10^{-4}$  G/cm<sup>2</sup> at 800 G, which corresponds almost exactly to a trap frequency of 100 mHz. If the trap is made isotropic by adjusting the curvature compensation, the curvature can be lowered by a factor of 2/3 and the trap frequency by  $\sqrt{2/3}$ . The theoretical limit of curvature cancellation with gravity compensation in  ${}^7\text{Li}$  is therefore about 80 mHz.

### The coil-winding process

This section provides a detailed description of the production process for a pair of coils. The wire chosen for the coils in this experiment is 5 mm  $\times$  5 mm square copper with a 2 mm diameter round hollow core and fiberglass insulation, manufactured by MWS, Inc.. The wire is rather stiff, and in order to maintain enough tension to wind it tightly, it should be wound around a jig which can be rotated by a lathe. The advantages of larger wire cross-section are mainly current handling and cooling capacity. The greater the tension the lathe can apply, the fewer imperfections there will be in the coil. In order to wind coils using a lathe, one needs:

- A low-speed, high-torque gear option for the lathe (10 rpm is a reasonable speed).
- A rig for holding and applying tension to the wire spool, and possibly a wire guide or straightener to remove kinks before winding.

- A form around which to wind the coil. This form should be spiral-shaped, with a pitch equal to the wire diameter, and should be made of aluminum in order to withstand the significant forces experienced during winding (figure 2.11a).
- A dowel to attach the form to the lathe chuck. This dowel should have one round or hexagonal end, in order to fit into the chuck, and one end that can transfer torque to the winding form, e.g. D-shaped, and should also be made of aluminum.
- A pair of plates to keep the wire in the plane of the form during winding and to secure the wire during drying. These plates should be made of clear, scratch-resistant acrylic; clear acrylic enables observation the winding process, and the scratch-resistant surface is smooth enough that epoxy does not adhere to it very strongly (figure 2.11b).
- Epoxy to bind the layers of the coils. NM-252 (Duralco) is a non-magnetic, high temperature two-part epoxy that works well for this purpose.

The plate design used for these coils is pictured in figure 2.11a; two of the same plates can be used to make the form for a bilayer coil. For the other coil in the pair, the spirals must have the opposite handedness and so require inverted plates. In order to wind bilayer coils with tight tolerances, the following procedure was developed:

1. Unspool enough wire to form one of the layers, including the lead, and make a 90° bend at the part closest to the spool. It helps to have a form around which to bend the wire.
2. Place one of the guide plates and one of the coil forms on the dowel; place the 90° bend of the wire on the starting point of the form, and clamp in place with the second guide plate. The excess wire that will eventually form the second layer should be pointing along the axis of the lathe, where it can rotate harmlessly in place.
3. Wind the coil, making sure to fully coat the inside surface of the wire with epoxy before each layer is wound. After completing the coil, continue winding until enough excess wire has been wound in order to form a lead. While continuing to maintain tension on the spool, clamp the guide plates tightly in place with C-clamps and wait until the epoxy has dried (figure 2.11c).
4. Remove the outer guide plate, add the second coil form to the dowel, bend the wire so that it is perpendicular to the lathe axis and replace the outer guide plate. Cut the first layer free from the spool.
5. Wind the second layer as the first, except that wire should be fed from the other side and the winding direction of the lathe should be reversed (figure 2.11d).

Once the epoxy on the coils has dried completely, the guide plates and coil forms can be completely removed and the leads bent into position (figures 2.11e and f). Three separate coils are bonded with epoxy in order to create a multi-layer coil package. The coils are further secured with epoxy to a ceramic washer that has threaded holes for brass rods. These rods attach to an

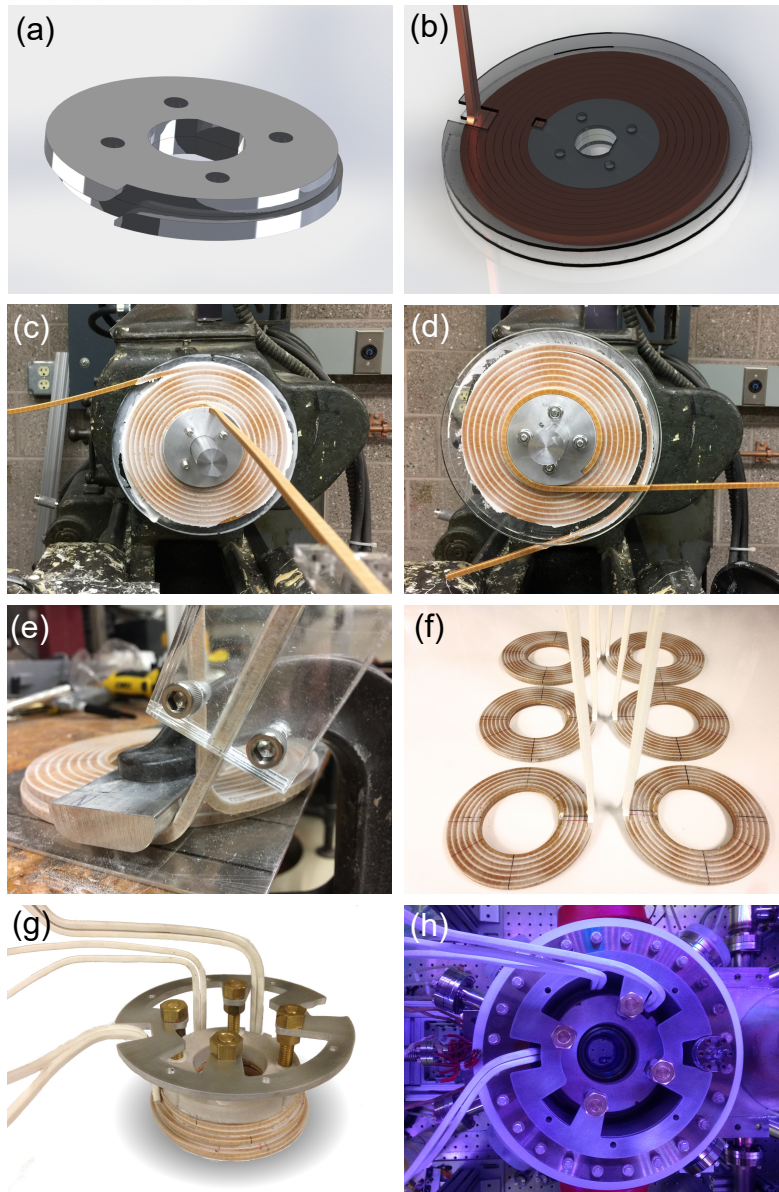


Figure 2.11: (a) Render of the winding form for bilayer coils. The form is an Archimedean spiral with a pitch equal to the wire diameter. A second form with opposite helicity must be made for the opposing coil. (b) Render of a completed bilayer coil with winding form and acrylic guide plates. (c) Photograph of a half-completed, left-handed bi-layer coil at the end of winding the first layer and (d) the beginning of winding the second layer of a right-handed coil. (e) The leads are bent around a form with the appropriate radius. (f) Three completed top coils and three completed bottom coils. (g) A view of the top three coils, assembled into a single package with ceramic washer and aluminum mounting bracket. (h) A view of the top coils mounted in the bucket window on the main chamber.

aluminum bracket which can be screwed to the top of the bucket windows in order to clamp the coil package against the inner surface of the bucket window (figures 2.11g and h).

### Design and characterization of the main coils

In order to be able to generate very high fields with low curvature, the top and bottom coils are made of three bilayer segments each (as in figure 2.10). The segments closest to the atoms have eight windings, with the more distant bilayers containing seven and six windings each. This design leaves space for the leads, and also varies the ratios of  $|B''|/|B|$  produced by each coil. Following the procedure outlined in the previous two sections, relative angles of  $+70^\circ$  and  $-15^\circ$  are chosen for the second and third bilayers relative to the first. A full thick-wire simulation further reveals that the trap frequency is limited by quartic terms to about 500 mHz, which is significantly higher than the theoretical limit of 80 mHz derived in the context of gravity compensation. While such perfect curvature cancellation is not necessary for any of the lattice simulations discussed in this thesis, it may prove useful for future projects and it would be interesting to characterize the curvature of the coils *in situ*.

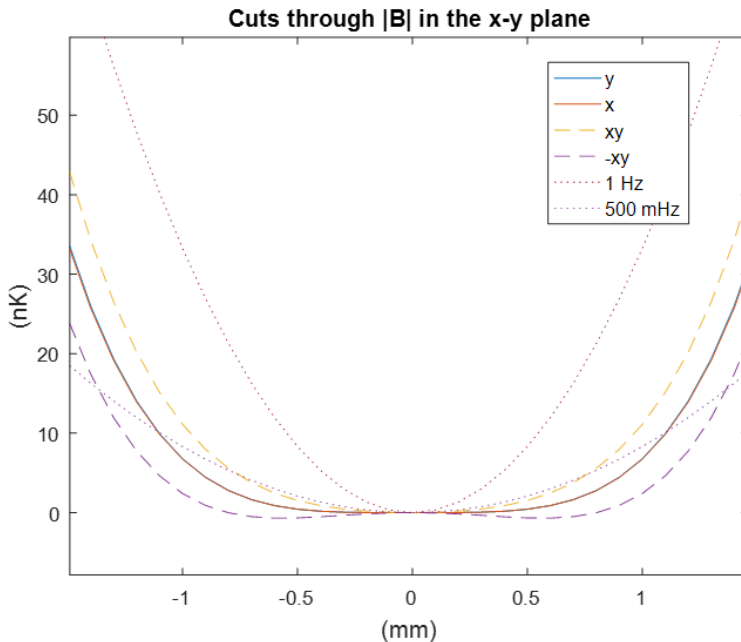


Figure 2.12: Simulated cuts through  $|B|$  in the XY plane at 750 G, with the curvature in the X and Y directions completely zeroed by varying the relative currents in the layers (only quartic terms remain). The field is plotted in temperature units ( $\mu_B|B|/k_B$ ), with 0.5 Hz and 1Hz trapping potentials plotted for comparison.

When the transverse overlap of the quadrupole zero and the bias field saddle point are measured *in situ* by finding the equilibrium position of the atoms in each field configuration, they are found to be offset by only 150 microns, thanks to the bilayer design and careful construction. On the other hand, the overlap along the  $z$ -axis is not nearly so good. In the plane of the quadrupole zero, the atoms experience a force upwards in a 750 G bias field which is about twice the force of gravity. It is suspected that the origin of this gradient, which vertically offsets the field centers, is a difference in the ferromagnetic content of the two bucket windows in which the coils reside, rather than due to a problem with the coils themselves. The top and bottom layers are connected in series, so the currents are identical, and further there exist no winding errors or shorts which could possibly give rise to a vertical gradient while simultaneously preserving the cylindrical symmetry necessary to create good transverse overlap. Regardless, it is possible to simply servo out this gradient by applying a small quadrupole field with layer 3– which was necessary anyway to cancel gravity. When all three layers are water-cooled in parallel at a pressure of 200 psi, they equilibrate at 5°C above the temperature of the cooling water in 10 s when supporting a series current of 500 A. In Helmholtz configuration, the temperature coefficient of the field is measured to be +2mG/°C via field-sensitive Zeeman transitions within the range 14°C to 27°C.

## 2.2.4 Computer Control and Data Collection

The control signals for the experiment consist of computer-generated analog voltages and TTL signals, synced by a variable-timebase clock with a minimum resolution of 2  $\mu$ s. The DACs are National Instruments PXI-6733s, while the TTL outputs are NI PXIe-6535s. Details about the clock, experimental sequence software environment (Cicero) and output card software controller (Atticus) can be found in the PhD thesis of Aviv Keshet, who designed and coded the first versions.

<sup>4</sup> The TTL channels are all optocoupled for safety and peace of mind with respect to grounding; the analog channels are isolated using Analog Devices AD215 analog isolators when connecting to high voltage equipment such as power supplies, or when the analog inputs of equipment are not differential already. The same computer control system synchronizes data collection from various cameras and ADCs, which after the completion of each experimental run or “sequence” are written

---

<sup>4</sup>The software is open-source and available for download at <https://github.com/akeshet/Cicero-Word-Generator>

into a database (MariaDB) along with all the control parameters of the sequence and basic pre-analysis of the data. Results are live-plotted and can be used for closed-loop feedback via the database, which is available via standard SQL queries. A MATLAB library has been developed that provides an object-oriented environment for analysis of absorption images of cold atomic clouds, BECs, and lattice superfluids in various trapping geometries and in time of flight (TOF).

Data is recorded by ADCs and CCD cameras. The experiment currently contains two fixed-position cameras and one auxiliary camera. On the axis with the re-entrant viewport (“imaging axis”) is an imaging system with variable magnification ( $\times 1/3$  through  $\times 20$ ) which images the atoms onto a low-noise EMCCD supplied by Princeton Instruments. The vertical axis is imaged by a PI CoolSnap CCD. The auxiliary camera is a PixelFly which can be moved about the chamber to assist with beam alignment procedures (there are imaging systems along each axis of the chamber, including mounting hardware for the PixelFly). The ADC channels are provided by an NI PXI-5105 card.

## 2.3 Laser Cooling

Many of the laser cooling techniques employed in this experiment are quite standard in the field and will not be reviewed here, except to provide some context for design choices, and to report operational details and characterizations of their performance. There is an incentive to improve phase space density as much as possible during laser cooling, because evaporation is a lossy cooling mechanism, and furthermore the lossiness (efficiency) of evaporation can be improved by starting with higher phase space density. Gains made at any stage of the laser cooling process therefore result in faster evaporation and larger degenerate clouds.

On the bright side, magneto-optic trapping often results in clouds cooled to below the Doppler limit (in fact, the very first MOT exhibited this surprising result, much to the consternation of the experimenters). The explanation for this effect is polarization gradient cooling which takes place near the zero-field center of a standard type-I ( $J \rightarrow J+1$ ) red-detuned MOT. Reaching the Doppler limit requires a detuning of  $\Gamma/2$ , which reduces capture velocity and decreases achievable densities due to enhanced light-rescattering. Additionally, the density can be increased by using a hollow repumping beam so that atoms in the center of the MOT are shelved in a dark state ( $F = 1$ ),

allowing the density to build up without rescattering [48].

Unfortunately, neither of these techniques provide much of an advantage in  ${}^7\text{Li}$ . It has been found that polarization gradient cooling of the red-detuned  $\sigma^+ - \sigma^-$  type, which usually enhances the cooling power of a MOT, does not function effectively in lighter alkalis on account of their degenerate hyperfine manifolds. The essence of the argument is that these schemes rely on a level of detuning-enhanced selectivity between the possible F2 transitions which is foiled by the tight spacing of the F' hyperfine levels in  ${}^7\text{Li}$ . Furthermore, the combination of indistinguishable hyperfine levels in the excited state and branching ratios that determine the hyperfine fate of atoms that undergo spontaneous emission means that atoms are approximately half as likely to end up in the F1 manifold as in the F2. This situation requires that there be nearly as much F1 light as F2.

### Atomic Beam Source

The oven is a stainless steel cup, connected to a nozzle by a  $90^\circ$  elbow and operated at  $485^\circ\text{C}$  by means of a regulated band heater (Omega Engineering). Whereas effusive flow from a pinhole nozzle would normally create a distribution with a solid-angle flux density proportional to  $\cos(\theta)$ , the nozzle used in this experiment is a special micro-channel plate which admits only particles with  $\text{atan}(v_\perp/v_\parallel) < \text{atan}(d_\perp/d_\parallel) \equiv \theta_0$  for length and width  $d_\parallel$  and  $d_\perp$  of the micro-channels (see figure 2.13). For a micro-channels with aspect ratios of 10,  $\theta_0 \approx 5^\circ$  and this pre-collimation of the beam is estimated to save 99% of the flux of atoms, as the atoms which are prevented from leaving the oven have velocities that would cause them to be lost before reaching the chamber (only atoms within a solid angle of  $\theta < 0.37^\circ$  reach the chamber, given the length and diameter of the Zeeman slower).

The effect of this nozzle can be observed by measuring the absorption of a laser beam propagating through the effusive flux as a function of laser frequency  $\omega_L$ . In order to see why, consider distribution of atoms after the nozzle. An atom passes through a nozzle of area  $A_0$  in a time  $dt$  if it can be found in the volume  $A_0 v_z dt$  before the nozzle. The probability that a randomly selected particle leaves the oven is

$$\frac{A_0 v_z dt}{V_0} \cdot p(\mathbf{v}) d^3v \quad (2.11)$$

for oven volume  $V_0$  and where  $p(\mathbf{v})$  is the 3D Maxwell-Boltzmann distribution. The total number

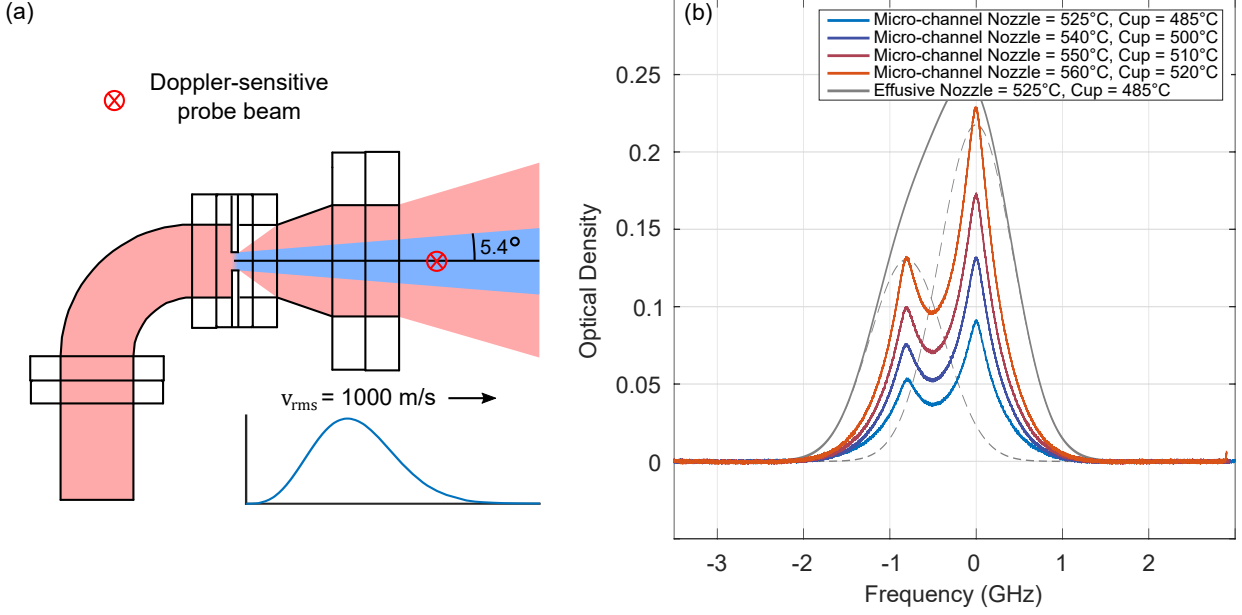


Figure 2.13: (a) A schematic representation of the oven filled with Lithium vapor. An effusive nozzle produces a density distribution with an angular dependence of  $\cos \theta$ . The micro-channel nozzle limits the maximum emitted angle to  $\theta_0 \approx 5^\circ$ . (b) A near-resonant laser passing perpendicularly through the atomic beam produces a Doppler-sensitive spectrum which reveals the distribution of transverse velocities in the atomic beam. The thermal atoms are randomly distributed between the two hyperfine ground states, leading to relative absorption strengths of  $3/8$  and  $5/8$  on the F1 and F2 lines, due to the multiplicity of the Zeeman sublevels. These two peaks can be seen distinctly in the spectra taken with the micro-channel nozzle, due to the significant decrease in Doppler-broadening. In the spectrum taken with the ordinary effusive nozzle, the two peaks must be distinguished by fitting (dashed gray line). The spectra have been shifted so that the F2 transition is at zero detuning.

$dN$  of such particles, recast in spherical coordinates  $d^3v = v^2 dv d\Omega$ , is

$$dN = n_0 A_0 v^3 \cos \theta \cdot dt \cdot p(v) dv d\Omega . \quad (2.12)$$

Here  $n_0$  is the number density, which is a function of temperature via the Clausius-Clapeyron relation

$$n_0(T) = p_\infty \cdot \frac{e^{-L/k_B T}}{k_B T} \quad (2.13)$$

with  $p_\infty = 2.341 \times 10^4$  Pa and  $L = 1.108 \times 10^{-19}$  J for  ${}^7\text{Li}$  [49]. The solid-angle flux of particles  $dN$  in velocity group  $dv$  emitted into the solid angle  $d\Omega$  in a time  $dt$  is

$$j(\theta, \phi, v) = \frac{dN}{dt d\Omega dv} = n_0 A_0 v^3 \cos \theta \left( \frac{m}{2\pi k_B T} \right)^{3/2} e^{-\frac{mv^2}{2k_B T}} . \quad (2.14)$$

In order to calculate the local density of this atomic beam, consider that particles emitted into  $d\Omega$  pass through an area  $dA = r^2 d\Omega$  at a distance  $r$  from the nozzle, and that these particles have moved by a distance  $v dt$  in the time  $dt$  and so are located within a volume  $d(Av)dt$ . Thus

$$dn(r, \theta, \phi, v) = \frac{dN}{dV} = \frac{dN}{d(Av)dt} = \frac{1}{v} \frac{1}{r^2} j(\theta, \phi, v) dv, \quad (2.15)$$

which can be integrated along the path of a probe beam to calculate its absorption.

Photons propagating through an atomic vapor, assumed for now to have a single electronic transition with resonant cross-section  $\sigma_0 \equiv 6\pi\lambda^2$ , are absorbed with a frequency dependent cross-section

$$\sigma(\omega) = \sigma_0 \cdot \frac{(\Gamma/2)^2}{(\omega - \omega_0)^2 + (\Gamma/2)^2}. \quad (2.16)$$

If a particle is moving at velocity  $\mathbf{v}$ , the Doppler shift is added to the detuning so that  $\sigma(\omega - \mathbf{k} \cdot \mathbf{v})$  for photon wavevector  $\mathbf{k}$ . Thus the total optical density  $\rho_{\text{OD}}$  experienced by a laser beam propagating perpendicular to the flux of the oven is an integral over all atomic velocities and along the path  $l$  of the laser beam

$$\rho_{\text{OD}} = \int_0^\infty dv \int_l dr \sigma(\omega - \mathbf{k} \cdot \mathbf{v}(\mathbf{r}, v)) dn(\mathbf{r}, v). \quad (2.17)$$

In the limit that  $k_{\text{B}}T \gg m\Gamma^2$ , atomic lineshapes can be approximated by delta functions and this line integral reduces to

$$\rho_{\text{OD}} = \frac{n_0 \sigma_0 \Gamma A_0}{4z_0 k} \sqrt{\frac{k_{\text{B}}T}{2\pi m}} \exp\left(-\frac{m}{2k_{\text{B}}T} \left(\frac{\omega - \omega_0}{k}\right)^2 \frac{1}{\sin^2 \theta_0}\right) \quad (2.18)$$

at a distance  $z_0$  from the nozzle. The resulting intensity  $I/I_0 = -\exp(\rho_{\text{OD}})$  can be used to fit the spectroscopic signals plotted in figure 2.13b in order to obtain  $\theta_0$  and  $A_0$ , from whence it is possible to calculate the effusion rate  $R = n_0 A_0 \sin^2 \theta_0 \sqrt{k_{\text{B}}T/2\pi m}$ . Given  $T = 485^\circ\text{C}$ ,  $n_0$  can be calculated from (2.18), leading to  $A_0 = 11.2 \text{ mm}^2$ ,  $\theta_0 = 5.4$  and finally  $R = 2.1 \times 10^{15}/\text{s}$ , with  $6.5 \times 10^{12}/\text{s}$  reaching the chamber.

## Differential Pumping and Beam Shutter

After leaving the oven, the atoms next pass through another collimating nozzle, or *cold cup*, whose purpose is to protect the subsequent differential pumping tubes from atomic vapor deposition. During the design phase of this experiment, it was estimated that the melting point of Lithium is so high that the cup would not require active cooling. No significant deposition has ever been observed on the cup's surface, which casts doubt on the verity of this assumption, but in any case the use of a micro-channel nozzle renders the discussion moot. Two stages of differential pumping, the second of which includes the Zeeman slower tube, separate the oven chamber, which is measured to have a pressure of  $5 \times 10^8$  Torr, from the main chamber, whose pressure is measured to be  $2 \times 10^{-11}$  Torr. A solenoid-operated beam shutter, in the form of a copper paddle attached to a vacuum bellows, is located between the two differential pumping tubes. The oven chamber, beam shutter chamber and main chamber are each continuously pumped by 60 L/min ion pumps (Varian StarCell).

## Zeeman Slower

The experiment uses a spin-flip Zeeman slower, which consists of decreasing-field and increasing-field sections pointing in opposite directions, joined at a zero-crossing. The advantage of this design is minimized fringing field in the chamber: although the magnitude of the magnetic field at the terminus of the slower is more than 400 Gauss, the fringing field due to the slower at the position of the atoms 10 cm away is less than 1 Gauss, which can be easily compensated with a low-current shim coil. The frequency of the slowing light is determined by  $kv_{cap} + \mu_B B_{final}$ : the sum of the Doppler shift corresponding to the capture velocity of the MOT  $v_{cap}$ , and the Zeeman shift experienced by the atoms at the end of the slower. It is necessary that  $B_{final} \neq 0$ , so that the slowing light can be sufficiently detuned from resonance at zero field that it does not interfere with the operation of the MOT, through which it necessarily passes. In this experiment, the detuning of the slower is chosen to be 400 MHz  $\approx 68\Gamma$ , by which point the scattering rate has been reduced from resonance by a factor of  $5 \times 10^5$ .

The slower performance saturates with a power of 40 mW, with 6% of the power in the sidebands (3% on the repumping transition at +803.4 MHz, and 3% wasted). The sidebands are created with

Scheme	Transition	Detuning ( $\Gamma$ )	Intensity ( $\text{mW}/\text{cm}^2$ )
MOT	D2, F1	-5	2.3
	D2, F2	-7	3.9
GM	D1, F1	+5	2.0
	D1, F2	+5	68.2

Table 2.1: Parameters of the cooling beams.

a home-built resonant EOM operating as a phase modulator. The slowing is optimized either by observing velocity distribution of the atomic beam with Doppler-sensitive spectroscopy, or by simply observing the initial loading rate of the MOT ( $< 500$  ms), which is linear in time and has a slope that depends on the slowing rate. The loading rate is observed to improve by about 20% when a small magnetic field ( $< 10$  G) is added in the 30 cm of differential pumping preceding the slower, providing a quantization axis along which the atoms can be optically pumped into the  $|F, m_F\rangle = |2, 2\rangle$  state, which has a cycling transition on the D2 line. This trick ensures that the atoms are prepared in the  $|2, 2\rangle$  state before they enter the Zeeman slower.

### Magneto-optic Trap

The MOT is a standard type-I configuration operating on a  $J \rightarrow J+1$  transition (in this case the D2 line). As the cooling and trapping properties of MOTs are described in many references [46, 50], this work will briefly describe only the operation and characterization of the particular implementation used in this experiment. The MOT is created from three pairs of counter-propagating, circularly polarized beams. In order to maximize capture velocity, the detunings of the F2 and F1 light are made as red as possible given the available power, such that the scattering rate on each transition remains high enough to capture the Zeeman-slowed atoms. In order to maximize the capture volume, the beams are also made as large as the chamber will permit, with a  $1/e^2$  radius of 2.5cm. The beam parameters are summarized in table 2.3. The strength of the quadrupole field is  $B'_z = 15$  G/cm, for  $\hat{z}$  along the axis of symmetry of the coils. With these parameters, the MOT is capable of loading  $5 \times 10^9$  atoms in 3 seconds.

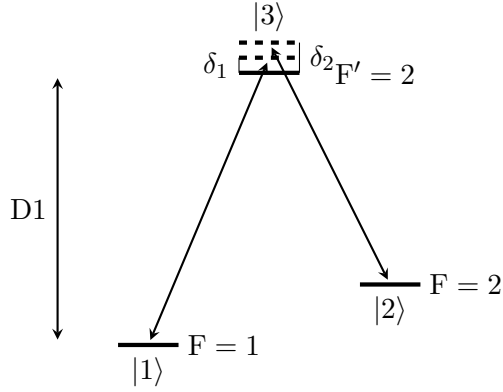


Figure 2.14: The Gray Molasses cooling level scheme.

### Compressed MOT

While the parameters of the MOT are chosen to maximize atom number and loading rate, they do not simultaneously maximize phase space density. Rather than compromise capture velocity or re-scattering by adjusting the MOT parameters during the loading, the parameters of the MOT are dynamically adjusted after the loading stage is completed. As the CMOT will be followed by a sub-Doppler cooling stage with limited beam size (7 mm, compared to 2.5 cm) the parameters of the CMOT are empirically tuned to prioritize maximum density. The detuning of the cooling light is brought close to resonance, in order to maximize compression, while simultaneously the intensity of the repumping light is lowered to zero in order to limit the scattering rate. As a result, the cloud is compressed by slightly more than a factor of two and its temperature is lowered by 30%. Somewhat surprisingly, it was found that increasing the strength of the quadrupole field did not significantly affect the density or temperature of the cloud.

### Gray Molasses

Due to the temperature dependent scattering length of  ${}^7\text{Li}$  (see section 2.1), it is necessary to cool well below the Doppler limit in order to ensure the thermalization rates required for evaporative cooling. A good choice for alkali atoms is a class of  $\Lambda$ -enhanced sub-Doppler schemes known as Gray Molasses (GM), a form of Electromagnetically Induced Transparency (EIT) cooling [51] (distinguished here from EIT-sideband cooling, which requires a trapping potential [52]) that combines the cooling of a blue-detuned  $\sigma^+ - \sigma^-$  cooling on a  $J=1 \rightarrow J'=1$  transition with the momentum-

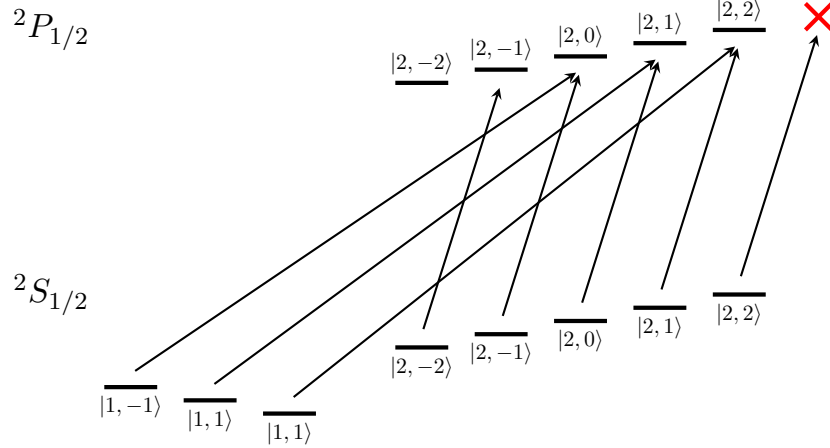


Figure 2.15: A dark state pumping scheme in which atoms collect in the  $|2, 2\rangle$  ground state. As this is the D1 transition, there is no  $F' = 3$  level in the excited state. Not pictured is spontaneous emission from the excited state, which takes atoms from the excited state to  $F = 1$  or  $F = 2$  in the ground state with  $\Delta m_F = \pm 1, 0$ .

dependent dark state mechanism of Velocity-selective Coherent Population Trapping (VSCPT) [53]. While the original GM proposal called for a 1D, single-transition molasses in  $^{87}\text{Rb}$  on the D2 line [54], subsequent iterations have expanded the scheme to other atoms and three dimensions [55, 56], and recently also simultaneous  $J \rightarrow J$  transitions (i.e. on  $F=1$  and  $F=2$  transitions) [57]. In the latter case, the motional dark state is the result of the three-level  $\Lambda$ -system depicted in figure 2.14. While the relative detuning  $\delta_1 - \delta_2$  must equal zero in order for the dark state to correspond to zero atomic velocity, the overall detuning  $\Delta$  must be positive in order for the molasses to function.

Because of the indistinguishability of the hyperfine levels within the  $^2P_{3/2}$  in  $^7\text{Li}$ , only the D1 line contains a suitable transition, as the  $^2P_{1/2}$  hyperfine levels are separated by nearly  $16\Gamma$ . The performance of the scheme is sensitive to the relative detuning  $\delta_1 - \delta_2$  at the level of  $\Gamma/10$ , but the overall detuning may be anywhere from  $4\Gamma$  to  $6\Gamma$  blue of the  $F' = 2$  excited state. The cooling rate of the molasses is improved by higher optical intensity, so the GM beams are 7 mm in diameter, which is approximately the size of the atomic cloud after the CMOT. The beam parameters are again given in table 2.3. This scheme achieves a final temperature of about  $100 \mu\text{K}$  in 4 ms with 14 mW per cooling beam, without any loss of density.

## Dark State Pumping

In order to prepare the atoms in the  $|2, 2\rangle$  state (see section 2.4.1), an  $m_F$  pumping technique is needed. In the presence of a magnetic field in order to set the quantization axis,  $\sigma^+$  light will tend to increase the angular momentum of the atoms over many scattering events so that they gather in the stretched state. If a D2 transition is used, as in the MOT, this pumping has the undesirable side effect of causing the atoms which collect in the stretched state to scatter many photons on the  $|2, 2\rangle_g \leftrightarrow |3, 3\rangle_e$  cycling transition. This leads to significant heating, negating the hard-won gains of laser cooling. The entire problem can be side-stepped by using a scheme in which the stretched state is also a dark state. The D1 transition affords just such a possibility. The strategy is to illuminate the cloud with  $\sigma^+$  light on the D1 line in the presence of a weak bias field ( $\approx 5$  G), so that atoms will scatter until they reach the  $|2, 2\rangle$  state and subsequently go dark (both F2 and F1 light are necessary, as spontaneous emission from the excited state can result in an atom populating either F=2 or F=1).

One can characterize the effectiveness of this scheme by measuring the acceleration of the cloud due to photon recoils, e.g. by imaging the cloud from the side after some pumping time. If the stretched state were perfectly dark, one would observe that the center of mass of the cloud would simply acquire a momentum equal to the photon recoil times the average number of photons necessary to pump an atom into the dark state. A dark state that is imperfect or “leaky” will, however, continue to scatter and accelerate. The final velocity of the cloud can be determined from the position of the cloud’s center of mass after a time of flight following the pumping pulse, assuming this time of flight is significantly longer than the pumping pulse. The measured velocity normalized by the recoil velocity  $v_R = \sqrt{\hbar^2 k^2 / m^2}$  gives the number of photons scattered. In the scheme implemented here, these data suggest the scattering rate asymptotes to about 3 photons/ms (see figure 2.16), which, while not perfect, is at least suppression by more than forty times of the initial scattering rate of 125 photons/ms. This may be due to imperfect alignment of the pumping light with the bias field, or to imperfect  $\sigma^+$  polarization, but in either case the scheme pumps nearly all of the atoms into the dark state within half a millisecond with minimal excess heating.

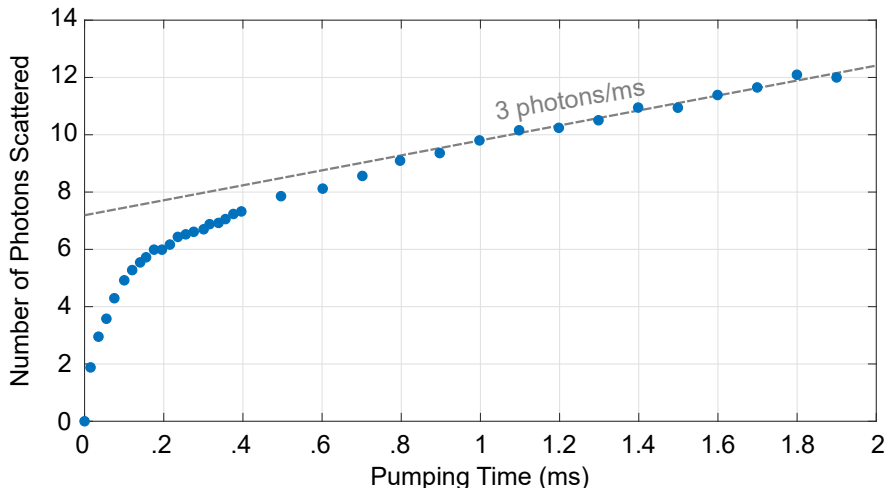


Figure 2.16: Suppression of scattering from the dark state. The dashed line is a linear fit to the data at the ten longest times, whose slope shows the asymptotic behavior of the scattering cross-section as the atoms are pumped into  $|2, 2\rangle$ .

## 2.4 Evaporation

Even using a sub-Doppler cooling scheme, the phase space density achieved by laser cooling in  ${}^7\text{Li}$  is only  $5 \times 10^{-5}$ , which is still five orders of magnitude lower than  $\rho_{\text{crit}}$  (see section 1.3.1). Although the first condensate of  ${}^7\text{Li}$  was formed by solo evaporative cooling of  ${}^7\text{Li}$  in a magnetic trap, to this author's knowledge all successive  ${}^7\text{Li}$  condensates have been made by evaporating a mixture of  ${}^6\text{Li}$  and  ${}^7\text{Li}$ . The mixture has the advantage that the inter-species scattering length is about a factor of two larger than the scattering length of  ${}^7\text{Li}$  with itself. This section describes the development of a forced evaporative cooling scheme for  ${}^7\text{Li}$  alone, using both magnetic and optical traps in succession.

### 2.4.1 Magnetic Trap Evaporation

In principle, it would be ideal to transfer the laser-cooled atoms directly to an optical dipole trap (ODT), in which the scattering length can be adjusted to a large and positive value via a Feshbach resonance, so that evaporation can proceed with maximum efficiency. The light mass of  ${}^7\text{Li}$ , however, requires a significant investment in optical power: a 10 W optical dipole trap beam with a  $1/e^2$  waist of  $100 \mu\text{m}$  gives a trap depth for  ${}^7\text{Li}$  of about  $100 \mu\text{K}$ , which is on the order of the lowest achievable temperature via laser cooling. A crossed ODT made from such beams would,

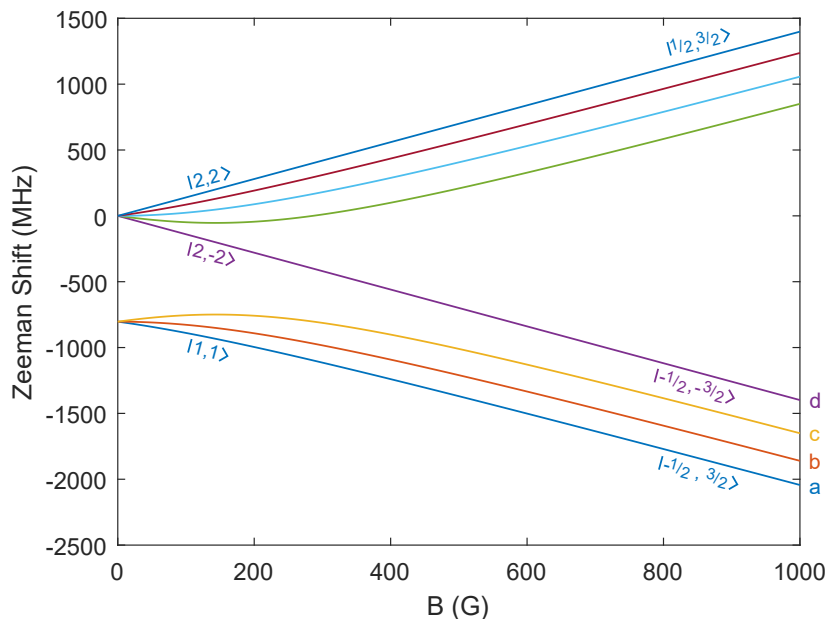


Figure 2.17: Hyperfine structure of  ${}^7\text{Li}$  in a magnetic field. The low-field states, dominated by spin-orbit coupling, are labeled with the quantum numbers  $|F, m_F\rangle$ , where  $F=I+S$ , while the high field states are labeled with the quantum numbers  $|S, I\rangle$  and are indexed (a,b...) in ascending order.

however, have terrible overlap with the spacial distribution of the laser-cooled cloud, which is a few millimeters in diameter. Just from overlap considerations, the captured number of particles would be about  $10^5$ , which is far too low: evaporation should *end* with about  $10^5$  atoms in the condensate. The ODT beams could be made larger in order to increase spatial overlap, but that would require higher optical power, which is expensive and difficult to fiber-couple.

### Trappable states

Instead, a short step of evaporation in a highly compressed magnetic trap can boost the density and lower the temperature enough to efficiently stitch together laser cooling and ODT evaporation.  ${}^7\text{Li}$  has three magnetically trappable states at low fields (figure 2.17). Near  $|B| = 0$  the  $|1, -1\rangle$  and  $|2, 1\rangle$  states both have slopes of half a Bohr magneton, whereas  $|2, 2\rangle$  is a stretched state and therefore always has the slope of the full Bohr magneton. In the  $|1, -1\rangle$  state the magnetic moment goes through a minimum and changes sign at around 160 G, limiting the achievable trap strength; both the  $|1, -1\rangle$  and  $|2, 1\rangle$  states are susceptible to spin-changing collisions which lead to losses, which as a stretched state the  $|2, 2\rangle$  is not, and in any case the greatest trap strength is achieved using the highest magnetic moment (in principle, dipolar relaxation is still available as a loss channel,

but the rate is too low to measure in bulk).

The tightest possible confinement is achieved by use of a quadrupole trapping potential  $|B_{\text{trap}}|^2 = (B')^2 \cdot (x^2/4 + y^2/4 + z^2)$ . The use of a quadrupole trapping potential has one caveat, which is a magnetic field zero at its center, where passing atoms can be spin-flipped to an untrapped state. This “Majorana hole” introduces a single-particle loss rate which is proportional to the peak density of the cloud, and thus increases with the phase space density. In this experiment, the atoms are kept away from this region by a repulsive potential created by a 10 W, 532 nm beam with a waist of about 23  $\mu\text{m}$ , which is on for the duration of the magnetic trap evaporation.

### Adiabatic compression

The effects of adiabatic compression in a quadrupole trap can be derived from simple scaling arguments. It is possible to define a characteristic length  $\tilde{x} = k_{\text{B}}T/(\mu_{\text{B}}B')$  and also a characteristic momentum  $\tilde{p}^2/(2m) = k_{\text{B}}T$  for temperature  $T$ , atomic mass  $m$  and magnetic field trapping gradient  $B'$ . Adiabatic changes in this trap strength imply  $\tilde{x}\tilde{p} = \text{const}$  such that  $T \sim (B')^{2/3}$  in such a trap. Thus the density scales as  $n \sim 1/\tilde{x}^3 \sim (B'/T)^3 \sim B'$ . Most importantly, these two results can be combined to show that the two-body elastic collision rate  $n\sigma v$  scales as  $(B')^{4/3}$ . This collision rate determines the equilibration rate of thermal distributions and is critical for efficient evaporative cooling.

### RF-induced evaporative cooling

The principle behind evaporative cooling is the removal of energy from a trapped gas by removing the most energetic particles: that is, the particles in the high-energy tail of the Maxwell-Boltzmann distribution. In a magnetic trap, it is straightforward to achieve this culling by using RF transitions between trapped and untrapped Zeeman sublevels [58]. The most energetic atoms explore highest parts of the trapping potential, and thus experience the largest Zeeman shifts, so it is possible to choose a radio frequency such that only these atoms are spin-flipped. The cutoff energy can be described by multiples of the mean kinetic energy of the atoms  $\eta \equiv E_{\text{cut}}/(1/2m\bar{v}^2)$ .

The hyperfine structure of  ${}^7\text{Li}$  presents two options for this spin flip: the atoms can be transferred to the lower half of the  $F = 2$  manifold (often referred to as “ $m_{\text{F}}$  evaporation”), or directly to the  $|1, 1\rangle$  state (referred to as “hyperfine evaporation”). The two options further are characterized

by different frequency requirements. Whereas  $m_F$  evaporation requires RF between 100 MHz and 1 MHz, hyperfine evaporation requires RF between 1 GHz and  $E_{\text{hfs}}/h = 803.5$  MHz. It was found that  $m_F$  evaporation interferes with other low-frequency lab equipment, such as the Doppler-free spectroscopy locking scheme for the diode lasers; and since the high- $|B|$  spin flips performed later in the experiment require a 100 MHz - 1 GHz amplifier and antenna anyway, hyperfine evaporation was selected.

A trapped gas of particles with contact interactions reaches thermal equilibrium through collisions— in two dimensions and higher, elastic two-particle collisions can redistribute kinetic energy and momentum. However, collisions also present an opportunity for particle loss and heating, whether by changing the internal state of the particles or via a chemical reaction that changes the spatial component of the two-body wavefunction. A sample of atoms in a single hyperfine state (a “spin-polarized” sample) may decay to a mixture of states, subject to the constraints of angular momentum conservation. These states may be untrapped, leading directly to loss, or in the presence of the trapping magnetic field may convert enough Zeeman energy to kinetic energy that they escape the trapping potential (see figure 2.17). At ultracold temperatures, two-particle chemical reactions are ruled out by the need to both conserve the center of mass momentum of the two-particle system and to find a place to put the energy liberated by the chemical bond. When three particles collide, however, there is a chance for two of them to form a molecule while the third carries away the binding energy (which can be hundreds of recoils), which results in the loss of all three particles. As both the two- and three-body loss processes scale with density (as  $n$  and  $n^2$ , respectively), they will tend to heat a gas trapped in a non-uniform potential by removing particles with below-average kinetic energy from the coldest and densest part of the trap.

Due to ever-present single particle losses caused by background gas collisions, it is desirable to evaporate as quickly as possible. The constraint is the thermalization rate of the trapped gas, proportional to the two-body collision rate  $n\sigma v$  for collisional cross section  $\sigma$  and average velocity  $v$ . Therefore it is desirable to compress the cloud as much as possible. On the other hand, the rate of three-particle collisions is  $\Gamma_3 n^2$ , for three-body loss coefficient  $\Gamma_3$ . The ratio of two-to-three particle collision rates is then  $\sigma v/\Gamma_3 n$ . Optimization of forced evaporative cooling is thus equivalent to finding a route to degeneracy in which the density of the atomic sample is controlled in such a way as to keep the two-body collision rate high and to simultaneously straddle the constraints of

single- and three-body losses.

### Optimization of Evaporative Cooling

When the scattering length is small, as is the case in  ${}^7\text{Li}$ , the key to fast and efficient evaporation is compression. There are really two aspects to this: the maximum achievable gradient, and gradient at which the atoms can be caught after laser cooling. These two endpoints determine the compression factor  $B'_{\text{max}}/B'_{\text{capture}} \equiv \alpha$ . The maximum achievable density is therefore  $\alpha \cdot n_{\text{capture}}$  and the two-body collision rate receives a boost  $\alpha^{4/3}$ , via the scaling arguments introduced in the previous section. The coils whose design was introduced in section 2.2.3 are capable of compressing the laser-cooled cloud by a factor of 5, which boosts the elastic collision rate by a factor of about 8.5.

Compression optimizes the starting conditions, but it still remains to determine the  $\text{RF}(t)$  and  $B'(t)$  that maximize cooling efficiency. Various optimization techniques exist, many of which are reviewed in [58]. First of all, the most efficient path is the one which optimizes the efficiency at each point, so that the frequency ramp can be tuned experimentally by breaking it into a number of linear segments and optimizing each separately. It is further possible to assume that the distribution of kinetic energies amongst the atoms follows a (truncated) Maxwell-Boltzmann distribution at all times, in which case the problem of optimizing evaporation amounts to solving a pair of coupled differential equations for  $\dot{N}/N$  and  $\dot{T}/T$ . An alternative approach, originally introduced by Foot and Wu [59], is to run a Monte-Carlo simulation of the full dynamics of the trapped gas, including kinetics, losses, and collisions. This method has the advantages that it makes for relatively straightforward incorporation of various sorts of losses and energy-dependent scattering, and it does not assume anything about the distribution of kinetic energies of the atoms. A version of this approach is used to optimize the evaporation procedure in this work. It does, however, assume classical statistics and non-hydrodynamic densities (both of which are valid for the regimes modeled in this work). The DSMC algorithm, which simulates the dynamics of  $N$  particles with  $N/p$  representative particles, can be summarized as follows:

1. Initialize  $N/p$  particles (results converge for  $N/p > 10^5$ ).
2. Advance a time  $dt$ .

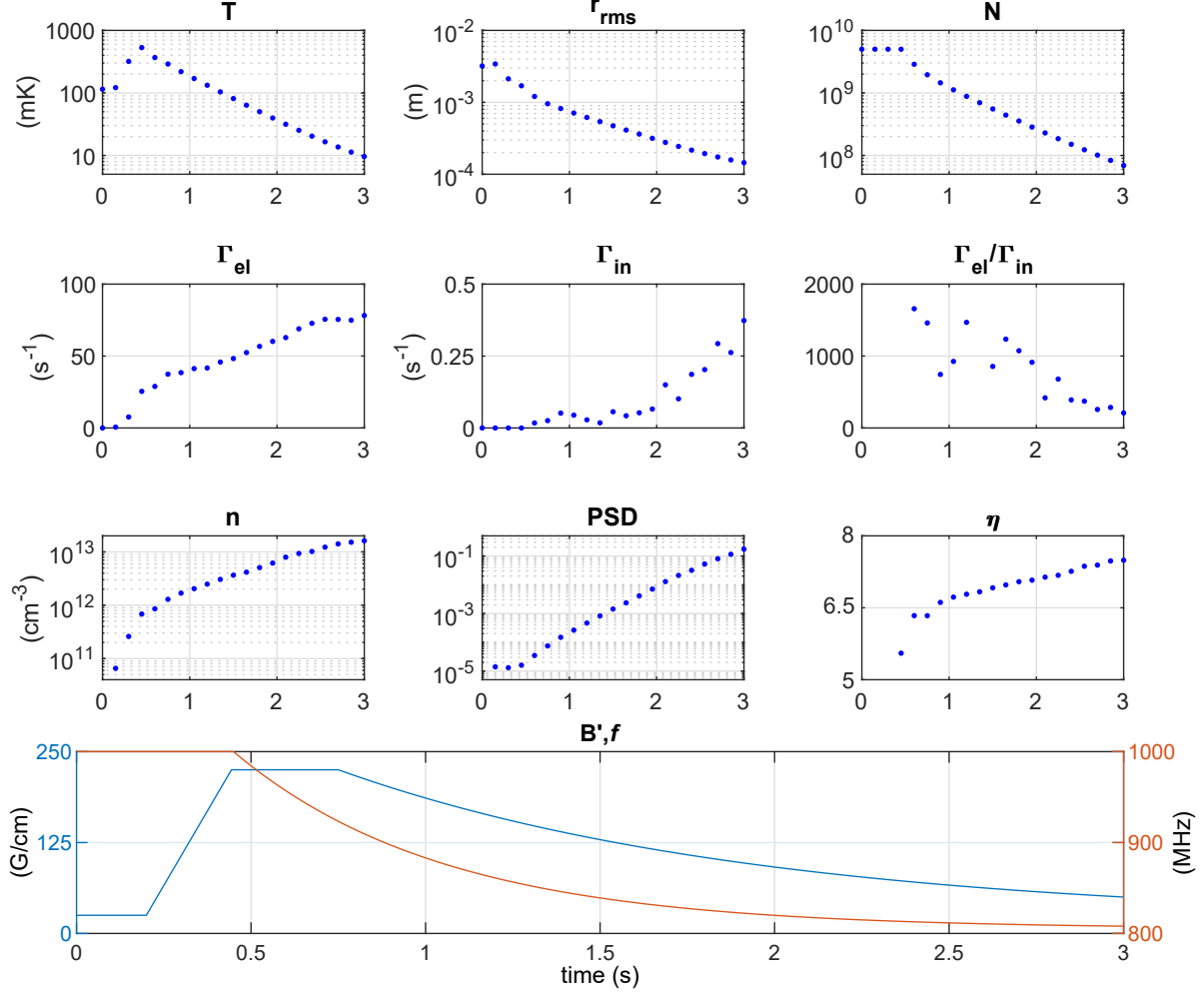


Figure 2.18: Output of the DSMC evaporation optimizer when the evaporation time has been set to 2.5 s.  $5 \times 10^9$   ${}^7\text{Li}$  atoms at  $100 \mu\text{K}$  are brought to just below degeneracy with an efficiency of  $\gamma=2.2$  in an optical quadrupole trap. The strength of the quadrupole field  $B'$  is reported as the transverse gradient in G/cm (the Z-gradient is twice as large).  $\Gamma_{in}$  is the loss rate per particle due to the combined effects of background gas collisions, dipolar relaxation and three-body recombination.  $T$  is defined via the average kinetic energy of the particles, although the particle velocities are not restricted to follow a Maxwell-Boltzmann distribution.  $n$  is the peak density,  $r_{rms}$  is the root-mean-square cloud radius in the transverse direction, and  $\eta$  is the potential energy of the spin-flipped atoms normalized by  $k_B T$ .

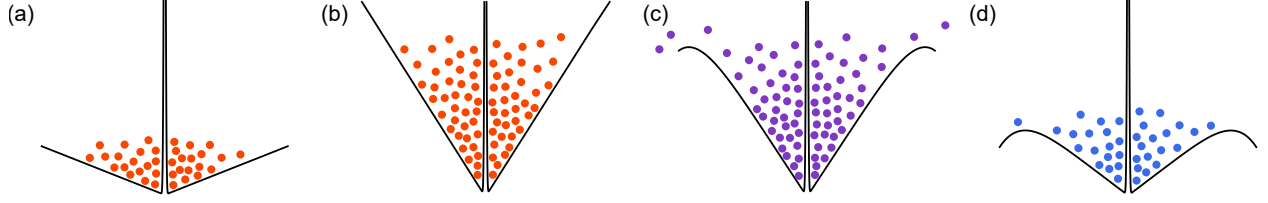


Figure 2.19: Cuts along an axis of the optically-plugged quadrupole trap during different stages of evaporation. (a) Atoms are captured in a mode-matched magnetic trap. (b) The atomic cloud is adiabatically compressed by ramping up the magnetic potential. (c) RF spin flips remove the most energetic atoms from the edges of the trap. (d) The trap is adiabatically decompressed while RF evaporation continues, in order to manage density-dependent losses.

3. Update positions and velocities of atoms moving in the conservative trapping potential by solving Newton's equations, e.g. using symplectic integration such as the Beeman algorithm.
4. Bin the atoms into 3D cells.
5. Compute two-particle collisions using Bird's constant-time NTC algorithm [60] and update particle velocities.
6. Compute density-dependent particle losses in cells.
7. Redraw the grid of 3D cells and adjust particle weight  $p$  to remain at a constant number of simulation particles and return to step 2.

By using this simulator, it is possible to optimize the path the evaporated cloud traces through phase space, given certain constraints (e.g. on the total time). That is the approach followed here: the optimizer adjusts the RF and trap compression ramps in a piece-wise fashion in order to reach a target PSD within a given time. For example, it finds an evaporation procedure that increases the PSD by more than four orders of magnitude in 2.5 s with an efficiency of  $\gamma \equiv \log(\rho_i/\rho_f)/\log(N_i/N_f) = 2.2$ , which is remarkably good for an atom with such a small collisional cross-section. The results of the simulation are found to be highly consistent with the experiment; in fact, the number of atoms with which the target PSD is reached in the experiment is slightly higher than predicted, suggesting that the rates for one or another loss processes are over-estimated (but the optimal path turns out not to be terribly sensitive to collisional loss rates, as long as adiabatic decompression maintains the density at a level where  $\tau_{\text{loss}}$  per atom is much shorter than remaining evaporation time).

## 2.4.2 Optical Dipole Trap Evaporation

The difficulty posed by the attractive interactions the  $|2, 2\rangle$  state must be addressed before BEC can be achieved. The lowest two hyperfine states of  ${}^7\text{Li}$  ( $|1, 1\rangle$  and  $|1, 0\rangle$  at low field,  $a$  and  $b$  at high field, as in figure 2.17) have Feshbach resonances around 740 G and 940 G respectively; further  $|1, 1\rangle$  is the absolute spin ground state, so no two-body losses can occur. It is therefore in either the  $|1, 1\rangle$  or  $|1, 0\rangle$  state, at a magnetic field where the scattering length is about  $150a_0$ , that the final evaporation to BEC takes place. Both choices of hyperfine state are incompatible with magnetic trapping, so the atoms are transferred to an optical dipole trap (ODT), which uses the conservative potential arising from the AC-Stark shift to trap the atoms in a focused beam of light.

### Optical Dipole Trapping

The conservative (induced dipole potential) and non-conservative (scattering) aspects of the light force can be expressed as

$$U_{\text{dip}}(\mathbf{r}) = -\frac{3\pi c^2}{2\omega_0^3} \left( \frac{\Gamma}{\omega_0 - \omega} + \frac{\Gamma}{\omega_0 + \omega} \right) I(\mathbf{r}) \equiv s(\omega)I(\mathbf{r}) , \text{ and} \quad (2.19)$$

$$\Gamma_{\text{sc}}(\mathbf{r}) = \frac{3\pi c^2}{2\hbar\omega_0^3} \left( \frac{\omega}{\omega_0} \right)^3 \left( \frac{\Gamma}{\omega_0 - \omega} + \frac{\Gamma}{\omega_0 + \omega} \right)^2 I(\mathbf{r}) \quad (2.20)$$

for laser frequency  $\omega$ , transition frequency  $\omega_0$ , natural linewidth  $\Gamma$ , and intensity distribution  $I(\mathbf{r})$  [61]. The detuning and optical power should be chosen such the light can provide enough trap depth to contain atoms with kinetic energy  $k_{\text{B}}T_{\text{evap}}$ , while simultaneously keeping the characteristic scattering time  $2\pi/\Gamma_{\text{sc}}$  long compared to the duration of the experiment. In the context of small detuning  $\delta = \omega - \omega_0$ , the term that depends on  $1/(\omega + \omega_0)$  becomes negligible, leading to

$$\frac{U_{\text{dip}}}{\hbar\Gamma_{\text{sc}}} \approx \frac{\delta}{\Gamma} . \quad (2.21)$$

Formulation in this *rotating wave approximation* makes it clear that the strategy should be to detune as far as possible, given constraints on optical power. However, for extremely large detunings, this approximation significantly underestimates both the induced dipole potential and scattering rate. Without inclusion of the counter-rotating term, trapping forces due 1064 nm light on  ${}^7\text{Li}$ , which has an S $\rightarrow$ P transition at 671 nm, would be underestimated by about 40%.

The ODT itself takes the form of a Gaussian beam propagating in the  $\hat{z}$  direction, described by

$$I(r, z) = I_0 \frac{e^{-2\frac{r^2}{w_0^2}}}{1 + (z/z_R)^2} \quad (2.22)$$

where  $w_0$  is the  $1/e^2$  beam waist and  $z_R = \pi w_0^2/\lambda$  is the Rayleigh length.  $I_0 = 2P/\pi w_0^2$  is the peak intensity for a beam with total optical power  $P$ . An atom located near the focus of such a beam will experience an approximately harmonic dipole potential

$$U(r, z) \approx \frac{1}{2}m(\omega_r^2 r^2 + \omega_z^2 z^2) \quad (2.23)$$

where  $\omega_r = \frac{\sqrt{s(\omega)}}{w_0^2} \sqrt{8P/\pi m}$  and  $\omega_z = \frac{\sqrt{s(\omega)}}{w_0 z_R} \sqrt{4P/\pi m}$ . As the Rayleigh length scales like  $1/w_0^2$ , the longitudinal confinement provided by a single beam is much weaker than the transverse confinement (unless the beam is focused to a wavelength-sized spot). In order to achieve more symmetric confinement of the atomic cloud, and therefore higher densities, this apparatus uses two beams that cross at  $45^\circ$ . With beam parameters of  $\lambda = 1064$  nm,  $w_0 = 100$   $\mu\text{m}$ , and  $P = 5$  W, the ODT beams each achieve a radial trapping frequency for  ${}^7\text{Li}$  of 2 kHz and a depth  $sI_0/k_B$  of 70  $\mu\text{K}$ .

Due to poor spatial overlap, the ODT can only capture 10% of the atoms prepared by evaporation in the magnetic trap. After loading the atomic cloud into the ODT, an RF sweep causes a hyperfine transition  $|2, 2\rangle \rightarrow |1, 1\rangle$  in 10 ms with close to 100% fidelity. A gradient of 10 G/cm is applied in order to clear atoms out of the wings of the ODT. The cleanup step may be followed by another sweep into the  $|1, 0\rangle$  state, depending on whether an  $a$ - or  $b$ -condensate is to be made. The main coils then ramp the bias field to  $B_{\text{evap}}$ .

### Evaporative Cooling to Degeneracy

At this point, the atom number with which BEC is reached can be adjusted lower by ramping the magnetic field towards the Feshbach resonance for some time, in order to induce three-body loss. In this way, BEC numbers between  $1 \times 10^4$  and  $5 \times 10^5$  can be reached via the same evaporative cooling parameters, with fluctuations of  $\pm 3\%$  and without loss of condensate fraction. After adjusting the starting number, evaporation in the  $|1, 1\rangle$  or  $|1, 0\rangle$  state proceeds quickly because a scattering length can be selected that affords the best ratio of elastic to inelastic collisions (about  $150a_0$ , at 730 G or

870 G, depending on the hyperfine state). The depth of both ODTs are lowered exponentially over 2 s with a time constant of 500 ms in the presence of a magnetic field gradient equal to 8 times the force of gravity, which helps to spill the light Lithium atoms from the trap.

### Limits of evaporative cooling

After crossing the BEC transition, the collisional density of the sample leads to fast thermalization times and ought to result in extremely efficient evaporation. Further cooling, however, tends to be hampered by the fact that the *in situ* size of the thermal cloud remains determined by the temperature, while the size of the condensate is determined by the condensate number and interactions (in the Thomas-Fermi limit). (In reality, there is some interplay between the size of the condensate and the size of the thermal cloud, because the presence of the BEC modifies the trapping potential experienced by the thermal atoms, at least at the center of the trap.) In order to avoid cutting into the condensate while evaporating, which would tend to heat the sample, the  $\eta$  of the evaporation may have to become prohibitively high, leading evaporation to stall. This can to some extent be limited if interactions can be tuned via a Feshbach resonance, so that the BEC radius can be made smaller, at the price of increasing the density and exposing the sample to three-body losses, but is typically only a consideration at very high condensate fractions ( $> 95\%$ ).

## 2.5 Summary of Cooling Results

The excellent performance of the cooling sequence is contingent upon two accomplishments: (1) the final temperature achieved by laser cooling is low enough that the compression ratio of the magnetic trap is high and the temperature-dependence of the scattering length does not play a role, and (2) adiabatic compression kick-starts the evaporative cooling process, followed by decompression in order to keep the time constant of three-body loss above a second. As a result, BECs with  $> 10^5$  atoms and high condensate fraction ( $> 95\%$  is too high to fit reliably) can be made in the  $|1, 1\rangle$  or  $|1, 0\rangle$  state in about 8 seconds.

Cooling Step	Duration (ms)	N	$n_0$ ( $\text{cm}^{-3}$ )	T ( $\mu\text{K}$ )	$\rho_0$
MOT	3000	$2 \times 10^9$	$1 \times 10^{11}$	1200	$1 \times 10^{-6}$
CMOT	4	$2 \times 10^9$	$2 \times 10^{11}$	700	$1 \times 10^{-6}$
GM	4	$1 \times 10^9$	$2 \times 10^{11}$	100	$5 \times 10^{-5}$
DSP	0.6	$1 \times 10^9$	$2 \times 10^{11}$	100	$5 \times 10^{-5}$
MT (Capture)	100	$1 \times 10^9$	$2 \times 10^{11}$	120	$4 \times 10^{-5}$
MT (Compressed)	250	$1 \times 10^9$	$5 \times 10^{12}$	410	$4 \times 10^{-5}$
MT (Evaporation)	2500	$5 \times 10^7$	$2 \times 10^{13}$	8	0.25
ODT (Capture)	500	$5 \times 10^6$	$4 \times 10^{13}$	35	0.05
ODT (Evaporation)	2000	$5 \times 10^5$	$1 \times 10^{13}$	0.65	5.5

Table 2.2: The duration of each cooling step, as well as the atom number, peak density, temperature, and phase space density it achieves.

## Chapter 3

# A Platform for Simulations

## Atoms in Optical Lattices

### 3.1 An Atom in an Optical Lattice

In this thesis, the role of the optical lattice is to create localized Fock states which will form the sites of a lattice spin model. Its initialization is therefore the first leg of the adiabatic connection between the superfluid ground state and the ground state of said spin model. Atoms in an optical lattice are analogs of electrons in a solid crystal, where the lattice sites correspond to potential wells of nuclei. As in a solid material, the periodic external potential changes a particle’s effective mass, modifying relationship between the its energy and its momentum. Derivation of this single-particle *band structure* in that context is readily available in textbooks [62, 63], but bears repeating here because of its central importance in the discussion to follow.



Figure 3.1: Render of a standing wave of light, formed by retro-reflecting a Gaussian beam. The potential experienced by the atoms is in the region of the focus between two lenses, where the light is most intense and the longitudinal variation of the transverse beam profile is simultaneously minimized. The lattice spacing is exaggerated for clarity.

#### 3.1.1 Optical Lattice Potentials

The simplest optical lattice– and the one used throughout this work– is formed by retro-reflecting a laser beam,  $Ee^{i(kz-\omega t)}$ , upon itself. Here  $k = 2\pi/\lambda$  is the wavevector and  $\omega = 2\pi c/\lambda$  is the optical frequency. The resulting standing wave is of the form

$$V(\mathbf{r}) \cos^2(kz) \tag{3.1}$$

where  $V(\mathbf{r}) = 4 \cdot s(\omega) \cdot I(\mathbf{r})$  is the depth of the lattice and carries units of the recoil energy  $E_R$ . One factor of two comes from retro-reflection, and the other from interference, while  $s$  is a wavelength-dependent parameter which relates potential energy to intensity, defined as in (2.19). The resulting optical potential is a stack of “pancakes” along the  $\hat{z}$  axis, with a transverse envelope arising from

the curvature of the Gaussian beams, as in (2.22), and is illustrated in figure 3.1. To form a potential akin to an array of tubes, one must overlap an orthogonal, non-interfering lattice beam with the first. The non-interference condition may be realized either by orthogonal polarizations, or by sufficiently detuning the frequency of the orthogonal lattice beams so that the interference *between* them creates beat frequencies that are higher than any inter-band transitions present in the lattice. Adding a third mutually orthogonal lattice beam results in a cubic array of point traps.

### 3.1.2 Wavefunctions in a Lattice: The Momentum Basis

The behavior of an atom in the lattice is governed by the one-dimensional Schrödinger equation

$$\left(\frac{\hat{p}^2}{2m} - V(x)\right)\psi(x) = E\psi(x) \quad (3.2)$$

where the momentum operator is  $\hat{p} = -i\hbar\partial/\partial x$  and the potential energy  $V(x) = V_{\text{lat}}(x) + V_{\text{trap}}(x)$  has short-range structure due to the optical lattice and long-range variation due to the Gaussian curvature of the lattice beams and optical traps. Making the approximation that  $V_{\text{trap}}$  does not vary on the scale of the periodicity of the lattice, one may invoke Bloch's theorem in order to write the eigenstate  $\psi_q^{(n)}$  as a plane wave with quasimomentum  $q$  times a scalar function  $u_q^{(n)}(x) = u_q^{(n)}(x + \pi/k)$  that has the same periodicity as the lattice:

$$\phi_q^{(n)} = u_q^{(n)}(x)e^{iqx/\hbar} . \quad (3.3)$$

Here  $n$  labels the eigenvalues and in the context of a lattice potential is called the “band index.” Plugging in this trial wavefunction gives

$$\left(-\frac{1}{2m}(\hat{p} + q)^2 - V(x)\right)u_q^{(n)}(x) = Eu_q^{(n)}(x) \quad (3.4)$$

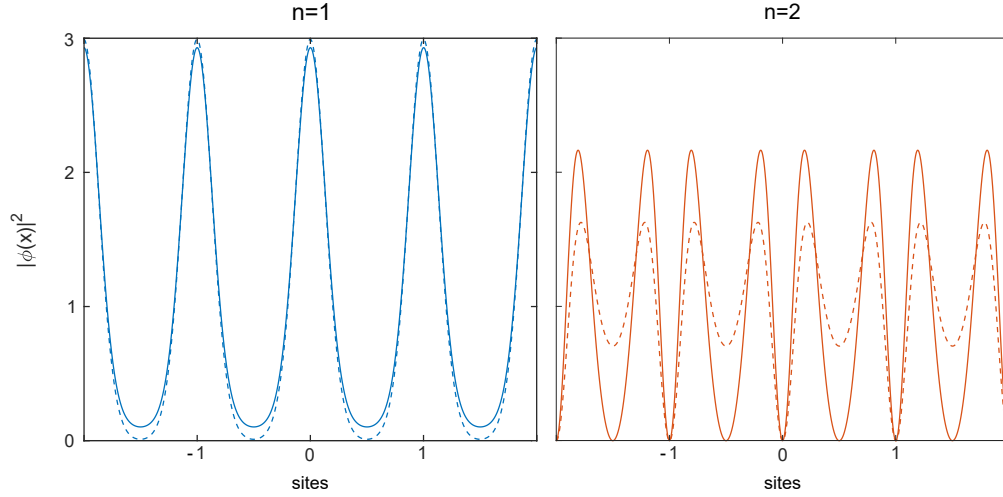


Figure 3.2: The square norms of the Bloch functions in the ground and first excited bands ( $n=1,2$ ) of a lattice with a depth of  $10 E_R$ . The solid lines depict the Bloch functions at  $q=0$ , while the dashed lines are at  $q=\hbar k$ .

where the common phase factor has been dropped. Both  $u_q^{(n)}(x)$  and  $V(x)$  have the same periodicity  $\pi/k$ , so their Fourier decompositions are sums of plane waves with wavevector  $2k$ :

$$V(x) = \sum_r V_r e^{i2rkx} , \text{ and} \quad (3.5)$$

$$u_q^{(n)}(x) = \sum_l c_l^{(n,q)} e^{i2klx} . \quad (3.6)$$

Thus the Bloch functions are superpositions of plane waves with wavevectors  $q/\hbar + 2kl$ , with  $q$  defined between  $-\hbar k$  and  $\hbar k$ . This range of quasimomenta is known as the first Brillouin zone. Given the Fourier decomposition (3.5) of the Bloch functions, the potential energy term of the Schrödinger equation can be re-expressed as

$$\begin{aligned} V(x)u_q^{(n)}(x) &= \sum_r \sum_{l'} V_r e^{i2(r+l')kx} c_{l'}^{(n,q)} \\ &= \sum_r \sum_l V_r e^{i2lkx} c_{l-r}^{(n,q)} \end{aligned} \quad (3.7)$$

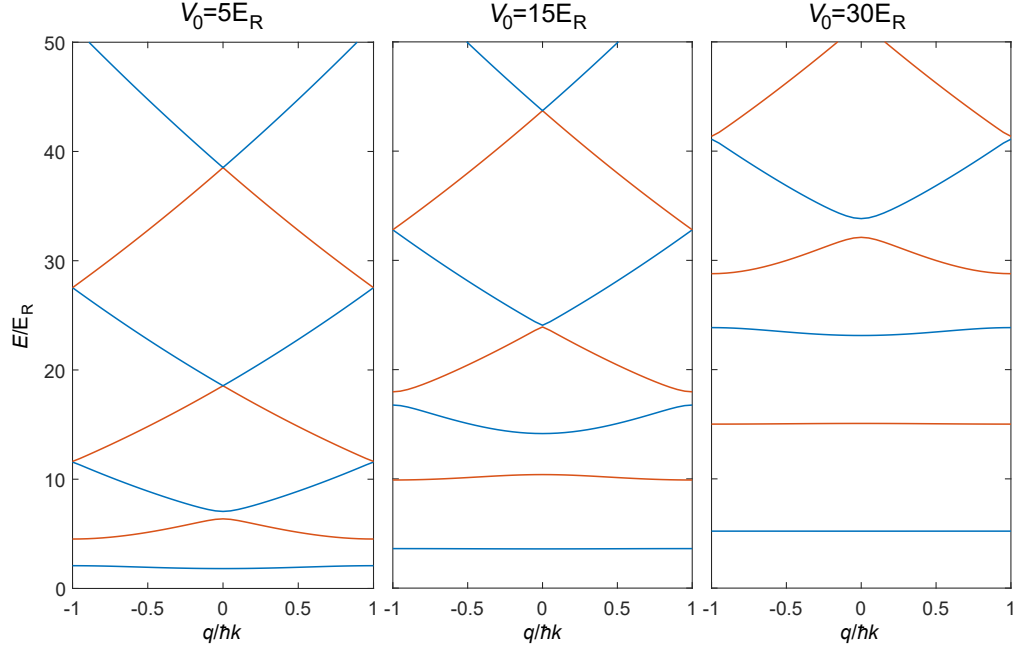


Figure 3.3: The band structure is plotted for several lattice depths as a function of quasimomentum, ranging over the first Brillouin zone.

while the kinetic energy becomes

$$\frac{1}{2m}(\hat{p} + q)^2 u_q^{(n)}(x) = \sum_l \frac{(2\hbar k + q)^2}{2m} c_l^{(n,q)} e^{i2lkx} . \quad (3.8)$$

The optical lattice potential (3.1) is itself a sum of counter-propagating plane waves

$$V(x) = V \cos^2(kx) = \frac{V}{4}(e^{i2kx} + e^{-i2kx} + 2) \quad (3.9)$$

so that the only non-zero coefficients  $V_r$  are  $V_0 = V/2$  and  $V_{\pm 1} = V/4$ . Finally, the Schrödinger equation can be recast in the form

$$\sum_{l'} H_{ll'} c_{l'}^{(n,q)} = E_q^{(n)} c_l^{(n,q)} \quad (3.10)$$

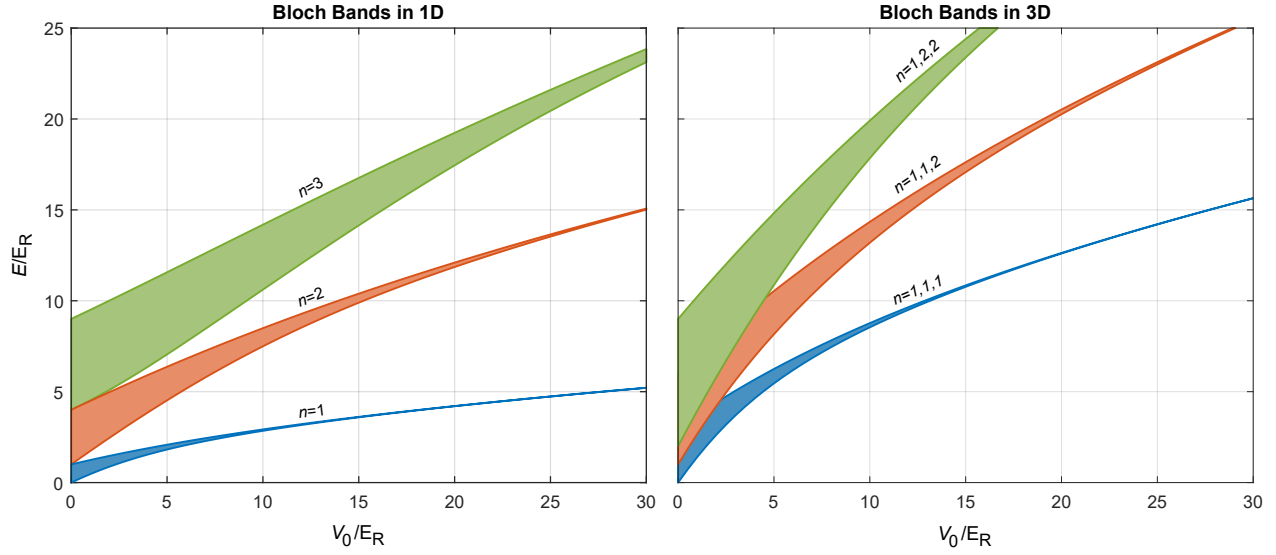


Figure 3.4: The first three bands of the lattice, plotted in 1D and 3D as a function of the lattice depth in recoils. In 3D, one quanta of excitation is added per band. While the bands are fully separated at all non-zero lattice depths in 1D, the ground and first excited band do not fully separate in 3D until about  $2.3 E_R$ .

with the matrix elements

$$H_{ll'} = \begin{cases} (2l + q/\hbar k)^2 E_{\text{rec}} + V/2 & \text{if } l = l' \\ V/4 & \text{if } |l - l'| = 1 \\ 0 & \text{else} \end{cases} \quad (3.11)$$

This matrix, truncated at some sufficiently large  $|l| \gg n$ , can be numerically diagonalized in order to obtain the eigenenergies and eigenvectors (higher energy waves and do not contribute significantly to the lowest energy eigenvalues or their associated eigenvectors). The eigenenergies, calculated as a function quasimomentum, are arranged in continuous bands with periodic boundary conditions (figure 3.3), and the eigenvectors define the coefficients  $c_l^{(n,q)}$  which can in turn be used to reconstruct the Bloch waves  $\psi_q^{(n)}$  (figure 3.2). At zero lattice depth, the band structure simply resembles the dispersion relation of a free particle (modulo  $\hbar k$ ), and the Bloch functions are simply single-frequency plane waves. As the depth of the lattice is increased, a gap opens at the edges of the band structure ( $q = \pm \hbar k$ ), and the width of the bands decrease to zero, starting with the ground band. At very large lattice depths, each lattice site is effectively an isolated harmonic

oscillator and so the lower bands become entirely flat and the gaps approach  $\hbar\omega$ .

Due to the separability of the Hamiltonian, the Bloch wavefunctions in multiple dimensions are simply products of the independent wavefunctions in each dimension. The energies are therefore the sums of the eigenenergies associated with those Bloch waves. It is then evident the band structure changes both quantitatively and qualitatively, depending on the dimensionality of the lattice (figure 3.4). In a single dimension the bands are always gapped for  $V > 0$ , but in three dimensions the first excited band has a minimum energy  $2 \times E_0^{(0)} + E_0^{(1)}$  which is lower than the maximum energy of the ground state  $3 \times E_{\pm\hbar k}$ . In fact, the bands do not fully separate until approximately  $2.3 E_{rec}$ .

### 3.1.3 Wavefunctions in a Lattice: The Position Basis

The Bloch wavefunctions are momentum eigenstates and are thus completely delocalized in position-space. If one wishes to know the wavefunction of an atom localized on the  $i$ th site of a lattice, one must construct a coherent superposition of all Bloch waves that maximizes the probability to find the atom on site  $i$ , which is to say one must find the phase factors by which to multiply the Bloch waves so that they interfere constructively on the site [64]. This can be accomplished by taking

$$w^{(n)}(x - x_i) = \frac{1}{\sqrt{M}} \sum_q e^{-iqx} \phi_q^{(n)}(x) \quad (3.12)$$

where  $\phi_q^{(n)}$  are the (normalized) Bloch wavefunctions and  $M$  is the number of quasimomenta in the range of the sum. These so-called Wannier wavefunctions, while not eigenstates of the Hamiltonian, are extremely useful for describing the state of an atom localized by a deep lattice or by interactions with atoms on neighboring lattice sites. In a 3D cubic lattice, the Wannier functions are simply products of the 1D Wannier functions  $w^{(n)}(\mathbf{x}) = w^{(n_x)}(x)w^{(n_y)}(y)w^{(n_z)}(z)$ . In very deep lattices, the on-site potential of the lattice approaches a harmonic trap, i.e.  $V_0 \sin^2(kx) \approx V_0 (kx)^2$  for  $kx \ll 1$ , so that in low-energy bands the Wannier functions approach the solutions to the quantum harmonic oscillator. For example, in the ground state,

$$w^{(0)}(x) \approx \sqrt[4]{\frac{m\omega_0}{\pi\hbar}} e^{-m\omega_0 x^2/(2\hbar)} \quad (3.13)$$

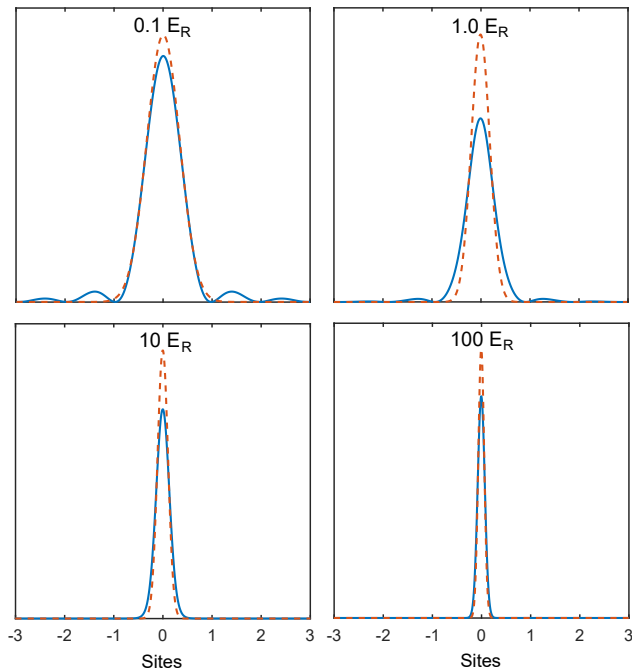


Figure 3.5: Square norms of the Wannier functions on a lattice site (solid blue lines) are plotted in arbitrary units for a selection of lattice depths. The corresponding ground state harmonic wavefunctions (dashed red lines) are plotted for comparison. At lower lattice depths, the Wannier functions feature off-site revivals that are not captured in the harmonic approximation.

for a trap frequency  $\omega_0 = \sqrt{2V_0 k^2/m}$ . At lower lattice depths, however, one notes significant revivals of the wavefunction away from the central peak, suggesting an enhanced probability to detect the atom on a neighboring lattice site (figure 3.5). The shape of wings of the wavefunction will play a key role in the description of atomic motion and interactions within the Hubbard model.

## 3.2 Many Atoms in an Optical Lattice

If the atomic interactions become comparable to the width of the ground band, they will also play a role in determining the configuration of atoms in the ground state. Following the approach originally suggested by Jaksch *et al.* [65, 66], this section will introduce the Bose-Hubbard model for interacting bosonic atoms in the lowest Bloch band of an optical lattice, and will subsequently explore the effect these interactions have on the ground state.

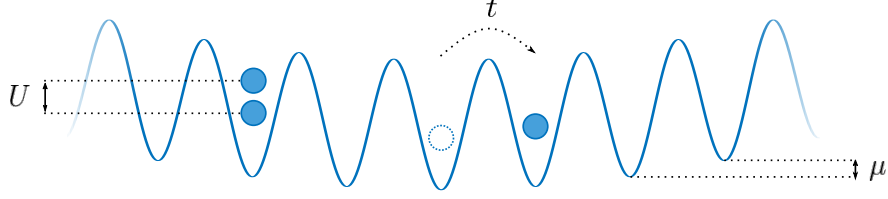


Figure 3.6: A schematic illustration of the matrix elements of the Hubbard model.

### 3.2.1 The Bose-Hubbard Model

The single-component Hubbard model describes particles which live on a lattice, may hop between sites, and interact only when they meet on a site, resulting in the Hamiltonian

$$H = \int d^3r \left[ \hat{\psi}^\dagger(\mathbf{x}) \left( -\frac{\hbar^2}{2m} + V_{\text{lat}}(\mathbf{x}) + V_{\text{trap}}(\mathbf{x}) \right) \hat{\psi}(\mathbf{x}) + \frac{g}{2} \hat{\psi}^\dagger(\mathbf{x}) \hat{\psi}^\dagger(\mathbf{x}) \hat{\psi}(\mathbf{x}) \hat{\psi}(\mathbf{x}) \right], \quad (3.14)$$

where  $g = 4\pi\hbar^2 a/m$  is the contact energy for atomic scattering length  $a$ . The field operators  $\hat{\psi}^\dagger(\mathbf{x})$  and  $\hat{\psi}(\mathbf{x})$  are responsible for the creation and annihilation of an atom at position  $\mathbf{x}$  and can be expanded in the Wannier basis as

$$\hat{\psi}(\mathbf{x}) = \sum_n \sum_i w^{(n)}(\mathbf{x} - \mathbf{x}_i) \hat{a}_i^{(n)}. \quad (3.15)$$

Assuming that the interaction energies and the kinetic energy of the system due to the temperature  $T$  are much less than energy gap between the ground and first excited band, the sum over  $n$  can be dropped as atoms exist only in the ground band. The Hubbard Hamiltonian then reduces to

$$H = - \sum_{\langle i,j \rangle} t_{ij} (\hat{a}_i^\dagger \hat{a}_j + h.c.) + \frac{1}{2} \sum_i U_i \hat{n}_i (\hat{n}_i - 1) + \sum_i \mu_i \hat{n}_i \quad (3.16)$$

with the number operator  $\hat{n} = \hat{a}_i^\dagger \hat{a}_i$  counting the atoms on site  $i$ .

#### Matrix elements of the Bose-Hubbard model

The coefficient of the kinetic energy term is

$$t = - \int dx w^*(\mathbf{x} - \mathbf{x}_i) \left( -\frac{\hbar}{2m} \nabla^2 + V_{\text{lat}}(\mathbf{x}) \right) w(\mathbf{x} - \mathbf{x}_j) \quad (3.17)$$

for a particle hopping from site  $i$  to site  $j$ . It has also been assumed that the off-site interactions are small compared to all the other energies in the system, so that the interaction energy only involves site  $i$  and is equal to

$$U = g \int d\mathbf{x} |w(\mathbf{x})|^4 . \quad (3.18)$$

This assumption is well-justified for all but the lowest lattice depths: by  $V = 2E_R$ , the contribution of nearest-neighbor sites to the interaction energy is already suppressed by  $10^2$  compared to the on-site interactions. Lastly, the term  $\mu$ , often called the *chemical potential*, characterizes the potential energy due to the external confinement and is equal to

$$\mu_i = \int d\mathbf{x} |w(\mathbf{x} - \mathbf{x}_i)|^2 V_{\text{trap}}(\mathbf{x} - \mathbf{x}_i) . \quad (3.19)$$

### Approximations to the matrix elements

To see how the matrix elements scale with lattice depth, it is useful to find their analytic approximations in the limit of high lattice depth. In the case of  $U$ , one may replace the Wannier functions with harmonic oscillator wavefunctions (3.13), leading to

$$U \approx \sqrt{\frac{8}{\pi}} ka \left( \frac{V_0}{E_R} \right)^{3/4} E_R . \quad (3.20)$$

The harmonic oscillator wavefunctions are further a little narrower than the Wannier functions (see figure 3.5), leading to a slight overestimate of the interaction energy. On the other hand, the tunneling matrix element  $t$  can, in the context of the tight-binding model, be inferred from the band structure calculation as  $t = \frac{1}{4}(E^{(\pm\hbar k)} - E^{(0)})$  and can therefore be approximated [67] as

$$t \approx \frac{4}{\sqrt{\pi}} e^{-2\sqrt{V_0/E_R}} \left( \frac{V_0}{E_R} \right)^{3/4} E_R . \quad (3.21)$$

These considerations show that  $U/t$  scales exponentially with the lattice depth, which means that an extremely wide range of Hubbard parameters are available within a reasonable range of lattice depths (figure 3.7).

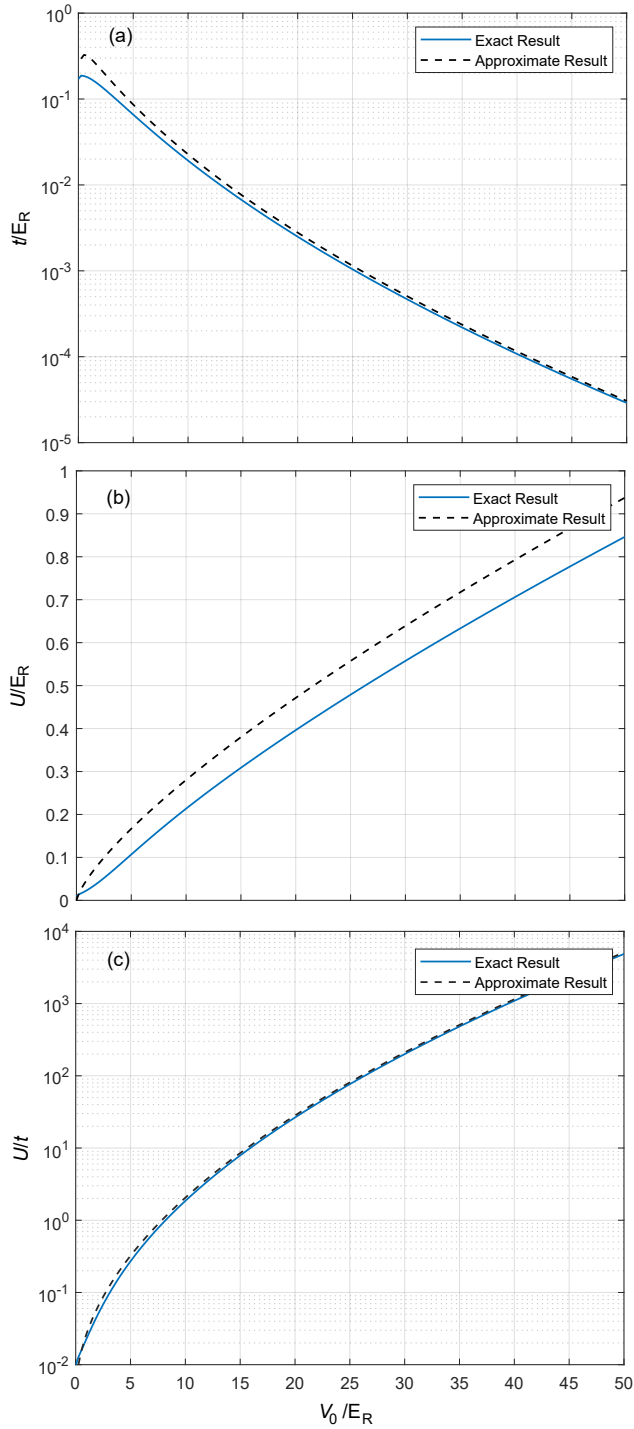


Figure 3.7: The matrix elements of the Hubbard model are plotted as a function of the lattice depth in recoils. In each case, the approximate analytical result is plotted (dashed black line) as a comparison to the exact numerical result calculated from the Wannier functions (solid blue line). The 1D tunneling energy  $t$  shown in (a) does not depend on the choice of atomic species and is a general result for a cubic lattice. In (b), the 3D on-site interaction energy scales linearly with the scattering length, which in the  $F=1$  manifold of  ${}^7\text{Li}$  can be tuned arbitrarily with Feshbach resonances. For the plot, a typical scattering length of  $100 a_0$  is chosen. The same scattering length is chosen in (c), which shows how  $U/(6t)$  can be tuned over many orders of magnitude simply by varying the lattice depth.

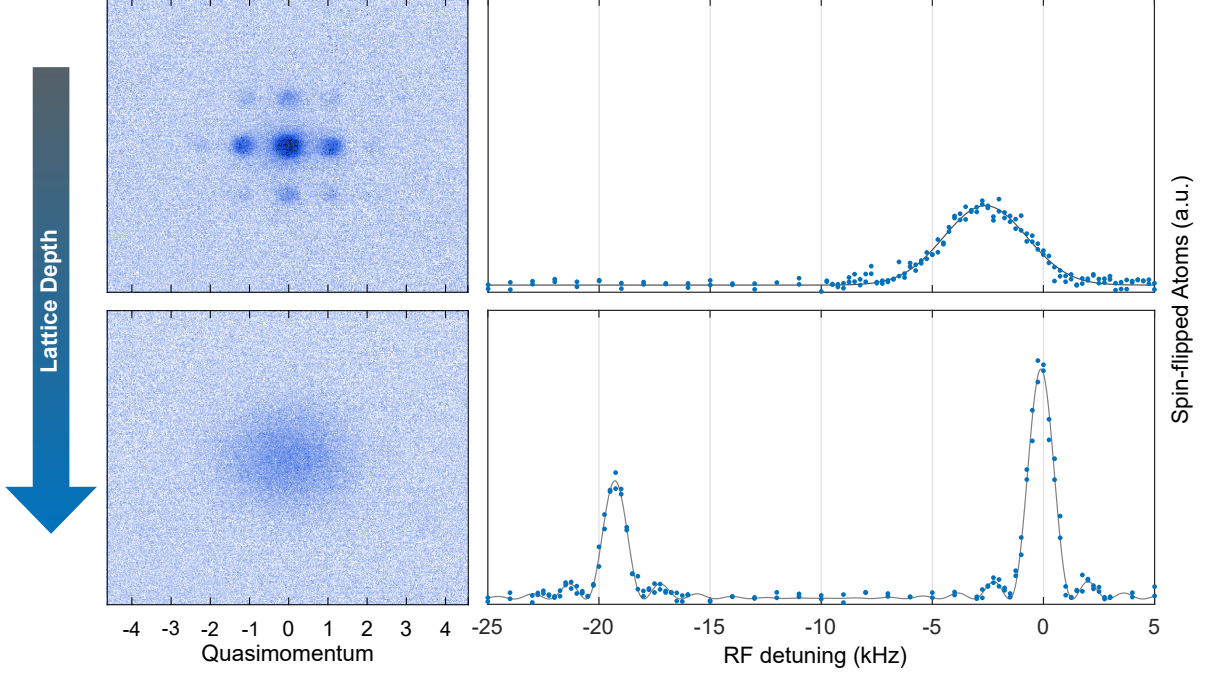


Figure 3.8: Comparisons of time-of-flight images (which probe quasimomentum) and lattice interaction spectroscopy (which probes site occupancy) reveal the differing nature of the ground states at low and high lattice depths (upper panels and lower panels). Images of the ballistically expanded cloud reveal characteristic superfluid peaks at  $\pm\hbar k$  momenta at low lattice depths, whereas at high lattice depths this coherence disappears. (The horizontal axis has units of  $\pm\hbar k/\sqrt{2}$  because the lattice is viewed at a  $45^\circ$  angle.) RF interaction spectroscopy reveals that the excitation spectrum of the MI contains a sharp peak at  $\delta = 0$  and  $-U/h$ . At low lattice depth, this structure subsides into a broadened peak centered around  $-U/\hbar \cdot \bar{n}$ , due to mean-field shifts.

### 3.2.2 Ground State of the Hubbard Model

In the Hubbard model, competition between  $t$ , which lowers the kinetic energy of the system by delocalizing the particles, and  $U$ , the potential energy arising from interactions, sets up an interplay between two phases with very different characteristics. When  $t/U \rightarrow \infty$ , the Hamiltonian describes a lattice superfluid, while when  $t/U \rightarrow 0$  the Hamiltonian describes a Mott Insulator (MI). In the former, site occupancy is described by a coherent state with number fluctuations and well-defined phase. The ideal superfluid state can, in the absence of external confinement, be written as

$$|\Psi_{\text{SF}}\rangle = \left( \frac{1}{\sqrt{M}} \sum_{i=1}^M \hat{a}_i^\dagger \right)^N |0\rangle \quad (3.22)$$

for  $M$  lattice sites containing  $N$  bosons, which approaches

$$|\Psi_{\text{SF}}\rangle = \prod_{i=1}^M \exp\left(\sqrt{\frac{N}{M}} \hat{a}_i^\dagger\right) |0\rangle_i \quad (3.23)$$

for sufficiently large  $N$  and  $M$ . In 3D at  $U/t = 0$ , all  $N$  bosons will be fully delocalized over the lattice, occupying the Bloch state  $\psi_0^{(0)}(x)$ . In contrast to the superfluid, the site occupancy of the Mott Insulator is rather described by a Fock state

$$|\Psi_{\text{MI}}\rangle = \prod_i |\bar{n}\rangle_i \quad (3.24)$$

with the average filling factor  $\bar{n} = N/M$ . The MI phase is an insulator (i.e. the atoms are localized to a single lattice site) *because* of the interactions, which penalize delocalization. It is possible to view the interaction portion of the Hamiltonian as a number-squeezing term which suppress number fluctuations on a lattice site.

These two different phases have important consequences for both the spectra of energy and of quasimomentum in the lattice system. The superfluid phase exists at a well-defined quasimomentum and is phase-coherent, which is readily observed by projecting the quasimomentum onto real momentum by ballistic expansion. In contrast, the MI exists at a well-defined occupation number, which splits the lowest Bloch band into many ‘‘Hubbard bands’’ and produces an energy spectrum that can be probed e.g. via lattice depth modulation (see section 3.3.1). The uncertainty relation between phase and number suggests that the characteristic momentum spectrum of the superfluid phase should be entirely washed out for the MI phase, and *vice versa* for the energy excitation spectrum.

### Quantum phase transition

The critical value of  $t/U$  that describes transition between the superfluid and the MI can be calculated in the context of the mean field approximation

$$\psi = \langle \hat{a}_i \rangle = \langle \hat{a}_i^\dagger \rangle = \sqrt{\bar{n}_i}, \text{ and} \quad (3.25)$$

$$\langle \hat{a}_i^\dagger \hat{a}_j \rangle = \langle \hat{a}_i^\dagger \rangle \hat{a}_j + \hat{a}_i^\dagger \langle \hat{a}_j \rangle - \langle \hat{a}_i^\dagger \rangle \langle \hat{a}_j \rangle = (\hat{a}_j + \hat{a}_i^\dagger) \psi - \psi^2. \quad (3.26)$$

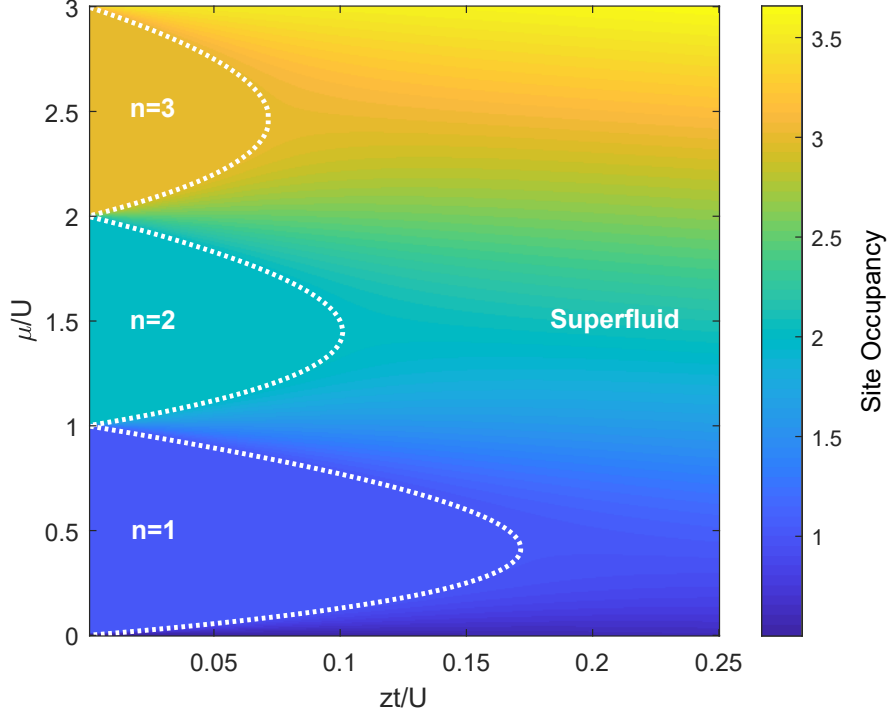


Figure 3.9: The expectation value of the site occupancy  $n$  obtained from a mean field approximation to the 3D Bose-Hubbard model is plotted vs the chemical potential  $\mu$  and tunneling  $t$  (both in units of the interaction energy  $U$ ), as calculated for  $n_{\max} = 7$ . The white dotted lines show the perturbative approximation to the phase boundary between the Mott insulator and superfluid. Within the Mott insulating lobes,  $n$  is an integer, while in the superfluid region  $n$  is a real number, which suggests one should expect the number fluctuations commensurate with a superfluid phase.

Substitution into (3.16) and scaling by the number of sites gives an effective Hamiltonian

$$\begin{aligned}
 H_{eff} &= -zt\psi \sum_i (\hat{a}_i + \hat{a}_i^\dagger) + zt\psi^2 N_s + \frac{U}{2} \sum_i \hat{n}_i(\hat{n}_i - 1) - \mu \sum_i \hat{n}_i \\
 &= \frac{U}{2} \hat{n}_i(\hat{n}_i - 1) - \mu \hat{n}_i - (\hat{a}_i + \hat{a}_i^\dagger)\psi + \psi^2
 \end{aligned} \tag{3.27}$$

where  $U$  and  $\mu$  have both been rescaled by  $zt$ , the product of the tunneling coefficient  $t$  and the coordination number  $z$  of the lattice. An advantage of this mean field Hamiltonian is that it is completely local, depending only on the occupancy of each site  $i$ , and can thus be diagonalized in order to determine the energy spectrum and wavefunctions.

As a first step, one can gain some intuition into the phase diagram by treating the tunneling as

a perturbation. Following Oosten *et al.* [68], the ground state energy for  $g$  particles is then

$$E_g^{(0)} = \frac{U}{2}g(g-1) - \mu g, \quad (3.28)$$

for  $U(g-1) < \mu < Ug$ . The first order of perturbation theory produces no non-zero matrix elements. To second order,

$$\begin{aligned} E_{GS}^{(2)} &= \psi^2 \sum_{n \neq g} \frac{|\langle g|V|n \rangle|^2}{E_g^{(0)} - E_n^{(0)}} \\ &= \frac{g}{U(g-1) - \mu} + \frac{g+1}{\mu - Ug} \end{aligned} \quad (3.29)$$

The mean field ground state energy is thus the sum

$$E_g(\psi) = E_0(g, U, \mu) + E_2(g, U, \mu)\psi^2 + \dots \quad (3.30)$$

minimized as a function of  $\psi$ . When  $a_2(g, U, \mu) > 0$ ,  $\psi = 0$ , while when  $a_2(g, U, \mu) < 0$ ,  $\psi \neq 0$ . Thus the boundary between phases is at  $a_2(g, U, \mu) = 0$ . Rescaling  $zt$  and  $\mu$  by  $U$  and solving for  $\mu$  gives

$$\mu_{\pm}^{(c)} = \frac{1}{2}[(2g-1) - t] \pm \frac{1}{2}\sqrt{1 - 2t(2g+1) + t^2} \quad (3.31)$$

which outlines the Mott lobes for each  $g$ , which are plotted in figure 3.9.

Returning to the local effective Hamiltonian, one may calculate the density per site by direct diagonalization, after truncating the Hamiltonian at  $n_{\max}$  sufficiently higher than the highest site occupancy expected in the system. The eigenvectors give the amplitude of the Fock states  $|0\dots n\rangle$  on each site. This method thus provides the expectation value of the number operator *within* the Mott insulating lobes, where it is integer-valued, and also in the superfluid regions without, where it is not (see figure 3.9).

One may use this phase diagram in order to quantitatively predict the ground state of bosons in an optical lattice. In general the ground state depends not only on the lattice depth  $V_0$ , but also on the external confinement  $V(\mathbf{r})$ . Making the local density approximation, one may consider the chemical potential on each site to be  $\mu - V(\mathbf{r})$ . Along a single dimension, a 3D optical lattice with harmonic confinement samples a line along the phase diagram, from  $\mu = 0$  to  $\mu = \mu_{\max}$ . If the

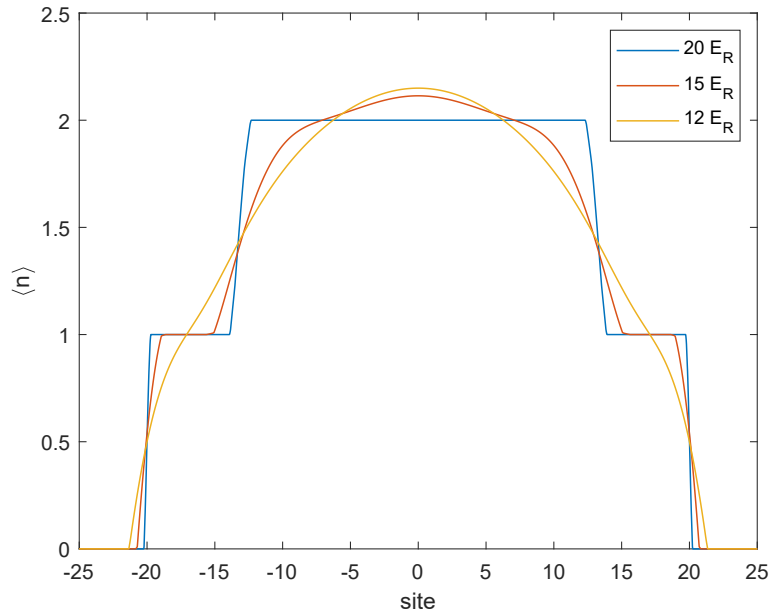


Figure 3.10: A cut of the expectation values of the number operator  $n$  along a lattice axis are plotted for lattices of various depths. The number of atoms is 40,000, the lattice beam waists are 100 microns and the scattering length is  $100a_0$ . The site occupancy develops a kink as each plateau crosses the Mott insulating transition.

lattice depth is uniform, this line is vertical, although in the case that the confinement arises from the curvature of the lattice beams themselves, the depth of the lattice is greatest where  $V(x) = 0$  and so tunneling increases as  $\mu - V(x)$  decreases. Thus at sufficiently high filling, the ground state of interacting bosons in an optical lattice is said to have a “wedding cake” structure, with a plateau of sites occupied by  $n$  atoms in the center, surrounded by a plateau of occupancy  $n - 1$ , and so on until  $n = 0$ , with thin shells of superfluid in between. These superfluid shells are regions where tunneling is not suppressed by interactions, and have expectation values of the number operator between  $n$  and  $n - 1$  (see figure 3.10).

### Super-exchange

The ground state of the MI at infinite lattice depth (infinite  $U/t$ ) is a product state of integer site occupancy, as in equation (3.24). At finite but small  $U/t$ , one may again treat tunneling as a

perturbation on top of the MI ground state at infinite lattice depth, to find that

$$|\Psi\rangle^{(1)} \approx |\Psi_{\text{MI}}\rangle + \frac{t}{U} \sum_{\langle i,j \rangle} \hat{a}_i^\dagger \hat{a}_j |\Psi_{\text{MI}}\rangle \quad (3.32)$$

to lowest order in  $t/U$ , which suggests that the ground state fundamentally contains a fraction of particle-hole excitations proportional to  $(t/U)^2$ . These *coherently* admixed doublons are responsible for restoring finite visibility of superfluid peaks above the MI transition [69] and have been directly observed in quantum gas microscope experiments [70], and will be important considerations for the lifetime of an  $n=2$  MI, where the particle-hole excitations create triplons that are subject to three-body loss (section 4.3.3). Their presence, however, already suggests it is worth considering *second-order* tunneling process which involves an atom tunneling to a virtual excited state (which does not conserve energy) and tunneling back: in analogy to the way an off-resonant two-photon process with one-photon Rabi frequency  $\omega$  and detuning  $\Delta$  occurs at a rate  $\Omega^2/\Delta$ , tunneling admixes particle-hole pairs at a rate  $J \equiv t^2/U$ . The off-site interaction energy arising from this second-order tunneling process is about an order of magnitude larger than the “real,” zeroth-order off-site interaction energy computed directly from the overlap of the Wannier functions (3.18), and results in oscillations in the population of a double-well system with two particles [23].

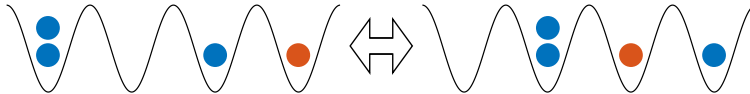


Figure 3.11: Schematic illustrating two different sorts of super-exchange processes. Two particles which could not tunnel separately, due to conservation of the interaction energy, are allowed to tunnel as a pair. Two neighboring particles (red and blue) can also switch places, which does not modify the overall-density distribution but nonetheless shifts the energy of the state by the exchange coupling energy  $J_{ex}$ . In contrast to bound-pair tunneling, this latter process is only non-trivial in systems with at least two distinguishable components.

The presence of super-exchange interactions in a MI gives rise to all sorts of fascinating phenomena, such as repulsively bound pairs of atoms [71] and distillation of vacancies [72]. One especially relevant feature it brings to the current work is the idea of partitioning the Hilbert space of the lattice system into a density (or “charge”) sector, which is frozen, and a spin sector in which all the dynamics take place. Because the Mott insulator (under appropriate filling conditions) has an integer number of particles per site, it is an ideal platform upon which to implement a quantum

simulation of a lattice model in which the quantum information is carried by internal states of atoms: the density distribution remains in quasi-equilibrium, but “spin” information can be exchanged between sites via super-exchange. The resulting interaction energy breaks the degeneracy of the different pseudospin configurations in the lowest of the Hubbard bands (which themselves exist in the ground state of the lowest Bloch band), giving rise to a spinful ground state that will be shown in section 4.1.1 to have features reminiscent of magnetic ordering in the Heisenberg model.

### 3.3 Lifetimes and Coherences

A variety of heating mechanisms can limit the fidelity of the single-component ground state. Indeed, any non-adiabatic variation of the parameters of the Hamiltonian will lead to excitations of some kind—imperfections in the adiabaticity of the lattice ramp will limit the initial fidelity, and technical sources of noise in the control beams and fields will limit the coherence lifetime of the model. The ground state of atoms in an optical lattice is protected by an energy gap to the first excited state at all depths in 1D and at all depths above  $2.3 E_R$  in 3D. While care is taken to ramp adiabatically with respect both to this bandgap and to the over-all confinement, dynamic processes in the lattice can nevertheless lead to a decay of the ground state occupation. This section will provide an overview of the decoherence mechanisms present in an optical lattice experiment, and provide some insight on how to diagnose various sources of heating— a process which is not always straightforward. While the effects of intensity and pointing noise on inter-band excitations have been carefully characterized in fermionic Lithium [73], the effects of position noise of the lattice sites will also turn out to be an important consideration. Further, there are intra-band excitations possible in bosons which are not in fermions (due to the Pauli exclusion principle), although the heating rates for these excitations turn out to be rather low.

#### 3.3.1 Inter-band Heating Mechanisms

Transitions from the ground band to excited bands of the optical lattice can be driven by fluctuations in the lattice potential at frequencies on the order of the bandgap  $w_{bg}$ . If the occupation is mostly in the ground band, these transitions are mostly single-particle physics, and are relatively simple to evaluate in the limit of harmonic oscillator lattice sites (i.e. deep lattices) where most lattice

physics takes place.

### Intensity fluctuations

By considering the fractional fluctuations of the trapping frequency  $\omega_T$  as a perturbation, Gehm *et al.* [74] showed that the expected rate of transitions out of the ground band of a harmonic oscillator is

$$\Gamma_{0 \rightarrow 2} = \frac{\pi \omega_T^2}{8} S_k(2\omega_T) \quad (3.33)$$

where  $S_k(\omega)$  is the one-sided power spectrum of the perturbation  $\epsilon(t) = \delta\omega_T/\omega_T$  in units of  $(1/s)^{-1}$ , normalized so that  $\int_0^\infty d\omega S_k(\omega) = \epsilon_{\text{RMS}}^2$ . The rate of excitation into the *first* excited band is identically zero: the perturbation is of the form  $\epsilon^2 x^2$ , which is even and therefore connects only states with the same parity. It is interesting to note that such parametric heating is only sensitive to noise at the frequency corresponding to  $E_{g \rightarrow e}/\hbar$  (which in the harmonic oscillator approximation is simply the trap frequency times the difference in band indices). The excitation rate as a function of the lattice depth is thus sensitive to the shape of the noise. For example, if the noise is white— i.e. it has a power spectral density<sup>1</sup> (PSD) that is constant as a function of frequency— the excitation rate will increase as  $\omega_T^2 \propto V_0$ . If, however, the PSD falls off as  $1/\omega^2$ , the excitation rate will be a constant function of the lattice depth.

It is therefore important to characterize the PSDs of the various sources of intensity noise in a lattice. White noise is the signature of a Poissonian process, or of many uncorrelated noise sources (as a consequence of the central limit theorem), and in electronics is often the result of Johnson-Nyquist noise in resistors— which is especially likely to manifest in analog circuits as noise on the input offset of the input amplifier of a circuit (or wherever the signal is smallest). Alternatively, a white noise profile might be the result of shot noise in the measurement of an optical signal. It could also be present in the light itself as a result of stimulated Brillouin scattering (SBS), which is essentially white noise at frequencies lower than 1 GHz. Brownian noise ( $S \propto 1/\omega^2$ ), on the other hand, is the result of a random walk, and is the likely noise profile of vibrations (neglecting resonances), which can couple into optical intensity via pointing noise at fiber-coupling inputs or

---

<sup>1</sup>The power spectral density used here is *not* the spectral density of the *optical* power, but rather the square modulus of the Fourier transform of the lattice depth  $V(t)$ — which itself is proportional to the optical power in the lattice beam.

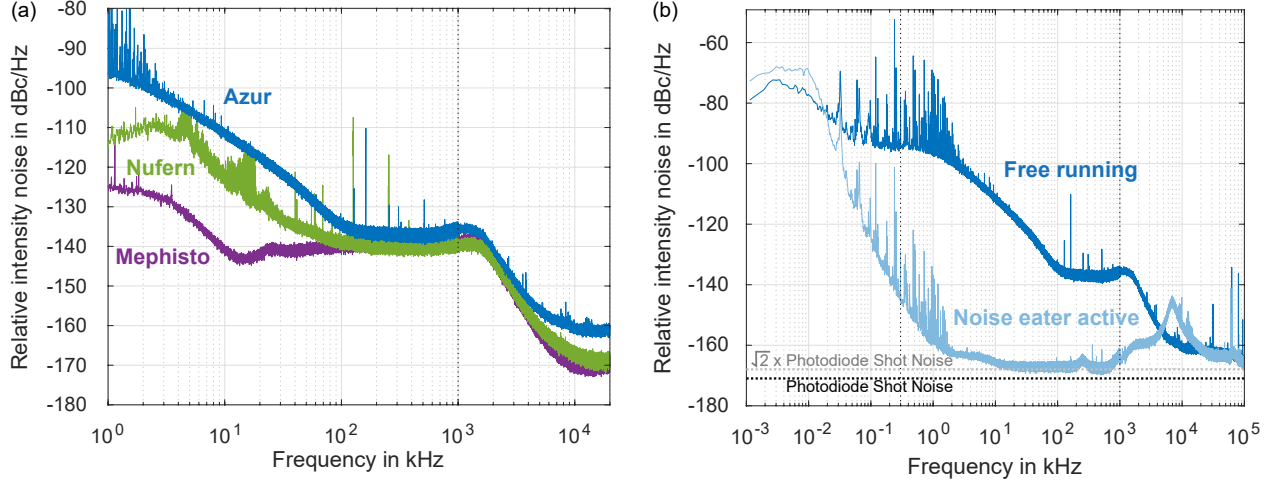


Figure 3.12: (a) Relative intensity noise at full output power of two models of 50 W 1064 nm fiber amplifier (Azur Light Systems and Nufern), seeded by the same ND:YAG laser (Coherent Mephisto). (b) Relative intensity noise of the Azur fiber amplifier with and without an EOM-based noise-canceling scheme, after passing through a single-mode fiber. One photodiode is used for feedback, and a second independent photodiode is used for the measurement, so that the *measured* noise floor is the sum of two uncorrelated white noise processes.

via polarization fluctuations in fibers. It is also the expected intensity noise profile of a laser, absent excess electronic noise in the control circuitry, due to the lowpass filtering effect of the gain cavity.

Significant effort has been made to characterize– and to some extent mitigate– intensity noise in the lattice lasers. Two different 50 W, 1064 nm fiber amplifiers have been used to generate lattice light. The first is a customized Nufern NuAmp with optimized gain fiber and shortened output fiber (in order to reduce stimulated Brillouin scattering, which is a limiting source of noise in the factory models), and the second is a stock model Azur Light Systems amplifier. The relative intensity noise (RIN) of both are plotted in figure 3.12a, along with the RIN of the Coherent Mephisto seed, where the RIN in dBc/Hz is defined as  $10 \log_{10} S(f)$ , if  $S(f)$  is the PSD of the fractional noise in 1/Hz, i.e.

$$S(f) = 2\pi \left| \frac{1}{T} \int_0^T \frac{V(t) - \bar{V}}{\bar{V}} e^{i\omega t} dt \right|^2 \quad (3.34)$$

for a photodiode signal  $V(t)$ . For both fiber amplifiers, two regimes are apparent: at frequencies below 100 kHz, noise produced by the fiber amplifiers themselves dominates (from a combination of power supply noise and vibrations), while above 100kHz the limit is the RIN of the seed laser. The plateau of noise between 100 kHz and 1 MHz is likely due to the shot noise of the internal photodiode which the Mephisto laser uses to regulate its own output power (most units contain

a “noise eater” which suppresses endemic intensity oscillations at a few hundred kilohertz), after which the noise power falls off with a slope of -30 dB/Hz.

This performance can be readily exceeded by the use of an additional noise-canceling scheme. Figure 3.12b shows the results of such a scheme, which uses an EOM between crossed polarizers as an intensity modulator to achieve shot noise limited performance in the region of the bandgap frequencies, from 1 kHz to 1MHz. The remaining noise at low frequencies comes from a combination of amplifier noise and pointing noise (turned into intensity noise by fiber-coupling). Addressing this low frequency noise directly with the EOM scheme is difficult because the amplitude of fluctuations grows larger as  $1/f$ , which subsequently requires servoing very high EOM control voltages ( $> |\pm 15|$  V), which are incompatible with high bandwidth, and/or operating the EOM polarization rotator at a setpoint of  $45^\circ$  to increase the sensitivity to the control voltage, which sacrifices optical power. A better approach is to use an AOM to take care of low frequency noise (which is well within the bandwidth of typical AOM feedback systems). Intensity noise is not currently a limiting source of heating (see next section), but such additional noise-canceling schemes will likely play an important role in future upgrades.

### **Characterizing sensitivity to intensity noise**

A model-free way to measure the local slope of the sensitivity to noise is to *add* noise and measure the response of the system. It is usually easier to add noise than it is to take it away, so that if there are many uncorrelated heating processes, this method can help to demonstrate that a certain heating process is not limiting (or at least is not the only limit) before making a serious technological investment in noise-canceling. In order to test the atoms’ sensitivity to intensity noise in the lattice beams, it is straightforward to introduce broadband white noise into a lattice beam and measure the resulting coherence time as a function of the amplitude of the noise. The results (figure 3.13) indicate that the coherence lifetime of the 3D Mott Insulating phase was limited by a heating mechanism other than intensity noise at the time of the measurement.

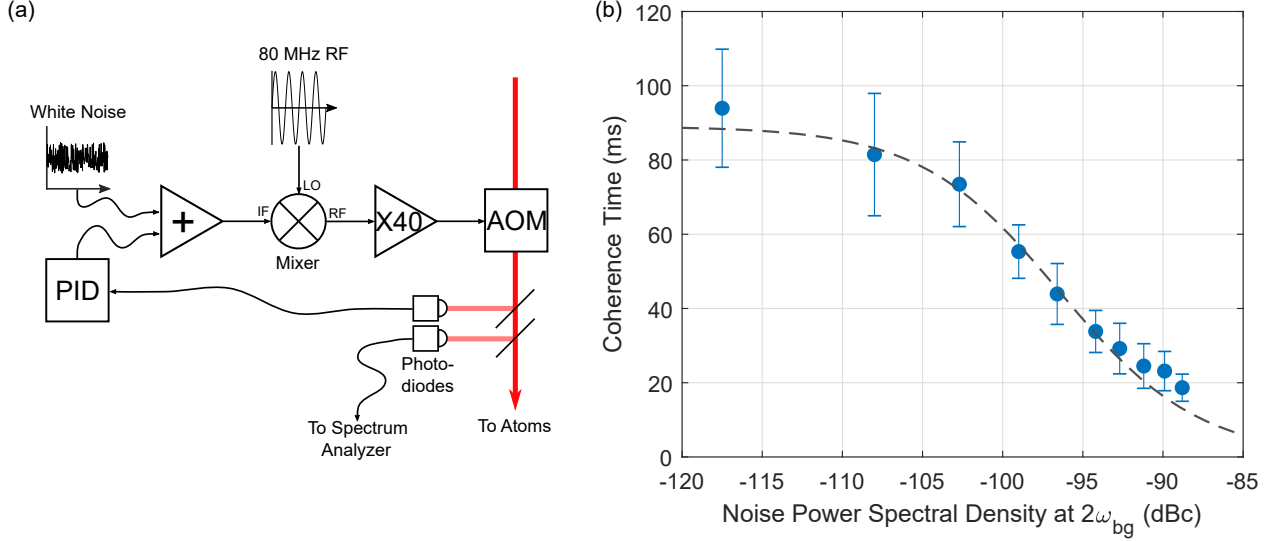


Figure 3.13: (a) Diagram of the scheme to measure the effect of added intensity noise. White noise (0-1 MHz) is summed with the output of one of the lattice feedback controllers. The summed signal controls the amplitude of the RF powering the AOM, which controls the intensity of the light. Two separate photodiodes supply the feedback signal and a monitor signal, which can be used to measure the magnitude of the added noise. Parametric heating is driven by noise at frequencies of approximately twice the bandgap  $\omega_{bg}$ , which is too high in  ${}^7\text{Li}$  for the added noise to be attenuated by the feedback controllers. (b) Coherence lifetime of a Mott Insulator at  $35 E_R$  as a function of intensity noise in one of the three lattice arms, measured by adiabatically ramping back to the BEC and probing the condensate fraction. The dashed line is a fit to a model in which the loss rate depends linearly on the PSD of the intensity noise, as in (3.33), and another independent loss rate.

## Position fluctuations

Fluctuations in the position of a harmonic trapping potential can be evaluated in a similar way to the intensity fluctuations discussed in the previous section, leading to an excitation rate of

$$\Gamma_{0 \rightarrow 1} = \frac{\pi}{\hbar} m \omega_T^3 S_x(\omega_T) \quad (3.35)$$

where  $S_x(\omega)$  is the PSD of the trap position fluctuations in  $\text{m}^2(\text{s})^{-1}$ . In this case, the perturbation  $\epsilon_x$  is odd and connects only states with opposite parity, leading to transitions from the zeroth to the first excited band. For position noise, the scaling of the excitation rate is one power of  $\omega$  stronger than for intensity noise, so that even if the noise is Brownian (which one would expect it to be for unattenuated vibrations, for example), excitation rates should still increase as a function of trap frequency.

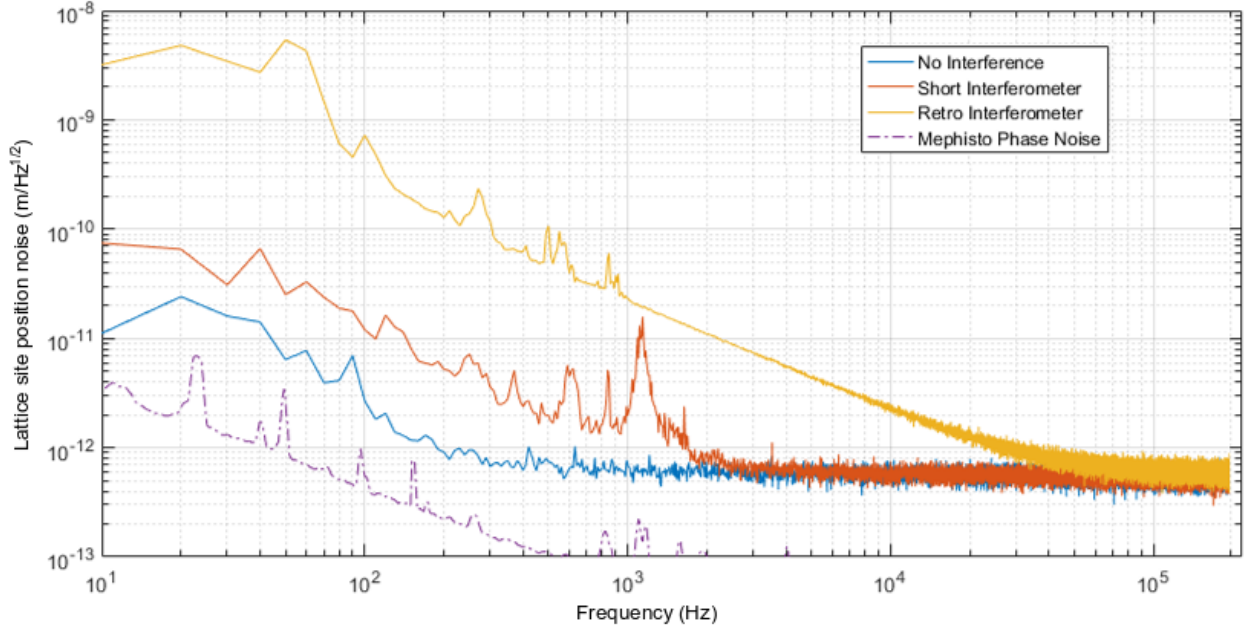


Figure 3.14: Interferometrically measured position noise of a lattice site. The noise floor is determined by twice the noise in the signal if one of the arms of the interferometer is blocked (blue line). The stability of the reference arm is characterized by using two very short interferometers, rather than one short and one long (red line). The resulting position variation in a lattice site (yellow line) is calculated from the photodiode signal  $V$  as  $\Delta z = (V/V_{\max} - 1/2)/(\sqrt{2}k)$ . The contribution of the frequency fluctuations of the laser (dash-dot purple line) are calculated from the manufacturer-specified phase noise of the Innolight Mephisto laser used for the experiment. The ultimate noise floor of the measurement, around  $5 \times 10^{-13} \text{ m}/\sqrt{\text{Hz}}$ , comes from the shot noise of the light.

There are fundamentally two different sorts of noise which can cause the position of a lattice site to fluctuate: noise in the position of the retro-reflection mirror, and noise in the frequency of the lattice light. The retro-reflecting surface defines a node of the standing wave and the number of nodes between this surface and a point  $l$  away is fixed by the wavelength to  $2l/\lambda$ . Thus fluctuations in the longitudinal position of the retro mirror directly couple to fluctuations in the positions of the lattice sites. However, a change in the frequency of the lattice light  $\omega_L$  by  $\delta$  moves a lattice site by approximately  $l \frac{\delta}{\omega_L}$ . For typical  $\omega_L$  of 100 THz and lattice path lengths of 1 m, a frequency sweep of  $\delta = 100 \text{ MHz}$  moves a lattice site by  $1 \mu\text{m}$ . The effect of frequency noise can therefore be decreased by shortening the “lever arm” of the retro-reflection path length.

Position fluctuations can be evaluated with the aid of a Michelson-Morely interferometer. A non-polarizing beamsplitter cube is introduced into the lattice path near the launch point. Half of the light travels through the chamber and is retro-reflected as usual (path length  $\sim 1$ ); the other

half is retro-reflected immediately (path length  $\sim 1$  mm). The two beams recombine at the cube and the resulting intensity is measured by a photodiode. The phase of the interference signal is a measure of the arm length difference, modulo  $\lambda/2$ . Assuming the short arm is a good reference, this path length difference is a measure of the fluctuations in the position of a lattice site. It can be further assumed that relative motions of the beamsplitter cube and retro-reflection mirror are comparable but uncorrelated, so that the position fluctuations of a lattice site in the inertial frame of an atom are  $1/\sqrt{2}$  smaller than what is measured by the interferometer. In order to make a careful measurement, the interferometer must be locked to one of the interference fringes at half the contrast, so that the response of the interference signal is locally a linear function of the path length difference. Because of the path length difference of 1 m between the reference and the lattice arm, this can be accomplished by feeding back on the frequency of the laser with a slow servo (bandwidth  $< 1$  Hz). The noise floor of this measurement is determined by the intensity noise in the light, which produces fluctuations of the interference signal which are uncorrelated with path length difference, so it is important to use a light source with low intensity noise.

The results of this measurement can be seen in in figure 3.14. Although photon shot noise prevented a precise determination of the spectral power density of the position noise between 100 kHz and 500 kHz, which are the relevant trap frequencies for  $^7\text{Li}$ , it can be determined that the PSD decreases as  $1/\omega^2$ , ignoring low frequency acoustic resonances, which are unlikely to occur above 10kHz. This scaling comes as no surprise, as absent any unusual driving or resonances, the position of some object ought indeed to be the result of Brownian motion. Extrapolating to higher frequencies, a lattice of  $16 E_R$  has an on-site trap frequency of  $\omega_T = 2\pi \times 200$  kHz and should suffer from position-noise-driven transitions to the first excited band at a rate of about  $1 \text{ s}^{-1}$  in one dimension. Since these data were taken, compressed air vibration isolation has been added to the legs of the table which supports the apparatus. This isolation system is expected to reduce the vibration noise power at frequencies above 100 Hz by at least 20 dB. While repeating the interferometric measurement of the lattice position noise would be a direct confirmation that the system works as intended, the subsequently measured excitation rate of the atomic sample (see figure 3.15) is consistent with these expectations, and Mott insulator coherence lifetimes (as measured by adiabatic return to the superfluid phase) increased by a little more than a factor of 10.

## Fluctuations in the external trapping potential

Any noise present in external potentials (the ODT, or external confinement of the transverse lattice beams) can also couple to the position and depth of the optical lattice sites. Treating all potentials as harmonic, for fractional perturbations in the external trap frequency  $\epsilon_{\text{ext}}$ , the total trap frequency can be written as

$$\omega_{\text{tot}}^2 = \omega_{\text{site}}^2 + \omega_{\text{ext}}^2 (1 + \epsilon_{\text{ext}})^2 . \quad (3.36)$$

Similarly, perturbations in the external trap position lead to a fluctuating position of the trap minimum satisfying

$$\frac{\partial}{\partial x} (\omega_{\text{site}}^2 x^2 + \omega_{\text{ext}}^2 (x - \epsilon_{\text{ext}})^2) = 0 . \quad (3.37)$$

In both cases, it turns out that the effect of the external perturbations are reduced by a factor  $(\omega_{\text{ext}}/\omega_{\text{site}})^2 < 10^{-3}$  for a wide range of lattice parameters, including those used in this experiment. The small size of this coefficient means that intensity or pointing noise in externally confining beams are unlikely to contribute to excitation rates in a lattice.

## Choice of atomic species

The physics of the Hubbard model is controlled by the dimensionless ratio  $t/U$ . In section 3.2.1 it was shown that this quantity scales as  $e^{-2\sqrt{V_0/E_R}}$ , which means that, ignoring for the present any variation in the s-wave scattering length among different atomic species, access to the same parts of the Bose-Hubbard phase diagram is possible with atoms of any mass at the same lattice depth  $V_0$ , measured in units of  $E_R$ . At the same time, the on-site trap frequency of an optical lattice is  $\omega_{\text{site}} = \sqrt{2V_0}\hbar k^2/m$ , which means that that  $\omega_{\text{site}} \sim 1/m$  for a given  $V_0$ , depending on the choice of atom. The inter-band excitation rate at a given lattice depth due to *either* intensity noise or position noise therefore scales as  $1/m^2 \cdot S(\omega)$ , which leads to higher heating rates for lighter atoms if  $S(\omega) \propto \text{const}$  and no advantage if  $S(\omega) \propto 1/\omega^2$ .

On the other hand, if one wishes to observe super-exchange physics, the relevant comparison is the super-exchange time  $\tau_{\text{SE}} = 1/\hbar \cdot t^2/U \propto (t/U)^2 \cdot U \propto \text{const} \cdot 1/m$ . As already discussed, the coherence time  $\tau_{\text{C}} \propto m^2/S(\omega)$ , so that  $\tau_{\text{SE}}/\tau_{\text{C}} \propto m/S(\omega)$ . It is therefore critically important to understand the functional form of  $S(\omega)$ , as lighter atoms may either be advantaged or disadvantaged

with respect to single-particle band excitations, when it comes to observing super-exchange physics!

### 3.3.2 Intra-band Heating Mechanisms

Excitations within the first Bloch band may either be created directly by perturbations of the Hamiltonian, or via inter-band excitations which then relax to the lowest band via collisions. The former process creates particle-hole pairs whose energy scales with  $U$ , while the latter eventually sees the bandgap energy  $\hbar\omega_{\text{bg}}$  distributed over many doublons in the ground band.

#### Intensity fluctuations

Just as inter-band excitations can be caused by various sorts of noise at the frequencies of the bandgaps, intra-band excitations can be caused by perturbations of the Hamiltonian at frequencies within the bandwidth. The elementary excitation is the particle-hole pair, the creation of which has been studied by Pichler *et al.* [75], who find that, as  $t/U \rightarrow 0$  deep in an optical lattice, white noise on the lattice depth drives creation of particle-hole pairs as

$$\Gamma_{\text{PH}} = \frac{1}{\hbar^2} S_0 V_0 t^2 z (\langle n \rangle + 1) \quad (3.38)$$

for a PSD  $S_0$  of the fractional noise in the unitless lattice depth  $V_0$ . The particle-hole pairs are created with opposite quasimomenta and travel on top of the Mott insulator, but in sufficiently deep lattices have energy  $U$  regardless of quasimomentum, due to the flatness of the band. This rate scales with  $E_{\text{R}}^2 \propto 1/m^2$  for white noise, but is vanishingly small for  ${}^7\text{Li}$  in a  $15 E_{\text{R}}$  lattice—less than 10 mHz for  ${}^7\text{Li}$  in a  $15 E_{\text{R}}$  lattice created by beams with intensity noise at the level of 100 dBc/Hz.

#### Thermalization of band excitations

The band excitations discussed up to this point have been treated as single-particle phenomena, adding an entropy per particle of  $k_{\text{B}}/n \cdot \ln n$  to the Mott-insulating ground state by creating randomly located holes. If the first or second excited band atoms can collide with ground-band atoms, however, it is possible for each band excitation to further cause multiple intra-band excitations within the ground band. Müller *et al.* found that atoms in the  $|n_x, n_y, n_z\rangle = |1, 0, 0\rangle$  state relax

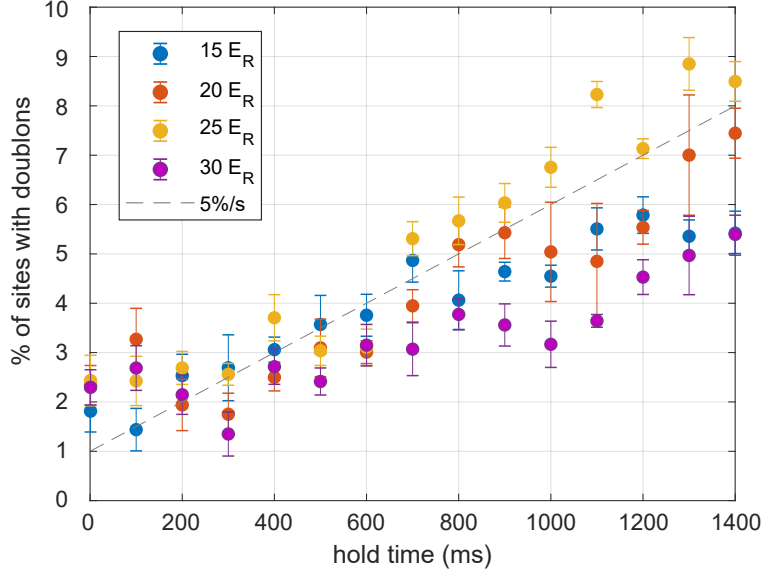


Figure 3.15: Doubly occupied lattice sites recorded as a function of time in 3D lattices of various depths, starting with 30,000 singly-occupied sites (the maximum number of doubly occupied sites would be 50%). The dashed line is a fit to the data for  $20 E_R$  for  $t > 200$  ms. The initial fraction of doublons is due to loss of sensitivity of the measurement technique at very low atom number, and does not change when the total atom number is varied within a range of  $\pm 30\%$ .

to the ground band via collisions at a rate which is nearly constant in the range of lattice depths between  $15 E_R$  and  $45 E_R$ , when the excited state population starts at 80% [76]. Starting with a lattice entirely in the  $|000\rangle$  state, it is possible to directly monitor the number of doubly-occupied sites as a function of hold time in the lattice (using RF transitions and interaction blockades to distinguish between sites with differing occupancies, as in section 4.2.1, rather than the band-mapping technique used by Müller *et al.*). This rate will serve as an ultimate limit on the lifetime of the many-body ground state in the optical lattice, and so is of great relevance for adiabatic state preparation. It is found that the rate of doublon creation is about 5% of the originally occupied sites per second, and does not depend on lattice depth (see figure 3.15). These data rule out direct creation of such excitations within the lowest Bloch band, which should occur at a rate that scales as  $V_0 \exp[-4\sqrt{V_0}]$ , but are consistent with a mechanism that involves inter-band excitations driven by position noise of the lattice sites followed by relaxation. It is possible that further steps to provide vibration isolation for the retro-mirrors in the lattice setup will improve the lifetime of the  $n=1$  MI beyond several seconds.

## 3.4 Implementation

Both the ODT and lattice light are supplied by a 1064 nm laser, whose detuning from the S to P transition in  ${}^7\text{Li}$  is nearly 340 THz, leading to a scattering rate which is below 10 mHz for a 3D, 35  $E_R$  lattice. The next sections discuss how this light is generated and controlled in order to create an optical lattice.

### Beam generation and delivery

The 1064 nm optical trapping and lattice light is provided by an Azur Light Systems 50 W fiber amplifier, seeded by a Coherent Mephisto ND:YAG laser with a linewidth specified at 1 kHz (for its contribution to the position noise of the lattice sites, see figure 3.14). The light is divided by a dynamically variable beamsplitter into a beam path supplying the ODT light and a beam path supplying the lattice light. During initial transfer of the cold atomic cloud into the ODT, the beamsplitter is set to maximize the amount of light reaching the ODTs, while during lattice operation, the opposite is the case. This setup is pictured in figure 3.16, and is capable of delivering either 11 W of power to each ODT beam or 8 W of power to each lattice beam. The crossover between the two regimes of operation takes place during the ODT evaporation step, when the power in the ODT is decreased to near-zero. Each of the two ODT beams and three lattice beams is coupled through an AOM (Gooch and Housego AODF 4090-6) to provide intensity control and frequency offsets, and then through a polarization-maintaining photonic crystal fiber (NKT Photonics LMA-PM-15). The large mode area of the fiber is important in order to minimize the potential for stimulated Brillouin scattering (SBS).

The fibers are connectorized with a PCF-SMA connector by AlphaNov. The connectors include an epoxy-free mode-stripper to prevent uncoupled light from propagating into the fiber cladding, in order to improve power handling. It was found that mode-strippers which contain epoxy tend to fail when the power of the uncoupled light reaches 6 W. As the in-coupled power of each lattice beam is about 10 W, this failure mode necessitates the use of an interlock mechanism which monitors the coupling efficiency of each fiber and switches off the laser beam when the coupling drops below 50%. The epoxy-free mode-strippers display no such failure mechanisms, and making an interlock is unnecessary. In addition, each mode stripper has been supplied with a homemade water-cooling

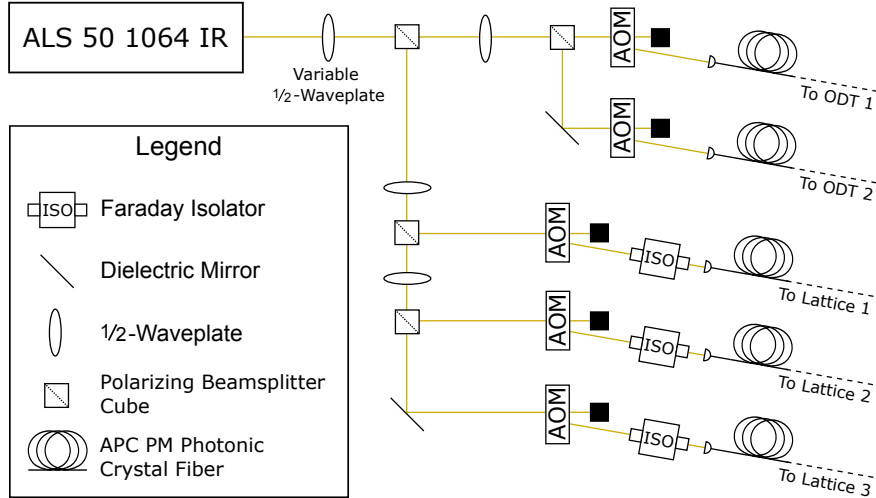


Figure 3.16: Schematic of the IR path. Not pictured are beam-shaping telescopes, focusing lenses, folding mirrors and polarization clean-up optics.

jacket, which makes the coupling efficiency virtually independent of the input power.

As each of the lattice beams is retro-reflected after passing through the chamber in order to create a standing wave potential, it is extremely important to provide adequate directional isolation along the lattice beam paths, both to protect the lasers from the retro-reflected power and the atoms from tertiary back-reflections. This goal is accomplished in two stages: a Faraday isolator with 55 dB of directional isolation is placed between each AOM and lattice fiber input, and a PBS and quarter-wave plate pair are placed after each lattice fiber output. The latter technique provides only about 40 dB of directional isolation, but mostly serves to protect the lattice beams from reflections of the retro-reflected beam from the fiber tip. These tertiary reflections are further minimized by the use of an angle-cleaved fiber. The cube-and-waveplate isolation technique also has the dual advantage that it does not suffer from the sort of thermal lensing typical of the TGG crystal inside a Faraday isolator, and can be easily un-done by the addition of a half-wave plate to the lattice beam path, allowing for easily alignment of the retro-reflected beam by back-coupling at low power. The fact that the lattice beams form a  $\sigma^+ - \sigma^-$  pair proves to be unimportant as 1064 nm is far enough detuned from any atomic transition in  ${}^7\text{Li}$  that vector AC-Stark shifts are negligible, and the interference terms between different lattice beams are suppressed enough by relative detunings of 3 to 5 MHz (not commensurate with any inter-band transitions) that further isolation by orthogonal polarizations does not provide any benefit. It is worth noting that using the

positive and negative orders of AOMs to create beams with detunings of  $+\delta$  and  $-\delta$  is *not* sufficient to decouple the beams. In general, AOMs suffer from a one part in a hundred contamination of the positive order by the negative order and *vice versa*, due to photons scattered by the reflected acoustic wave, so that interference between the two beams can still cause transitions within the band structure.

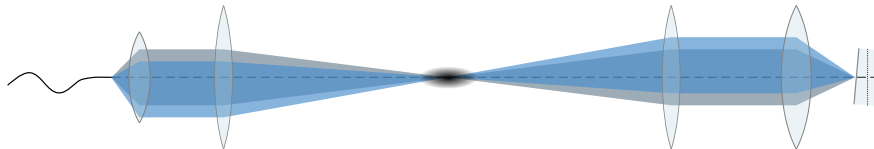


Figure 3.17: Cartoon of a lattice beam with cat-eye configured retro-reflection mirror. The forward-propagating beam (gray) is delivered by an optical fiber and focused onto the atoms. If the angle of the retro-mirror changes, the retro-reflected beam (blue) still passes through the atoms. Not pictured are folding mirrors, beam shaping optics and polarizing elements.

The lattice and ODT beams are all alignable via  $45^\circ$  mirrors with two-axis piezoelectric control (Newport Picomotor 8821). The minimum angular step-size of these devices is  $0.7 \mu\text{rad}$ ; they are placed before lenses which focus the beams onto the atoms ( $f = 300 \text{ mm}$ ) so that the position of the beams is adjustable with a minimum resolution of  $200 \text{ nm}$ . The ODT beams are shaped so that the beam waists at the atoms have a  $1/e^2$  radius of  $100 \mu\text{m}$ , while the lattice beams have waists of  $125 \mu\text{m}$ , which is the maximum size at which the intensity is high enough to reach a lattice depth of  $V_0 = 40E_R$  with the available power. The lattice beams are additionally retro-reflected by a gimbal-mounted mirror at the focus of an  $f = 50 \text{ mm}$  lens in a cat-eye configuration. The cat-eye lens and lattice focusing lens form an imaging system which images the waist of the beam (where the atoms are) onto the mirror surface; this geometry guarantees that the beam passes back through the atoms regardless of the angle of the retro-reflection mirror. Similarly, the beam waist in the chamber is the image of the fiber tip, so the retro-reflected light is also guaranteed to hit the fiber—although not necessarily with the correct angle for efficient fiber-coupling. This arrangement makes the lattice alignment quite insensitive to the angle of the retro mirror.

### Beam control and feedback

In addition to providing the frequency offset between the beams which is necessary to suppress interference, AOMs also provide intensity control, which can be used in a feedback loop to both

set the total intensity and cancel intensity noise. The frequency response of an AOM has two major components— a lowpass filtering behavior with characteristic frequency of about 3 MHz, and a constant time delay introduced by the propagation time of the sound wave in the AOM crystal, which is about  $1 \text{ mm} / (1000 \text{ m/s}) = 1 \mu\text{s}$ , as in figure 3.18. The additional phase shift accrued due to this time delay is quite significant, and has the effect of limiting the bandwidth of the AOM which is usable for feedback, as will be illustrated. The delay can in principle be reduced slightly by focusing the beam tightly and moving it closer to the transducer, but such a strategy is ultimately limited by thermal lensing in the AOM crystal for the high powers required by Lithium.

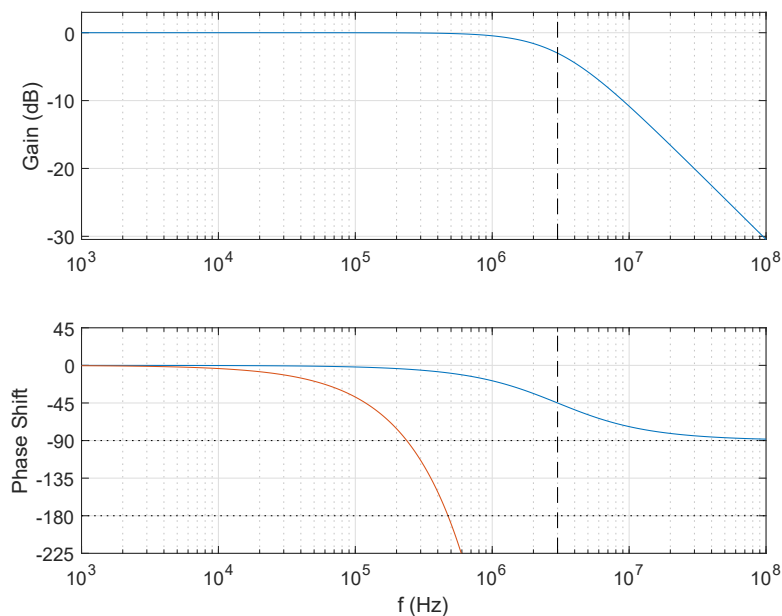


Figure 3.18: Bode plot of the transfer function of an AOM with a typical bandwidth of 3 MHz (indicated by vertical dashed dashed line). The blue lines show the gain and phase shift of an AOM that behaves only as a first-order lowpass filter. The red line shows the total phase shift, including the extra phase shift accrued due to  $1 \mu\text{s}$  of time delay.

Closed loop feedback is a fascinating topic with many implications for the work in this thesis and broad application in atomic physics generally, which will not be discussed in detail;<sup>2</sup> it suffices here to say that the open loop gain of a linear feedback circuit should cross 0 dB where the phase shift of the total loop, including the servo device, is less than  $180^\circ$ . This condition is necessary in order to maintain the stability of the circuit when the loop is closed, which means the PI-corner of a simple feedback controller should be set to wherever the total phase shift is  $-45^\circ$ . The controller

<sup>2</sup>A nice introduction to feedback can be found in [77].

gain can then be increased until the phase margin is too small to avoid amplification of noise beyond the loop bandwidth. In the presence of a time delay, however, the PI-corner must be set to significantly lower frequency (in the typical example of figure 3.18, at about 100kHz). Not only does this limit the low frequency noise-canceling gain, but it also allows any *output* noise of the controller at frequencies above the feedback bandwidth to be written into the light, where the AOM gain is still responding proportionally. Note that a feedback system driving a servo with simple first-order lowpassing behavior and *no* time delay would not have this problem, as noise above the feedback bandwidth would never reach the light. In heavier atoms, frequencies between 100kHz and 3 MHz should be relatively unimportant; in Lithium, however, this range corresponds precisely to the inter-band transitions that can be driven by intensity noise. The problem of excess output noise can be addressed by introducing a low-pass filter between the feedback controller and the AOM driver at a frequency corresponding to the time-delay-limited bandwidth, but this solution is not ideal, as it limits the feedback bandwidth even more. Further efforts to build a feedback controller with lower output noise therefore remain a priority.

### Alignment procedures

In order to ensure that spurious forces experienced by the atoms are minimized and to provide for adiabatic hand-off between the ODT and the lattice, the ODT beams must be aligned with the saddle point of the Feshbach field, and the lattice beams must be aligned with the crossed ODT. To that end, the following procedure has been developed:

1. After making a BEC in the crossed ODT, ramp down one of the ODT beams adiabatically. The BEC will then be confined by the combined potentials of the remaining ODT and the horizontal curvature of the magnetic field (this only works if the field is confining in the XY plane and anti-confining in Z). Draw a line perpendicular to the ODT which passes through the center of the cloud (see figure 3.19a).
2. Repeat with the other ODT beam. Move the ODTs to that position where the two center-lines cross, and confirm that the untrapped cloud experiences no horizontal forces.
3. Load a BEC in the ODT beams. Snap off both ODT beams and pulse on one of the three lattice beams at high power for a short time (at most 1/4 of the radial trap period in the lattice beam). After some time of flight, image the cloud along the beam axis. Its displacement from the trap center will be a dispersive function of the distance between the ODT and lattice beam centers, which close to perfect alignment displays linear sensitivity (see figure 3.19b).

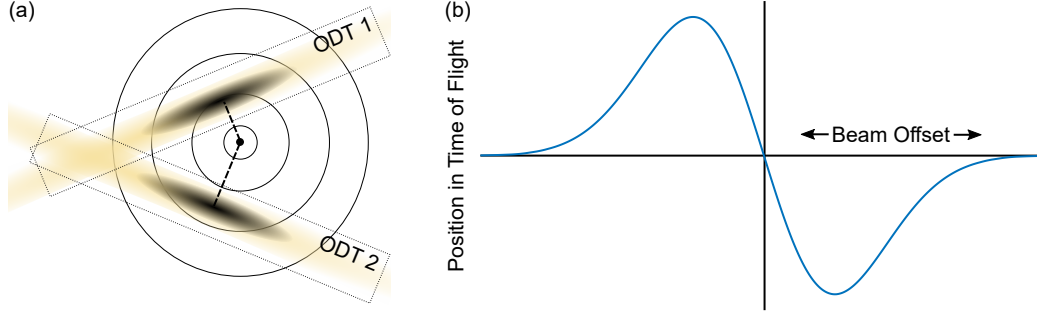


Figure 3.19: (a) Composite of the two-step alignment procedure to align the ODT beams with the magnetic field saddle point. The thin solid circles represent equipotential lines of the magnetic field in the XY-plane. (b) The position of the cloud in time of flight, after being kicked by a lattice beam which was offset along one axis from the ODT position.

The cloud displacement also scales linearly with the time of flight, which allows this method to magnify small offsets that would be difficult to resolve *in situ*.

4. Adjust the lattice beam until the kicked cloud remains at the same position in time of flight. Repeat with the other two lattice beams.
5. Align the retro-reflected beams by maximizing the back-coupled efficiency through the lattice fibers.

This method gives a lattice depth within a few percent of the expected value, given the measured beam power and waist size, suggesting that the alignment procedure is highly successful. A temperature stabilized enclosure surrounding the experiment ( $\pm 0.1^\circ\text{C}$ ) ensures the alignment procedure only has to be repeated every few weeks.

### Lattice calibration

The noise-driven processes discussed in section 3.3 can also be used intentionally to calibrate the lattice depth. When the lattice depth is modulated at a single frequency  $\omega_{\text{mod}}$ , peaks will be observed in the heating rate when  $\omega_{\text{mod}} = U/\hbar$ , as discussed in section 3.3.1, but also at  $\omega_{\text{mod}} = \omega_{1\rightarrow 3}$  (see figure ). The lattice depth can then be backed out of the band structure calculation of section 3.2.1, with a typical precision of 1%.

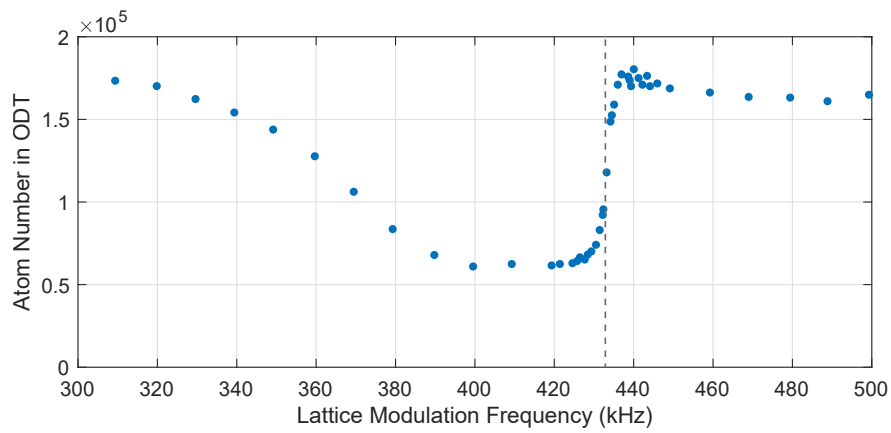


Figure 3.20: A near-degenerate thermal cloud is loaded into a lattice whose depth is modulated by 3% peak-to-peak for 30 ms. The number of atoms remaining is a function of modulation frequency, where the highest frequency response is associated with transitions between the ground and second excited bands at the center of the lattice (dashed line). The width of the feature is dominated by transitions between other bands, which take place at lower frequencies, and transitions at positions far from the trap center where the lattice is weaker. In a lattice made from 125 micron beams, the lattice depth varies by only 1% over  $\pm 20$  sites.

## Chapter 4

# Towards Simulations of Spin-1 Heisenberg Chains

## 4.1 Spin Models

One of the goals of the experimental platform described in this thesis is to provide a simple, tuneable analog system for Heisenberg models. These models share, as a defining feature, competition between nearest-neighbor exchange interactions along different axes or between these exchange interactions and other local terms. They provide insight into the behaviors of real materials, but even in the simplified context of toy models these behaviors can be difficult to compute, especially for large numbers of strongly interacting particles. The resulting systems contain not only states whose long range magnetic order is significantly influenced by the quantum nature of the spins themselves, such as  $xy$ -antiferromagnets, but also states displaying symmetry-protected topological order (SPT order) with robust, non-local correlations, such as the Haldane phase. This chapter describes progress towards simulating the dynamics and ground states of a spin-1 model that contains both of these features.

In 2006, Duan *et al.* showed that by matching up the matrix elements of a magnetic Hamiltonian and the matrix elements of the perturbative atomic Hubbard model (including terms up to second order in  $t/U$ ), it is possible to define a mapping between the two [78]. This mapping shows how the physical pseudospin configuration within the lowest Bloch band of an optical lattice is analogous to idealized quantum spins on a lattice. The model with a single fermion per site, corresponding to spin-1/2, has been studied extensively in fermionic regimes; recent successes include observation of 3D and 2D Néel ordering in fermions [11, 79], measurements of spin correlations in 2D spin-imbalanced systems [80] and spin-charge correlations in the presence of hole doping [16]. The bosonic system, however, which features the anisotropic exchange couplings and integer-spin models, remains unexplored.

### 4.1.1 Effective Hamiltonians and the Two-component Bose-Hubbard Model

While this chapter will focus mostly on implementing a spin-1 model, the spin-1/2 case provides a straightforward context in which to introduce the mapping and elucidates a few important differences between bosonic and fermionic models, while also providing a useful point of comparison for the spin-1 model. This section therefore begins by reviewing the spin-1/2 mapping, and then goes on to suggest how it can be extended to spin-1 [81].

## Spin-1/2

One of the simplest descriptions of a spin-1/2 system is the anisotropic Heisenberg model in an external magnetic field, which has the Hamiltonian

$$H_{\text{spin}} = \sum_{\langle i,j \rangle} \left( J_z S_i^z S_j^z + J_{xy} (S_i^x S_j^x + S_i^y S_j^y) \right) - h_z \sum_i S_i^z \quad (4.1)$$

where  $J_z$  and  $J_{xy}$  are the longitudinal and transverse exchange couplings, respectively, and  $h_z$  is the magnetic field. To see how this model can be implemented with cold atoms, consider the Bose-Hubbard model (3.16), which, when modified to describe a lattice of atoms with two possible internal states, reads

$$H = \underbrace{\sum_{\langle i,j \rangle, \sigma} \left( t_\sigma a_{i\sigma}^\dagger a_{j\sigma} + h.c. \right)}_V + \underbrace{\frac{1}{2} \sum_{i,\sigma} U_{\sigma\sigma} n_{i\sigma} (n_{i\sigma} - 1) + \sum_i U_{\uparrow\downarrow} n_{i\uparrow} n_{i\downarrow}}_{H_0} \quad (4.2)$$

for  $\sigma = [\uparrow, \downarrow]$ . The use of pseudospin indices is intended to recall the mapping, first introduced in section 1.2.2, between spins and hyperfine states of atoms. With two different hyperfine states, a composite spin- $n/2$  model can be constructed out of  $n$  atoms per site. The MI ground state of  $H_0$  provides plateaus of integer occupancy  $n$ , which constitutes a platform for any dynamics or ordering that may occur when spins are added to the system. In the limit of small  $t/U$ , as in section 3.2.2, one may treat the tunneling portion of the Hamiltonian perturbatively. With one atom per site (spin-1/2), the model has large manifold of degenerate ground states, which are all the possible configurations of pseudospins in the lattice. At finite  $t$ , however, the perturbation  $V$  will lift this degeneracy. As in the single-component MI, there are no first-order corrections to the energies. Following Complement B<sub>I</sub> of [82], the matrix elements of the effective Hamiltonian for perturbation  $V$ , to second order, are given by

$$\langle m | H_{\text{eff}} | n \rangle \approx E_n \delta_{nm} + \langle m | V | n \rangle + \frac{1}{2} \sum_k \langle m | V | k \rangle \left( \frac{1}{E_m - E_k} + \frac{1}{E_n - E_k} \right) \langle k | V | n \rangle, \quad (4.3)$$

which can then be compared to the matrix elements of  $\langle m | H_{\text{spin}} | n \rangle$ , where the states  $\langle m |$  and  $| n \rangle$  are the different positional configurations of nearest-neighbor spins/hyperfine states. This process

leads to four equations which can be solved simultaneously to find the coefficients of the spin Hamiltonian in terms of the coefficients of the effective atomic Hamiltonian:

$$J_z = \frac{t_{\uparrow}^2 + t_{\downarrow}^2}{2U_{\uparrow\downarrow}} - \frac{t_{\uparrow}^2}{U_{\uparrow\uparrow}} - \frac{t_{\downarrow}^2}{U_{\downarrow\downarrow}}, \quad J_{xy} = \pm \frac{t_{\uparrow}t_{\downarrow}}{U_{\uparrow\downarrow}}, \quad \text{and } h_z = z \left( \frac{t_{\downarrow}^2}{U_{\downarrow\downarrow}} - \frac{t_{\uparrow}^2}{U_{\uparrow\uparrow}} \right), \quad (4.4)$$

where  $z$  is again the coordination number of the lattice, and the  $-(+)$  sign in  $J_{xy}$  is for bosons (fermions), due to the parity of the wavefunction with respect to exchange of particles in each case. The term  $h_z$  is a magnetic field in the  $\hat{z}$  direction in the spin model (not the real magnetic field  $B$ ), which in this cold atoms system is fixed by the net magnetization  $M = N_{\uparrow} - N_{\downarrow}$  and is therefore identically zero when the system contains the same number of  $a$  atoms and  $b$  atoms. There is also a total constant energy offset equal to  $\epsilon = -(t_{\uparrow}^2 + t_{\downarrow}^2)/(2U_{\uparrow\downarrow}) - t_{\uparrow}^2/U_{\uparrow\uparrow} - t_{\downarrow}^2/U_{\downarrow\downarrow}$ , which can be dropped from the Hamiltonian without loss of generality.

For fermions,  $U_{\uparrow\uparrow}$  and  $U_{\downarrow\downarrow}$  are infinite, due to the Pauli exclusion principle, so  $J_z = J_{xy}$ , with positive  $U_{\uparrow\downarrow}$  favoring anti-ferromagnetic order in both  $z$  and  $xy$ . The system therefore implements an isotropic spin-1/2 Heisenberg model, which can be switched between ferromagnetic and anti-ferromagnetic order by switching the sign of  $U_{\uparrow\downarrow}$  via, for example, a Feshbach resonance. The story is quite different for bosons, however:  $U_{\uparrow\uparrow} \neq U_{\downarrow\downarrow}$  in general, leading to competition between the  $J_z$  and  $J_{xy}$  terms and the reintroduction of the bias field  $h_z$ . At the same time, the overall sign of  $J_{xy}$  is switched, so that *negative*  $U_{\uparrow\downarrow}$  favors anti-ferromagnetic coupling in the transverse direction. Varying the three interactions relative to one another therefore is expected to realize a wide variety of phases. One can gain some insight into the different ground state configurations by considering the spin Hamiltonian acting on trial states that are the classical magnetic ground states, as has been done by Altman *et al.* [81], but it turns out that applying this mean-field picture to the spin-1 configuration reveals only a part of the story.

## Spin-1

With two atoms per site and two hyperfine states  $a$  and  $b$ , the three possible configurations,  $|+1\rangle = |aa\rangle$ ,  $|0\rangle = (|ab\rangle + |ba\rangle)/\sqrt{2}$  and  $|-1\rangle = |bb\rangle$ , form a spin triplet manifold on each lattice site.<sup>1</sup> These are unique to bosons; fermions would instead form the spin singlet  $(|ab\rangle - |ba\rangle)/\sqrt{2}$ .

<sup>1</sup>Hereafter, for compactness, these three states will be referred to as  $|aa\rangle$ ,  $|ab\rangle$ , and  $|bb\rangle$ , using the Fock basis notation.

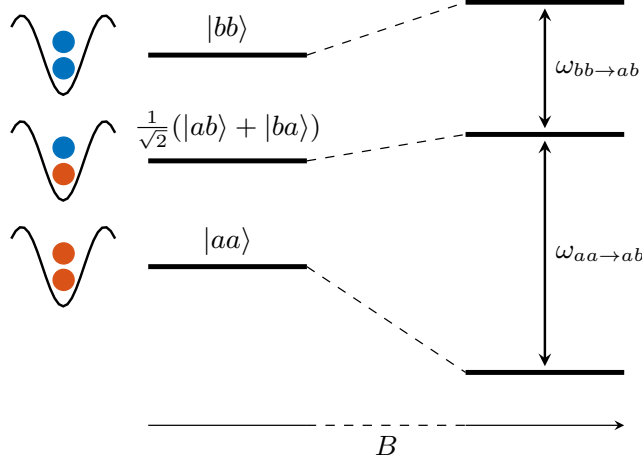


Figure 4.1: The three different combinations of two hyperfine states on a lattice site have interaction energies  $U_{aa}$ ,  $U_{ab}$ , and  $U_{bb}$  which can be tuned via Feshbach resonances. At a given field  $B$ , the splittings will in general be unequal, giving rise to an interaction blockade: the two possible transitions can be individually addressed by an RF drive with frequency  $\omega = \omega_{Zeeman} + \Delta U/\hbar$ .

As in the spin-1/2 system, the nearest neighbor interactions arise from super-exchange. Because of Feshbach resonances,  $U_{aa} \neq U_{bb} \neq U_{ab}$  in general: they are functions of the applied magnetic field  $B$  so that one can tune the configurational energies of different distributions of spins in the lattice (Fig. 4.1). The appearance of a spin triplet is already quite suggestive of the presence of an analog to a spin-1 model. It is helpful to first zero the energy of the  $|0\rangle$  state by subtracting an overall energy offset  $U_{\uparrow\downarrow}$ , and then to subtract the energy due to a fictitious magnetic field  $h_z = (U_{\uparrow\uparrow} - U_{\downarrow\downarrow})/2$ , which affects only the  $|\pm 1\rangle$  states and sets their energies to  $\pm D$ . As before, this fictitious magnetic field has no effect within a subspace of fixed magnetization, determined by the hyperfine state populations. One may then proceed as in the spin-1/2 case by finding the matrix elements of the effective atomic Hamiltonian (see figure 4.2) and collecting terms with the same spin operators, which results in

$$H = J \sum_{\langle i,j \rangle} S_i \cdot S_j + D \sum_i (S_i^z)^2 + \mathcal{O}(\delta^2) . \quad (4.5)$$

The correction terms of order  $\delta^2$  come from the normalized difference between the intra-spin interactions  $\delta = (U_{\uparrow\uparrow} - U_{\downarrow\downarrow})/(U_{\uparrow\uparrow} + U_{\downarrow\downarrow})$ , and affect only states of the form  $|\pm 1\rangle_i |0\rangle_{i+1}$ . The terms of order  $\delta$  have meanwhile been removed by the previous introduction of the fictitious magnetic field, which can now be written as  $h_z = -zJ \cdot 3\delta/2$ , and which provides, as usual, just a constant energy

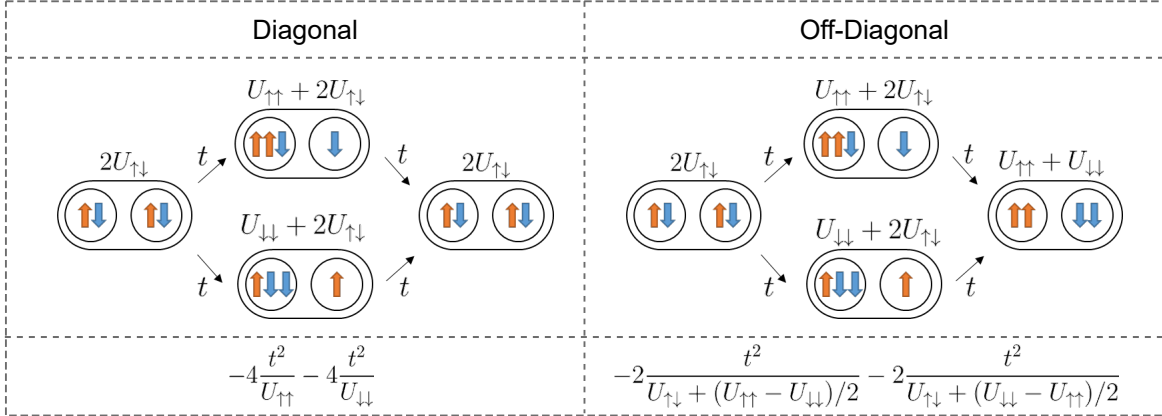


Figure 4.2: Pictorial representation of the calculation of two example matrix elements of the effective Hamiltonian— one diagonal and one off-diagonal— to second order in  $t/U$ . The tunneling is presumed to be uniform, i.e. there is no state-dependent lattice potential.

offset while constrained to a subspace of constant magnetization. The coefficients themselves take the forms

$$J = -4 \frac{t^2}{U}, \text{ and } D = \frac{U_{\uparrow\uparrow} - U_{\downarrow\downarrow}}{2} - U_{\uparrow\downarrow} \quad (4.6)$$

for an effective  $U$  which is the harmonic interactions of the two intra-spin interactions

$$U \equiv \frac{2}{1/U_{\uparrow\uparrow} + 1/U_{\downarrow\downarrow}}. \quad (4.7)$$

While the spin exchange term in the approximate Hamiltonian (4.5) is again simply the unadorned Heisenberg model, a number of differences from the spin-1/2 case are immediately clear. In the bosonic spin-1/2 system, the model has an exchange coupling anisotropy which depends on the difference in intra-state interactions, while the exchange coupling in the spin-1 model is isotropic regardless of the interactions. On the other hand, in the spin-1/2 system, the ground state is degenerate at  $t/U = 0$ , whereas in the spin-1 system the states already have different energies, which leads to the local spin-squeezing term  $(S_i^z)^2$  in the Hamiltonian.<sup>2</sup> Further, the exchange interaction in the spin-1/2 model depends only on  $U_{\uparrow\downarrow}$ , while the exchange interaction in the spin-1 model does not depend on  $U_{\uparrow\downarrow}$ , but only on  $U_{\uparrow\uparrow}$  and  $U_{\downarrow\downarrow}$ , and additionally picks up a factor of four due to having two bosons per site. Finally, the mapping to spin-1/2 is exact, while the mapping to spin-1 is exact only up to first order in  $\delta$ , and the form of the corrections may be important when

<sup>2</sup>The spin-squeezing term is sometimes referred to in condensed matter literature as single-ion anisotropy, uniaxial large ion anisotropy, or easy-axis anisotropy.

considering the symmetries of the Hamiltonian.

### Ground state phase diagram

This Hamiltonian describes the competition between an exchange term  $S_i \cdot S_j$ , which favors correlations between sites, and a spin-squeezing term  $|S_i^z|^2$ , which favors only local (on-site) pairing. When  $D$  is large and positive, the  $|0\rangle$  state is strongly favored everywhere, leading to a ground state, in the limit  $D \rightarrow \infty$ , which can be written as

$$|\Psi\rangle = \prod_i |0\rangle_i , \quad (4.8)$$

where  $|0\rangle$  indicates the spin zero state of two atoms (and not a zero-occupancy site). This product state of doublons, or *Spin Mott*, is highly reminiscent of the MI ground state (3.24), and in the context of magnetic ordering behaves like a Z-paramagnet. When  $D$  is large and negative, however, the spins are constrained to be  $|\pm 1\rangle$  on each site, and any residual exchange coupling leads to Ising-type interactions. Finally, the Hamiltonian has a special point defined by

$$U_{\uparrow\uparrow} + U_{\downarrow\downarrow} = 2U_{\uparrow\downarrow} , \quad (4.9)$$

which is the point at which  $D = 0$  and the super-exchange process  $|1\rangle_i |-1\rangle_{i+1} \Leftrightarrow |0\rangle_i |0\rangle_{i+1}$  becomes resonant. At this *degeneracy point* (DGP), what remains is an isotropic Heisenberg Hamiltonian, and the ground state then depends on the total spin, the dimensionality of the lattice, and on the lattice coordination number  $z$ . Further, when  $D/|J|$  approaches 1 from the positive side, one might expect competition between the terms of the Hamiltonian to lead to a phase transition between the uncorrelated state (4.8) and a state that displays some sort of exchange-mediated ordering.

In fact, spin-1 chains of this sort have been the topic of significant study in the context of condensed matter systems ever since Haldane's 1983 prediction that the ground state of 1D chains of integer spins is gapped, contrary to the gapless spectrum of spin-wave excitations on an XY-antiferromagnetic phase that a mean field phase diagram would suggest [12]. Importantly, Afflek

*et al.* showed that the larger class of 1D spin Hamiltonians

$$H = \sum_i [\mathbf{S}_i \cdot \mathbf{S}_{i+1} - \beta(\mathbf{S}_i \cdot \mathbf{S}_{i+1})^2] \quad (4.10)$$

exhibit the same symmetries as the Heisenberg Hamiltonian, and furthermore that 4.10 has an exactly solvable ground state for the case of  $\beta = 1/3$  (the Heisenberg Hamiltonian is recovered for the case of  $\beta = 0$ ) [83]. The construction of this so-called *valence bond* state arises from the realization that each spin-1 site can be viewed as the symmetric combination of two spin-1/2 particles on the same site (in the case of the model implemented in this work, this configuration exists in real space, but in the original theoretical work it was simply a construction). These constituent spin-1/2 particles can form a spin singlet with neighboring spin-1/2 particles  $|\uparrow\rangle_i |\downarrow\rangle_{i+1} - |\downarrow\rangle_i |\uparrow\rangle_{i+1}$ . The symmetric combination of the two spin-1/2 particles on each site restores the total spin on each site to  $S=1$ . This construction makes the origin of the gap very clear (the excitations are spin singlets, not spin waves), but also brings to light another interesting feature of the model: in an open chain, there will be un-paired spin-1/2 particles at the ends, which gives rise to a four-fold degenerate ground state. In their second paper on the topic, Affleck *et al.* showed that these four ground states consist of a spin triplet and a spin singlet, the latter of which is a fundamentally non-local state [84, 85]. Several condensed matter groups measured the presence of a Haldane gap in crystalline materials (see [86] for a partial list), but it is only quite recently that a fuller understanding of the Haldane ground state has been developed. The ground state of the isotropic spin-1 Heisenberg model is one of the simplest examples of a Symmetry Protected Topological (SPT) phase [87, 88]. These phases feature order which is protected by some symmetry of the Hamiltonian, in contrast to intrinsic topological order, which is robust even in the presence of any local perturbations. It was originally proposed that the Haldane phase in spin-1 chains was protected by inversion symmetry [89]. More recently, Gu and Wen pointed out that violating any one of inversion, translation or time-reversal symmetry will lead to a decay of the string-ordered correlations that characterize the Haldane phase [90].

The model Hamiltonian (4.5) features a competition between the Heisenberg exchange term and a spin squeezing term, leading to a first-order phase transition between the spin-squeezed paramagnetic phase and the Haldane phase. Sakai and Takahashi showed that the Haldane phase

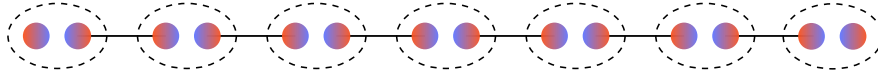


Figure 4.3: The valence bond ground state. Symmeterized spin-1 lattice sites are represented by the dashed ovals. The solid lines represent the “valence bonds” completing the off-site anti-symmetric spin singlets  $|\uparrow\downarrow\rangle - |\downarrow\uparrow\rangle$ . Illustration based on [84].

persists in quasi-1D— that is, in a lattice of chains with weak inter-chain coupling [91]. Pollman *et al.* argue, however, that the Haldane phase really only exists for *odd*-integer spins in 1D (and not just integer spins, as Haldane originally conjectured), and correspondingly in the quasi-1D situation, the number of coupled tubes must be odd (e.g. no spin ladders) [13]. Similarly, Gong *et al.* argue that the Haldane phase persists in the presence of weakly anisotropic spin coupling [92]. A simulator of the sort described in this work, with tunable parameters and access to a selection of ground states in the phase diagram, ought to add substantially to the data which have been gleaned from condensed matter systems.

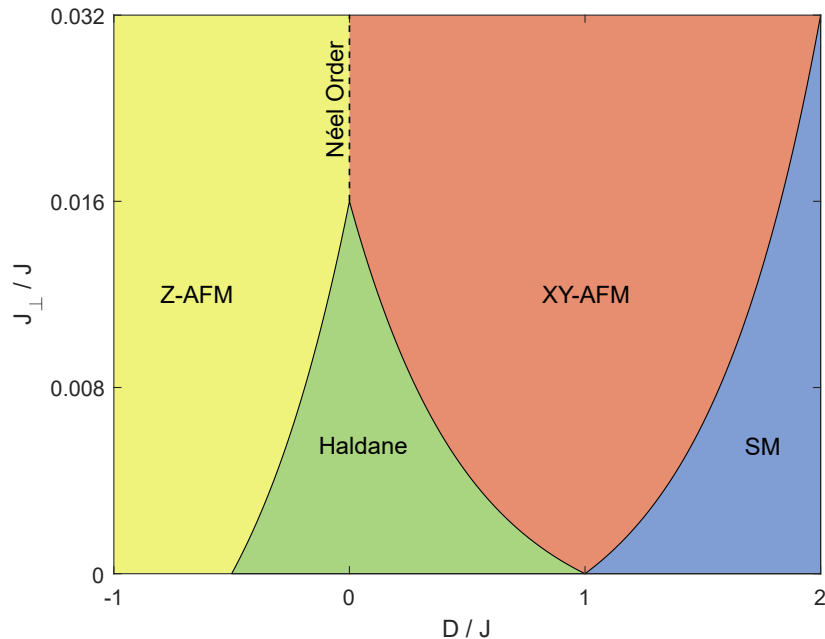


Figure 4.4: Cartoon of the phase diagram of the quasi-1D spin-1 chain with antiferromagnetic exchange interactions, as a function of the spin-squeezing parameter  $D/J$  and the inter-chain coupling strength  $J_{\perp}/J$ . In isolated chains, the system features only three phases: the Spin Mott, the Haldane phase and the Ising-type  $z$ -antiferromagnet. As weak inter-chain coupling is re-introduced, the system gains another phase that competes with, and eventually overwhelms, the Haldane phase. This phase is the quantum  $xy$ -antiferromagnet (XY-AFM). While the point on the  $D/J$  axis where the Haldane and SM phases touch is a first order phase transition, the SM to XY-AFM transition is a mean field transition. This figure is based on work by Wierschem and Sengupta [86, 93] and Sakai and Takahashi [91].

### 4.1.2 Ingredients for an atomic spin-1 model

The ability to implement a spin-1 model with neutral cold atoms in optical lattices thus has a number of specific requirements, especially if one is interested in accessing the (arguably more interesting) anti-ferromagnetic exchange couplings. First, one needs a two-component system which forms a spin triplet on each site, which implies a bosonic atom with two hyperfine states. The two hyperfine states should be stable against spin-changing collisions, which strongly favors stretched or hyperfine ground states. There should be some way to vary the interactions between these two states, in a regime which includes (1) all on-site interactions large enough to be in the MI at reasonable lattice depth and (2) differences between the interaction energies of comparable magnitude, ideally the same at one point. The exchange energy  $J$  must be positive to achieve anti-ferromagnetic coupling in bosons, for which it is a necessary (but not sufficient) condition that one or both of  $U_{\uparrow\downarrow}$  and  $U_{\downarrow\downarrow}$  be negative. The magnitude of the rate  $J/\hbar$  should also exceed the decoherence rate in the lattice, so that many super-exchange events may take place before the introduction of excitations that break up the spin chain and limit the correlation lengths of magnetically ordered states. And finally, there should be some way to prepare one of the ground states in the spinful phase diagram from a ground state in the single-component system.

Given these requirements,  $^7\text{Li}$  presents a number of unique advantages compared to other atomic systems, but also several challenges. The two lowest hyperfine states have a unique spectrum of Feshbach resonances that includes a double-resonance in the  $b$  state (see figure 4.9b). This particular structure provides for a unique opportunity to scan  $U_{bb}$  over a wide range while  $U_{aa} > U_{ab}$  remain almost constant, which provides for the variation of  $D/J$  between  $\pm\infty$ , as will be discussed in greater detail in section 4.3.2. In the same region of magnetic field, all the relevant scattering lengths are negative, providing for anti-ferromagnetic interactions. While the integer-occupancy density distribution of the MI with this configuration is the actually most excited Hubbard band, it is meta-stable in a 3D optical lattice for the simple reason that atoms which would tunnel to neighboring sites have no way to dispose of the potential energy they would lose; the lifetime of the attractive MI is therefore not detectably shorter than the lifetime of the normal repulsive MI, as has been observed in two-component MIs in this experiment and previously in single-component  $^{137}\text{Cs}$  [94]. The magnitudes of the scattering lengths are also important, as they fix the depth of

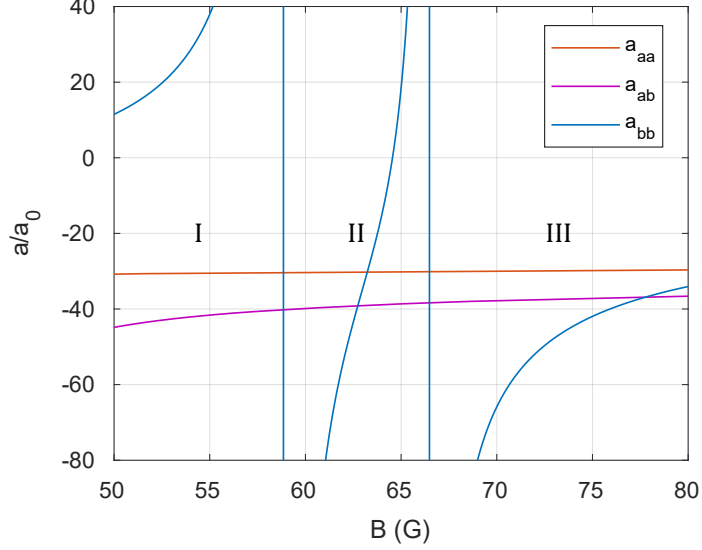


Figure 4.5: Scattering lengths of  $^{39}\text{K}$  around the low field  $bb$  resonance. Regions II and III exhibit degeneracy points for an  $n=2$  system with  $a$  and  $b$  atoms. Feshbach resonance data for  $^{39}\text{K}$  is taken from [95].

the lattice at which the experiment must be performed, to which the parameter  $J$  is exponentially sensitive: the MI transition happens at fixed  $t/U$ , so  $J \sim U \cdot (t/U)^2 \sim U \cdot \text{const}$ . Fortunately, the magnitudes of the scattering lengths in the lowest two hyperfine states of  $^7\text{Li}$  are all at least  $50a_0$ . The super-exchange rate is also benefited by the light mass of Li through  $U \sim m^{-1}$ . Lastly, at the high bias field where the Feshbach resonances are found, the Zeeman detunings of the two states also have similar slopes, which grants a degree of magnetic field insensitivity to the RF-transitions necessary for initialization and readout ( $\mu_{\text{rel}} \approx 0.02 \mu_B$ ). On the other hand, the Feshbach resonance that allows for the tuning of  $D/J$  is rather narrow, so that precision control of the bias field is still required (to better than one part in  $10^5$ ). Furthermore,  $^7\text{Li}$ 's light mass and fast tunneling are accompanied by high three-body loss rates, especially near Feshbach resonances. How these effects balance each other will be the subject of section 4.3.3.

It is worth considering what other atomic systems might afford an opportunity to explore this model, and what portion of the parameter space would be available to them. To this author's knowledge, the sort of Feshbach resonance structure that affords both anti-ferromagnetic coupling and the ability to scan  $D/|J|$  through the region containing the phases depicted by figure 4.4 exists elsewhere in bosonic alkalis only in the lowest two hyperfine states of  $^{39}\text{K}$  (figure 4.5). The relevant scattering lengths in this region are, however, more than a factor of two smaller than those in

${}^7\text{Li}$ , which decreases the maximum achievable super-exchange coupling by the same factor. The heavier mass of  ${}^{39}\text{K}$  reduces the super-exchange even further. On the other hand, the relevant Feshbach resonance structure exists at substantially lower magnetic field and the slope of the tuneable interaction (again  $bb$ ) is shallower, requiring much less dynamic range for magnetic field feedback. Ultimately, the most important concern would be the two- and three-body loss rates near the  $bb$  Feshbach resonance, for which published results are not yet available. While it is possible that  $J/(\hbar\Gamma_{\text{loss}})$  would be promising, a definite determination requires further study. One might also attempt such a simulation in atoms which have no Feshbach resonance, rather using spin-dependent lattice to vary  $U_{ab}$ . These atoms would universally have  $U > 0$  for all possible interactions if they can form a stable spin mixture (e.g.  ${}^{87}\text{Rb}$ ), and so in order to achieve anti-ferromagnetic exchange coupling, one could reverse the sign of super-exchange by tilting the system with an optical gradient so that  $J = t^2/U \rightarrow t^2/(U + \Delta) + t^2/(U - \Delta) = 2t^2U/(U^2 - \Delta^2)$  [23]. In the case of  ${}^{87}\text{Rb}$ ,  $U_{aa} \approx U_{bb} \approx .986 U_{ab}$ , and because the spin-dependent lattice reduces  $U_{ab}$  but leaves the intra-species interactions unchanged,  $D/|J|$  can actually access the entire range of parameters necessary to realize the phase diagram of figure 4.4.

Attempts have also been made to model spin-1 Heisenberg spin chains using trapped ions [96]. The JQI group has recently implemented a spin-1 simulator with short chains of ions (up to  $n=4$ ) that models a version of the anisotropic Heisenberg Hamiltonian with spin squeezing and long-range interactions (rather than nearest-neighbor). The addition of long range interactions frustrates the XY-order that might otherwise arise in 1D in the presence of anisotropic exchange coupling, although it is predicted that the Haldane phase persists if the coupling is weak enough [97]. However, the reduced dimensionality of the system prevents adiabatic preparation of the Haldane phase from the large-D phase (Spin Mott): by definition, a state with symmetry protected topological order is not adiabatically transformable into a topologically trivial state— that is, a product state like the large-D phase. It remains an open question, at least experimentally, whether an  $xy$ -antiferromagnetic phase can be adiabatically transformed into the Haldane phase in the presence of suitable symmetry-breaking perturbations— a question which future work on this  ${}^7\text{Li}$ -based quantum simulator may help to answer.

## 4.2 Interactions in ${}^7\text{Li}$

In order to find out the appropriate magnetic fields which implement various parts of the phase diagram of the anti-ferromagnetic spin-1 Heisenberg chain, it is necessary to know the on-site interactions in  ${}^7\text{Li}$  to better than the scale of  $J$ , which ranges from a few hundred Hertz to a kilohertz, depending on dimensionality. Before the work discussed in this thesis, the Feshbach resonances in  ${}^7\text{Li}$  had not been characterized so precisely, and what is more, the crucial  $ab$  resonance had never been measured at all. This following section is a discussion of direct measurements of the on-site interaction energies  $U_{aa}$ ,  $U_{ab}$  and  $U_{bb}$ , which constitute the direct inputs to the many-body Hamiltonian 4.5, by applying a technique which has not previously been used to characterize Feshbach resonances [36]. The use of an optical lattice is crucial for stabilizing the density of the ground state two-component mixture at a variety of combinations of scattering lengths, including when all or some of these scattering lengths are negative or have vastly different magnitudes.

### 4.2.1 Interactions on a Lattice Site

Section 3.2.1 derived the on-site interaction energy  $U$  from the overlap integral of two Wannier functions, which is valid in the limit of  $U \ll \omega_{\text{bg}}$ , so that higher bands may be neglected. While this limit is satisfied for the scattering lengths used in the lattice under normal experimental conditions, Feshbach resonance spectroscopy involves some measurements at relatively high scattering length (up to  $250 a_0$ ).

#### The Busch model

Busch *et al.* showed that there is an exact analytic solution for the energies in the case of two atoms with contact interactions occupying a spherical harmonic trap [98]. The Hamiltonian can be diagonalized when the interactions are expressed in terms of the regularized delta-function  $\delta_{\text{reg}}(\mathbf{r}) \equiv \delta^{(3)}(\mathbf{r})(\partial/\partial r)r$ , where  $r$  is the relative coordinate of motion. The modified eigenenergies obtained from this process, plotted in figure 4.6, can be expressed by

$$a = \frac{1}{\sqrt{2}} \frac{\Gamma(-E/2 + 1/4)}{\Gamma(-E/2 + 3/4)}. \quad (4.11)$$

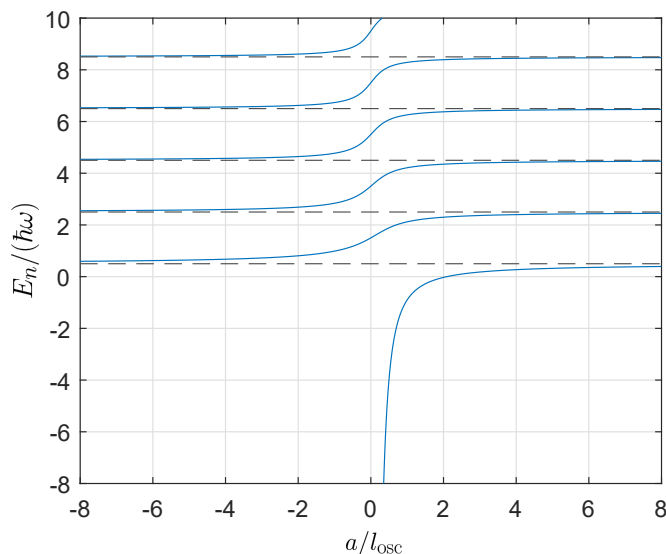


Figure 4.6: Exact solution to the energy of two interacting atoms in a spherical harmonic trap with trap frequency  $\omega$ , as a function of the scattering length  $a$ . The dashed lines are the asymptotic energies reached as  $a \rightarrow \pm\infty$  at a resonance.

This result beautifully captures several salient aspects of the system of two confined, interacting particles. First, the energy shift experienced due to attractive (repulsive) interactions saturates at  $+(-)\hbar\omega$ , which is to say the magnitude of an effective scattering length  $a$  saturates at the harmonic oscillator length  $l_{\text{osc}} \equiv \sqrt{\hbar/(m\omega)}$ . Second, passing through a resonance from the  $+\infty$  side promotes the atoms from oscillator level  $n$  to level  $n+1$ , and *vice versa* for passage in the opposite direction. Finally, the calculation illustrates the formation of a bound molecular state of the two atoms in the lowest state for  $a > 0$ , shifted upwards by the ground state trap energy  $1/2\hbar\omega$ .

## Interaction Blockades

Much of the work that follows will make use of the fact that interactions in a many-body system split the degeneracy in the excited state, shifting the energy levels of an otherwise a harmonically spaced system by the difference in the interaction energies in each state. These shifts, or *interaction blockades*, have been observed in a variety of quantum systems, including neutral atoms in the context of RF spectroscopy of MI shells [99] and inter-band transitions in a optical lattice [100], and in Rydberg atoms, where the so-called “dipole blockade” has been used to implement a variety of engineered interactions and quantum gates [21, 101, 102]. In an  $n$  particle system, this situation

is further characterized by a collective enhancement of the Rabi frequency, e.g. by  $\sqrt{n}$  for the transition between the ground state and the state with one quantum of excitation. In the simplest case of two particles, each in either states  $|a\rangle$  or  $|b\rangle$ , this effect makes the transition from state to the superposition state  $|ab\rangle + |ba\rangle$  addressable independently of the transition to the fully excited state  $|bb\rangle$  (see figure 4.7). Such interaction blockades will play an important role not only in spectroscopically characterizing the interactions of  ${}^7\text{Li}$  and the distributions of occupancies in the optical lattice, but also in coherent control of the hyperfine states in an occupancy-dependent way.

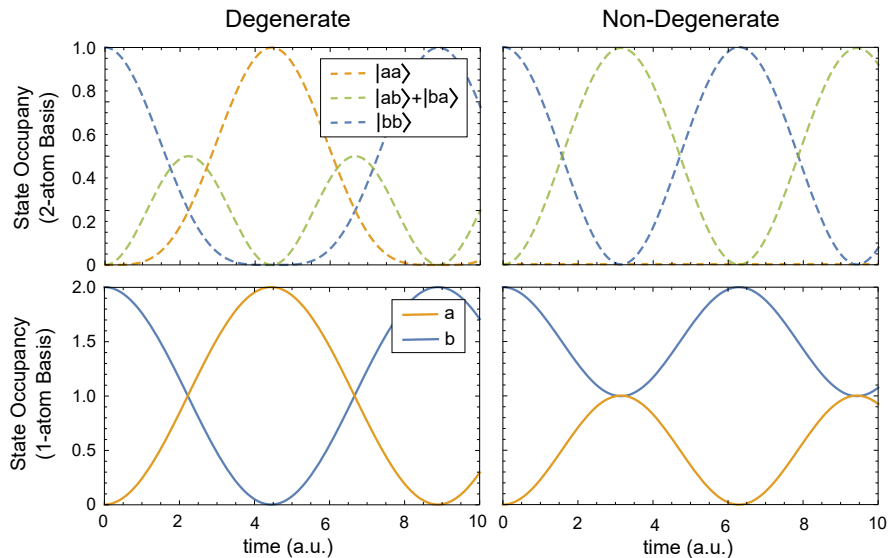


Figure 4.7: Rabi oscillations of two interacting bosons. The left panels depict the case where the interactions in all three possible configurations are degenerate, whereas the right panels depict the case where the drive is resonant only with the  $|bb\rangle \rightarrow |ab\rangle$  transition. The upper panels show the expectation value of the state occupancy in the basis of the two-atom states, while the bottom panels show the total detection probabilities for atoms in each hyperfine state. The non-degenerate case exhibits half the contrast but a  $\sqrt{2}$  enhancement of the Rabi frequency compared to the degenerate case, which is typical of an interaction blockade effect.

## 4.2.2 Interaction Spectroscopy

In order to measure the differential interaction energy of two confined atoms as a function of magnetic field, the system is prepared in an  $n=2$  Mott insulator in the  $b$  hyperfine state. The number of atoms is  $1 \times 10^5$  and the lattice depth is  $35 E_R$  in each dimension. The central  $n=2$  plateau, approximately  $3 \times 10^4$  sites, is surrounded by an  $n=1$  shell containing a similar number

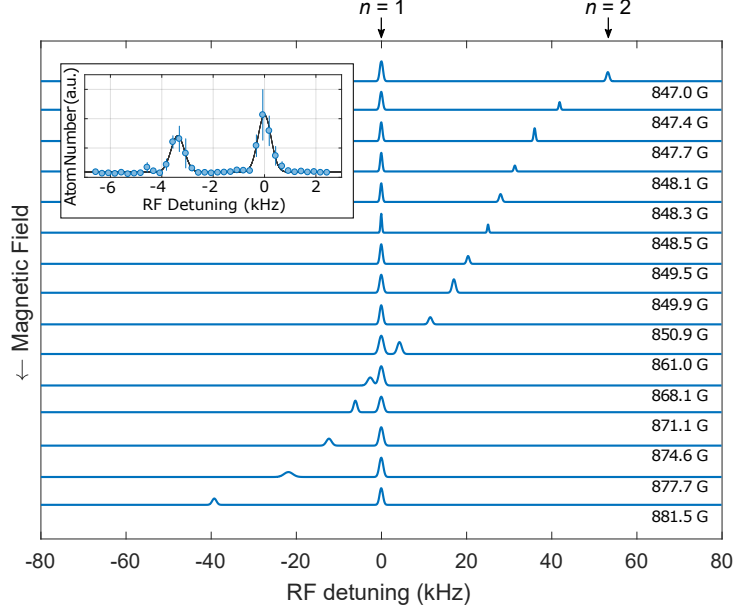


Figure 4.8: Fits to representative spectra of the transition between  $b$  and  $a$ , taken between the two  $bb$  Feshbach resonances. The spectra have been plotted so that the Zeeman-shifted peaks of the  $n=1$  transitions overlap. The inset shows an example spectrum in which each point is an average of four measurements and the fit is a sum of two Gaussians. The crossing of the frequencies of the two peaks corresponds to  $U_{ab} - U_{bb} = 0$ .

of sites. The RF drive is pulsed for 2.9 ms and monitor the number of atoms in the other hyperfine state as a function of drive frequency. At the frequency corresponding to the transition of a bare atom, a peak is observed coming from the atoms on  $n=1$  sites. A second peak is observed coming from the  $n=2$  atoms, which is shifted by the difference in interaction energy between the initial state ( $|aa\rangle$  or  $|bb\rangle$ ) and the final state ( $|ab\rangle$ ). The pulse length corresponds to a  $\pi$ -pulse for the  $n=2$  sites (so that the signal is maximized), which have a Rabi frequency  $\sqrt{2}$  greater than that of the  $n=1$  sites, due to bosonic enhancement. The interaction blockade that arises from unequal interaction energies in the three states means that one may drive the system selectively between  $|aa\rangle$  and  $|ab\rangle$  (or  $|bb\rangle$  and  $|ab\rangle$ ). Thus when the atoms are probed absorptively after an RF pulse with light that is resonant only for  $a$  (or  $b$ ), a single flipped atom per  $n=2$  site is measured (see the inset of figure 4.8).

The frequency of the  $n=1$  peak corresponds to the Zeeman shift and thus to the magnitude of the applied magnetic field (the hyperfine constant and nuclear g-factor for  ${}^7\text{Li}$  are taken from [103]). The frequency shift of the  $n=2$  peak, which may be positive or negative, is a direct measure of the differential two-body interactions. Using this technique, RF spectra are obtained at many

selected bias fields from which the two-body interaction splittings  $U_{bb} - U_{ab}$  and  $U_{ab} - U_{aa}$  (Fig. 4.8) can be derived. The technique works equally well for attractive and repulsive interactions, so long as the system remains in the Mott insulating state.

The precision to which the differential interaction energies on a site must be determined is set by the super-exchange rate, which at Mott insulator depths for  ${}^7\text{Li}$  in a 1064 nm optical lattice ranges from hundreds of hertz to several kilohertz, depending on lattice depth and dimensionality. Here the differential interaction energies are measured as a function of magnetic field to a precision of about 100 Hertz, limited only by the stability of the magnetic field (about one part in  $10^5$  at  $10^3$  G) and the sensitivity to magnetic fields of the RF-transition between the two hyperfine states (approximately 33 kHz/G at high field). Each  $n=2$  spin flip data point includes an independent calibration of the magnetic field via the  $n=1$  spin flip. Each of these measurements includes 100 points, sampled 3x each. At 10s/point, this is about an hour of data-taking during which the magnetic field can drift. However, the data used to determine the interaction shift at a certain field are taken out-of-order, and so the field drift is expected only to broaden the resonances, not shift their positions. Indeed, the  $n=1$  resonances approach Gaussians with standard deviation of about .5-.7kHz. Therefore, an upper bound on the field noise is a Gaussian distribution with a width of  $0.7\text{kHz}/(33\text{kHz/Gauss})=20\text{mG}$ . This value is very much an upper bound, as (1) it does not take into account the intrinsic width of the spin-flip resonances due to finite probe time and (2) the dense sampling of the resonance means drift should not significantly affect the positions of the resonances, but rather their widths. As the interaction energies range over many tens of kilohertz, the error bars are too small to see on a full scale plot (Fig. 4.9a). The technique of RF interaction spectroscopy is particularly well-suited to atoms with characteristically large interaction energies, such as Li, because the wide separation between singlon and doublon spin-flip resonances permits the use of high Rabi frequencies, which maximizes signal size and decreases sensitivity to magnetic field noise.

### **Amplitude modulation spectroscopy**

While RF spectroscopy in a lattice is a powerful and precise tool for characterizing differential interactions, another technique is necessary to measure the absolute interaction energy (i.e.  $U_{aa}$  or  $U_{bb}$ ), for these interactions determine the lattice depth for the transition to the Mott insulator

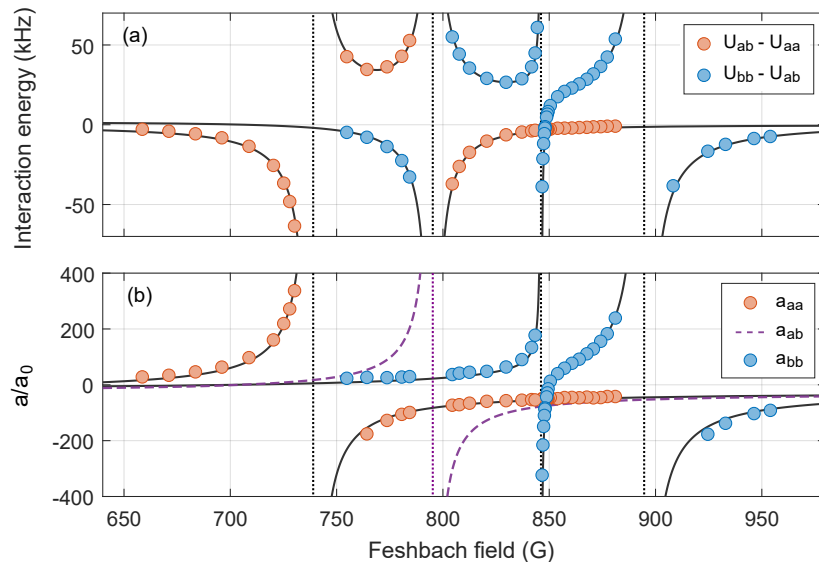


Figure 4.9: (a) The relative interactions  $U_{ab} - U_{aa}$  and  $U_{bb} - U_{ab}$  are plotted as a function of magnetic field, measured via RF interaction spectroscopy in 35, 35, 35  $E_R$  optical lattice. (b) The scattering lengths of the  $aa$  and  $bb$  interactions are plotted as a function of magnetic field, measured using lattice AM and shown in units of the Bohr radius  $a_0$ . Also shown as a bold dashed line is the  $ab$  scattering length, obtained using simultaneous hyperbolic fits to the RF spectroscopy and lattice AM data sets. The fits are shown as solid black lines. Dotted vertical lines indicate the position of a resonance.

in each hyperfine state. In previous studies, lattice amplitude modulation (AM) has been used to drive singlon-to-doublon conversion in the lowest Hubbard band, and the resonant frequency of this process has been associated with the on-site interaction energy in both repulsive [105] and attractive [94] single-component bosonic systems. Here the same technique is employed to map the on-site intra-species interactions of  ${}^7\text{Li}$  across a broad range of magnetic fields. The lattice depth is modulated by 30% peak-to-peak along the shallow dimension of a 35, 35, 20  $E_R$  optical lattice and the entropy added to the system is found by adiabatically ramping back to the BEC from the Mott insulator and measuring the recondensed fraction. While the system must remain in the Mott insulator in regions of magnetic field where the scattering length is negative in order to prevent the collapse of the atomic cloud, data taken above but close to the transition for either attractive or repulsive interactions display a bias towards higher frequency [105]. While this systematic bias prevents the collection of data for very small scattering lengths, limiting the accuracy of our determination of the background scattering length in each channel, the locations of the resonances themselves are not significantly affected.

Channel	$a_{bg}/a_0$	$\Delta$ (G)	$B_{res}$ (G)	$B_{res}$ (G)	$B_{res}$ (G)
			RF data only	Combined fit	Previous works
$aa$	-25.8(1.2)	-135.9(6.9)	737.58(10)	738.29(15)	738.2(2) <sup>[34]</sup> 737.8(2) <sup>[104]</sup> 736.97(7) <sup>[33]</sup>
$ab$	-29.8(1.3)	-90.5(4.0)	794.64(07)	794.59(12)	
$bb$	-23.0(1.4)	-14.9(0.9)	845.42(01)	845.45(02)	844.9(8) <sup>[34]</sup>
$bb$	-23.0(1.4)	-172.7(10.0)	893.34(12)	893.84(18)	893.7(4) <sup>[34]</sup>

Table 4.1: Parameters of the Feshbach resonances in the lowest two hyperfine states of  ${}^7\text{Li}$ , determined with a simultaneous fit to RF interaction and lattice AM spectroscopy data (except where specified otherwise). The reported errors in our measurements are  $1\sigma$  statistical uncertainties in the fit parameters. The AM data slightly bias the resonance positions derived from combined fits towards higher magnetic fields, possibly due to unaccounted-for systematics. As the RF data are influenced only by two-body, on-site effects rather than by many-body physics, the resonance *positions* are likely captured more accurately by the RF data alone.

### Extraction of the Feshbach resonance parameters

A simultaneous fit to both the RF differential interaction spectroscopy data and the lattice AM spectroscopy data determines the inter-species interaction energy  $U_{ab}$ , and extracts the parameters of the Feshbach resonances (see Fig. 4.9b). Feshbach resonances are dispersive features and can be parameterized as hyperbolae

$$a_s = a_{bg} \left( 1 - \sum_i \frac{\Delta^{(i)}}{B - B_{res}^{(i)}} \right) \quad (4.12)$$

with a background scattering length  $a_{bg}$ , width  $\Delta^{(i)}$ , and resonance location  $B_{res}^{(i)}$  [35, 106]. In order to provide a useful comparison with existing literature, the scattering lengths are calculated using (3.20):

$$\frac{1}{a_s} = \frac{4\pi\hbar^2}{m} \frac{1}{U} \int |\psi(r)|^4 d^3r \quad (4.13)$$

where  $U$  is the measured on-site interaction energy and  $\psi(r)$  is the calculated Wannier wavefunction on a site, given calibration of the lattice depth by inter-band parametric excitation. This approximation for  $\psi$  systematically biases the scattering lengths towards lower values because interactions modify the actual two-particle wavefunction by admixing higher bands, but the correction is not significant as long as  $|a_s|/a_{HO} \ll V^{1/4}/\sqrt{2\pi}$  where  $a_{HO}$  is the harmonic oscillator length on a site and  $V$  is the lattice depth in recoil units [107].<sup>3</sup> The complete Feshbach resonance spectrum for

<sup>3</sup>While the moderate scattering lengths considered here remain small enough that this approximation does not meaningfully affect the parameters of the hyperbolic fits, a more precise method would be to use the Busch solutions

the lowest two hyperfine states of  ${}^7\text{Li}$  is plotted in (Fig. 4.9b) and the parameters of the resonances can be found in Table 4.1.

This technique confirms the presence of a single resonance in the lowest hyperfine state, whose position is in good agreement with the most recent measurements made using RF-spectroscopy of molecular binding energies [34], although previous measurements made using the modification of in-trap condensate size due to the mean field energy of interactions have reported the resonance at slightly lower magnetic fields [33, 104, 108]. There is also a single resonance between the  $a$  and  $b$  states, previously unmeasured, whose parameters are particularly relevant for studies of two-component systems. Of interest is also the double resonance in the  $b$  state, studied previously using three-body atom loss [34, 109] and also RF-spectroscopy of molecular binding energies [34]. Compared to previous techniques, RF interaction spectroscopy allows for the exploration of the inter-species resonance. The method is as precise as RF spectroscopy of molecular binding energies, but does not require knowledge of the molecular potential in order to extract the scattering lengths.

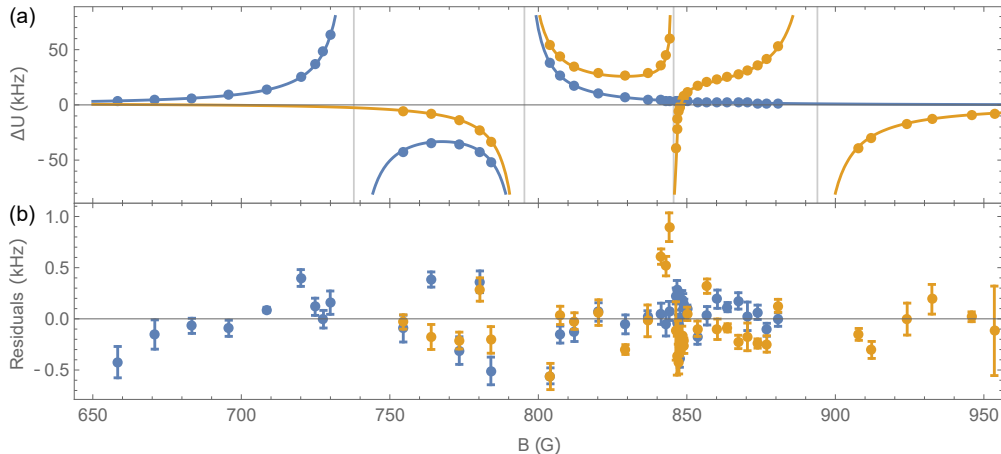


Figure 4.10: (a) Fit to a coupled channel calculation of the interaction energy differences  $U_{aa} - U_{ab}$  (blue) and  $U_{bb} - U_{ab}$  (gold). (b) The residuals of the fits. Figure reproduced with permission from [110].

### Fit to a coupled channel calculation

The interaction energy differences measured via RF-spectroscopy can also be used as the inputs to a coupled channel calculation, which allows for an especially precise determination of the scattering lengths at all magnetic fields, which does not suffer from the approximation inherent in the to the energies (4.11), as will be done in the next section.

hyperbolic parameterization, or the shortcomings of the lattice AM spectroscopy (especially at low lattice depths) [110]. By fitting scattering lengths obtained from modifying the Busch solution to the two-particle energies (4.11) so that the lowest two harmonic oscillator levels are separated by the same bandgap as the lowest two Bloch bands of the sinusoidal lattice potential, the resonance positions of table 4.2 are obtained. The fits are plotted in figure 4.10.

Channel	$B_{res}$ (G)
<i>aa</i>	737.883(31)
<i>ab</i>	795.307(160)
<i>bb</i>	845.499(14)
<i>bb</i>	893.989(195)

Table 4.2: Resonance positions obtained from a fit of the RF spectroscopy data to a coupled channel calculation. The errors represent  $2\sigma$  statistical uncertainty in the fit parameters.

### 4.3 Considerations for Spin-1 Experiments

The results of the interaction spectroscopy reveal that there is indeed a point near 848 G where the degeneracy condition for the spin-1 model is fulfilled, i.e. where  $D = 0$ . This point is not just a degeneracy point for super-exchange, however: it is also the point at which the interaction blockade on a single lattice site vanishes, and it is possible to rotate the total spin on a lattice site around the entire spin-1 Bloch sphere. Figure 4.11 shows an experimental realization of this effect, which is both a neat demonstration of interaction blockade physics and verification that such a degeneracy point exists in the Feshbach resonance spectrum of  ${}^7\text{Li}$ .

#### 4.3.1 Coherent Control and State Preparation

As much as RF interaction spectroscopy in a lattice enables precise measurements of scattering lengths, it is also a tool for state preparation and diagnostics. Starting with an  $n = 2$  Mott insulator in a single hyperfine state, one can prepare the fully paired,  $S^z = 0$  state  $|ab\rangle \equiv |0\rangle$  on every doubly-occupied lattice site by means of a  $\pi$ -pulse or a Landau-Zener sweep. Figure 4.11b demonstrates coherent preparation of this fully paired state, or Spin Mott state, which has a large gap and is a promising starting point for adiabatic state preparation, in analogy to the band insulator in fermions [25]. Full spin-sensitive diagnostics of doubly occupied sites can be realized using tran-

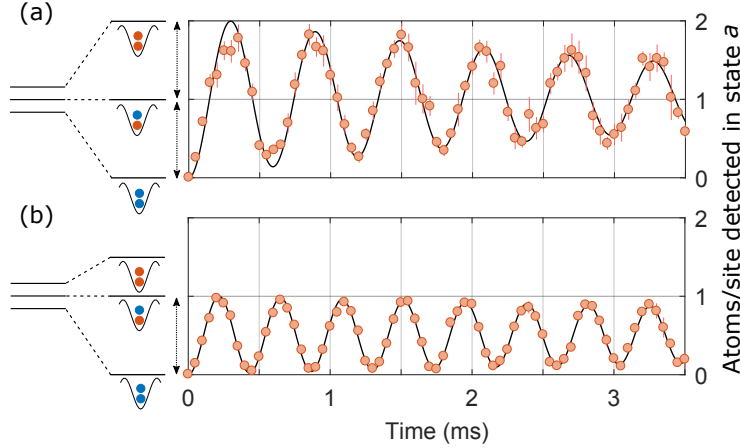


Figure 4.11: Rabi oscillations of doublons (a) exactly at and (b) far away from the magnetic field at which the interactions are degenerate, as in (4.9). The measured atom number is normalized to the total number of  $n = 2$  sites. The system is initially prepared in state  $b$  and the total number of atoms in state  $a$  is detected after applying a resonant RF drive. Decaying sinusoidal fits determine the Rabi frequencies to be  $1.68(4)$  kHz and  $2.30(1)$  kHz respectively, consistent with the expected  $\sqrt{2}$  ratio in Rabi frequency between resonant three-level and two-level systems. The time constant for the decoherence away from degeneracy is 10.2 ms. The oscillations in (a) seem to decay faster because this data was taken at the closest magnetic field to the degeneracy point which is permitted by the present resolution limit of our magnetic field setpoint, so that ultimately beating between two nearly-equal but off-resonant Rabi frequencies decreases the signal contrast.

sitions to a third hyperfine state, i.e. the  $c$  state, by selectively measuring the number of doublons in different configurations of hyperfine states at a magnetic field where the on-site interactions can be distinguished by RF transitions.

### 4.3.2 Magnetic Field Stability

The magnetic field is the parameter which tunes the scattering lengths, and through them, the ratio  $D/J$  that controls the phase of the system. Controlling both short term fluctuations (“noise”) and long term drift (“reproducibility”) of the magnetic field is therefore critical for quantum simulation experiments. The Feshbach resonances of  $^7\text{Li}$  begin above 700 G, so experiments will naturally involve high bias fields. These two requirements— detection of small variations and very high biases— require a stabilization system with large dynamic range.

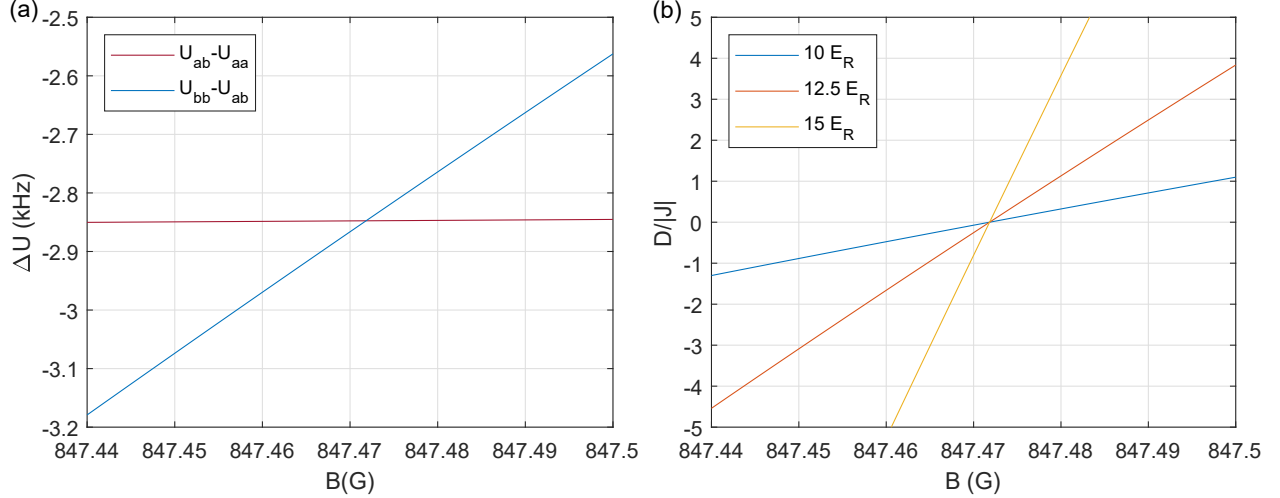


Figure 4.12: (a) Relative interactions plotted in the vicinity of the degeneracy point DGP, for a lattice depth of  $12.5 E_R$ . (b)  $D/J$  plotted for several values of the lattice depth in the strong-coupling direction (the transverse lattices are set to  $35 E_R$ ) for the same region of magnetic field. The values are calculated by using the Feshbach resonance parameters reported in table 4.1.

### Requirements for tuning $D/J$

The width of the magnetic field region where  $|D/J| < 1$  for the two-component  ${}^7\text{Li}$  system is sharply dependent upon the depth of the optical lattice  $V_0$  along the strong-coupling axis, mostly through the value of  $J$ . The depth  $V_0$  in turn depends on the location of the MI transition for doublons with the minimum  $U_{\text{on-site}}$ , because the system must be in the integer-occupancy regime in order for the mapping to the Heisenberg model to remain valid. At a reasonable lattice depth of  $10 E_R$  the width of the region in which  $|D/J| < 1$  is about 50 mG, but gets smaller very quickly at higher lattice depths (figure 4.12)b.

In order to make access to the regime in which  $D \approx 0$  accessible, the 20 mG of field noise detected via the interaction spectroscopy measurements requires some further improvement. Either the magnetic field stability can be improved, as will be discussed in the next section, or modifications can be made to the lattice setup. In 1D, where the coupling between chains should be zero, the transverse lattices can be made as deep as the available laser power allows, which increases  $U$  as  $V_0^{3/4}$  and in turn allows for a decrease of the lattice depth along the chain such that  $t_{\parallel}/U \sim \text{const.}$  If the transverse coupling is to be finite, the wavelength of the transverse lattice can be decreased, in which case  $U \sim k^{2/3}$  and again the depth along the chain can be decreased while still remaining in the MI. Both techniques would effectively broaden the range of magnetic field values for which

$$|D/J| < 1.$$

## Field control and feedback

If it were possible to measure the magnetic field at the position of the atoms, one could simply feed back on the bias current. As vacuum-compatible sensors with the required dynamic range (or bandwidth) have not yet— to the knowledge of this author— been invented, it is necessary to stitch together measurements from several sorts of sensors. To this effect, the large magnitude of the applied bias magnetic field presents both benefits and challenges. Because the relevant atomic effects depend on the magnitude of the magnetic field  $|B| = \sqrt{B_x^2 + B_y^2 + B_z^2}$ , experiments will be insensitive to changes in background field along the two axes perpendicular to the bias field, as their contributions to  $|B|$  will be suppressed by  $B_{\text{bias}}$ . Another advantage of high field is that the *relative* magnetic moments of the states at high field are only tens of kilohertz per Gauss, compared to megahertz per Gauss at zero field, so that in a spinful system magnetic field fluctuations mostly just rescale the total energy. In order to stabilize the bias field, a practical approach is to measure the applied current in a way that is insensitive to background magnetic fields. This task can be accomplished with Hall or fluxgate sensors that effectively measure the integral of the magnetic field along a closed loop; these can be placed around the conductor supplying the magnetic field coils. The approach of stabilizing the current, rather than the field itself, relies on the geometric stability of the coils with respect to the position of the atomic sample, which in turn depends on the thermal stability of the coil package and any hysteretic effects in the mounting hardware. In Helmholtz configuration, the bias field generated by a certain current varies by only  $+2 \text{ mG}/^\circ\text{C}$  for variations in the coil temperature (see section 2.2.3), and if any hysteresis in the field exists, its effects are too small to detect given other contributions to the noise, making the stabilization of current sufficient for this apparatus' needs. The remaining 20 mG of field noise comes rather from a combination of setpoint drift (due to the DAC used to control the fields, see section 2.2.4) and input offset drift of the error amplifier in the commercial feedback controller. Both issues are rather easily addressable via electronics upgrades.

In addition to stabilizing the applied bias field, fluctuations in the background field must be addressed as well. These can be as large as  $\pm 10 \text{ mG}$ , but are in general due to far-away sources and are quite uniform throughout the lab (the exception being 60 Hz fields, which are due mostly

to power supply transformers in lab equipment). The slow fluctuations in the component of the background field *parallel* to the applied bias can be measured by a field sensor such as fluxgate or Hall probe. The applied bias field presents an additional challenge, however, as one must be able to differentiate it from the background. In addition, near the chamber, the magnitude of the bias field is hundreds of Gauss, which will tend to overwhelm the dynamic range of any sensor.

The bias field falls off as  $1/r^3$ , so one might consider placing the sensor many meters from the chamber and subtracting a scaled bias field control signal from the measurement. This method has the disadvantage that the sensor must be far from the chamber. While the background fluctuations are presumed to be uniform in space, the distance between the sensor and the chamber prevent it from being used in a feedback configuration, where the compensation coils surround both the chamber and the sensor. Alternatively, one might place the sensor close to the chamber and wind a pair of compensation coils around it that cancel the fringing field of the bias. The advantage of sensor proximity can, however, be achieved with minimal additional complexity by recognizing that the fringing field of the bias coils is perpendicular to the coil axis everywhere on the surface of a double cone centered on the atoms and passing through the coils. This trick actually works better than one might expect: the sensor can be aligned by modulating the bias field and minimizing the response of the sensor. A small fluxgate sensor package (Bartington 690) with an active area of about  $4 \text{ mm}^2$  can be placed within 20 cm of the coils such that sensitivity to the bias field is already suppressed by five orders of magnitude. Thus a large set of coils enclosing both the sensor and the chamber can be used in a feedback configuration to cancel ambient field drifts down to the 0.5 mG level, with a bandwidth of about 100 Hz.

### 4.3.3 Decoherence Mechanisms

In order to have any hope of seeing coherent dynamics or ground states in this system, it must be the case that the super-exchange rate is much greater than the decoherence rate. In addition to the inter- and intra-band excitations (see section 3.3), the system is also susceptible to two- and three-body losses. Although state  $a$  is the hyperfine ground state, and therefore stable against spin-changing collisions, sites with two  $b$  atoms can decay to an  $a$  atom and a  $c$  atom, releasing tens of megahertz of Zeeman energy and ejecting the atoms from the lattice. Furthermore, sites with three particles can be lost due to three-atom recombination. Although the system is in the

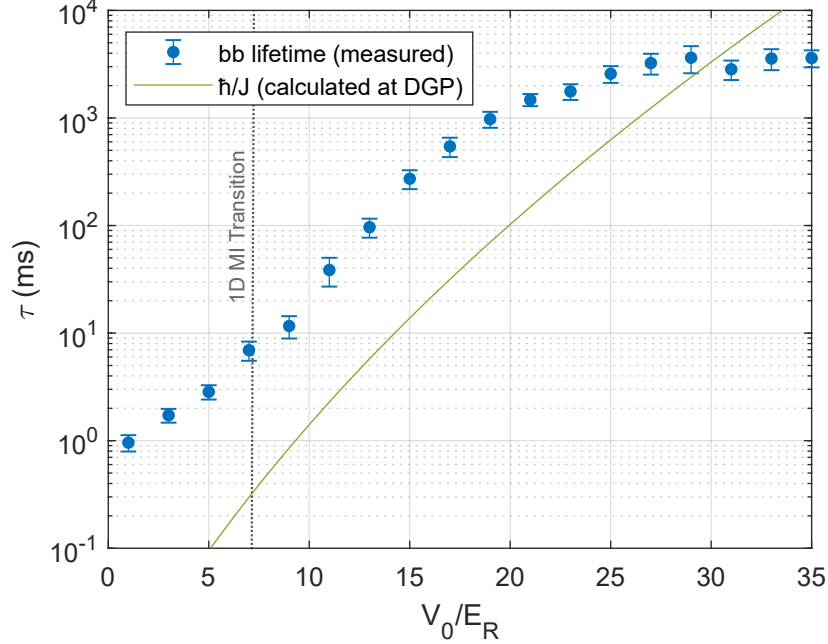


Figure 4.13: Measured lifetimes of  $bb$  sites and super-exchange period  $\hbar/J$  at a range of lattice depths, at the degeneracy point ( $B \approx 847.5$  G). The lattice depth  $V_{\text{crit}}$  at which the 1D MI transition takes place for the weakest interaction in the system ( $U_{aa}$ ) is indicated with a gray dotted line [111]. Because the MI lobes are rather more peaked in 1D than in 3D, the presence of external confinement means the superfluid phase is not really suppressed throughout the lattice until a depth of more than twice  $V_{\text{crit}}$  is reached.

$n=2$  MI state, there is a certain endemic three-body loss due to the finite admixture of triply occupied sites (see section 3.2.2), which in this context can be viewed as the intermediate step of super-exchange. These two loss mechanisms together form a fundamental limit to the lifetime of the system. Because the degeneracy point is very close to a  $bb$  resonance, the loss rate of  $bb$  sites should bound the total loss rate. Figure 4.13 shows the exponential decay constants measured for atom number in a lattice of  $bb$  sites at the degeneracy point, for a range of lattice depths. For comparison, the rate associated with the super-exchange parameter  $J/\hbar$  is also plotted, based on the Feshbach resonance parameters reported in 4.1. The loss rate scales like  $t^2$  for lattice depths below  $20 E_R$ , suggesting that below lifetimes of 1 s, the dominant loss process is three-body loss via coherently admixed triplons. Above lifetimes of 1 s, the lifetime is likely limited by noise-induced tunneling, resulting in band excitations and ultimately three-body loss. The three-body loss rate for  $b$ -state  ${}^7\text{Li}$  atoms at this magnetic field is unfortunately rather high [109]. For a range of lattice depths above the MI transition, however, the super-exchange rate is about 20 times higher than

the loss rate, suggesting that it will still be possible to observe effects arising from some tens of super-exchange events before the system decoheres completely. Encouragingly, the loss rate is likely to depend strongly on the local environment:  $ab$  doublons are less likely to decay if the neighboring sites contain  $aa$  or  $ab$  doublons than if the neighboring sites contain  $bb$  doublons.

#### 4.3.4 First Experiments

In light of these moderately encouraging results, some preliminary experiments can be performed which begin to explore the phase diagram of the spin-1 Heisenberg chain. The first step is to create a single-component MI in the  $b$  state with a core of doubly-occupied sites (given available lattice power, about 600 chains of 25 atoms each can be created, but the length can be increased by compensating external confinement along the tube axes with a repulsive potential, i.e. from a blue-detuned beam). Interaction blockades then permit RF preparation of the Spin Mott state in a deep lattice ( $J \approx 0$ ), in a region of magnetic field where this state is the ground state ( $D/|J| \gg 1$ ). It would then be possible to adiabatically sweep  $D/|J|$  in presence of weak inter-chain coupling in order to produce the  $xy$ -antiferromagnet. This sweep towards  $D/|J| \approx 1$  requires both lowering the magnetic bias field and lowering the lattice depth along the chains, which in principle can be accomplished in either order: lowering the magnetic bias field towards the DGP mostly decreases  $D$ , while lowering the lattice depth mostly increases  $|J|$ . Changing the field first will likely produce better results, as the magnetic field can be stabilized near the DGP while the sites are effectively isolated and the lifetime of the system is extremely long.

The formation of an  $xy$ -antiferromagnet from the Spin Mott phase should only require as many super-exchange events as the correlation length of the magnetically ordered state, which is anticipated to be a few sites. Thus, a second advantage of the Spin Mott phase as a starting point for adiabatic quantum simulation of this portion of the Heisenberg model phase diagram is that the phase transition does not require any long-range transport, which would be slow. Measurement of the correlation length would require techniques such as Bragg scattering [79, 112], noise correlations in time-of-flight [113, 114], or spin-resolved single-site imaging [115], but it may be possible to initially detect the presence of a phase transition simply by tracking the spin populations. Interaction blockades can again be used to distinguish  $aa$ ,  $ab$  and  $bb$  sites by flipping in an occupancy-dependent way one atom per site into a third state which can be imaged separately, e.g. the  $c$  state. In a

perfect Spin Mott, the population of doubly occupied sites should be exclusively  $ab$ , while in an  $xy$ -antiferromagnet the distribution of spins ought to be half  $ab$  sites and a quarter each of  $aa$  and  $bb$  (this is in contrast to a thermal distribution of spins, which ought to be one third of each state). It may even be possible to detect whether the transition is truly adiabatic by reversing the ramp of  $D/J$ , and measuring whether the distribution of spins respond accordingly. On the far side of the phase diagram, the  $z$ -antiferromagnet can be distinguished by the spin population being half each of  $aa$  and  $bb$ , with no  $ab$  sites at all.

Distinguishing the Haldane phase, however, is not nearly so straightforward. The spins are predicted to minimize the string order parameter

$$\mathcal{O}_{str}^\sigma \equiv \lim_{|j-k| \rightarrow 0} \left\langle S_j^\sigma \exp \left[ i\pi \sum_{j \leq l < k} S_l^\sigma \right] S_k^\sigma \right\rangle \quad (4.14)$$

which, as opposed to involving only products of nearest neighbors, is an inherently non-local measure [13, 116]. The sum in the exponent means that the order parameter is minimized only when every site containing a  $|+1\rangle$  spin is separated from a site containing a  $|-1\rangle$  spin by some number of  $|0\rangle$  sites (or none at all). Thus spin populations do not give an easily distinguishable picture of the state, and from the point of view of Bragg scattering, the Haldane state would look like the disappearance of magnetic ordering. In order to measure the long-range spatial correlations that string-ordering entails, one would really need the single-site resolution of a quantum gas microscope. An alternate approach to distinguishing the Haldane phase from the anti-ferromagnet would be to probe the system's response to a perturbation that creates spin waves, e.g. a magnetic field gradient. While the  $xy$ -antiferromagnet supports spin-waves, the Haldane phase does not, which leads to two different excitation spectra. The effect of these spin waves could be observed by returning (as adiabatically as possible) to the Spin Mott and observing the fidelity of the  $S^z = 0$  state.

## Chapter 5

# Conclusion and Outlook

This thesis has reviewed the design and construction of a general purpose, fast bosonic quantum simulator using  $^7\text{Li}$ . Because dynamics such as tunneling and super-exchange scale with the recoil energy, lighter atoms provide a significant advantage with respect to avoiding fundamental decoherence mechanisms like background gas collisions and off-resonant photon scattering, whose effects are independent of mass. Most technical sources of heating in the lattice, however, also scale with the mass (or with some higher power of the mass)— so that light atoms are a better choice if *and only if* such technical sources of noise can be mastered. In this respect light atoms present a dual challenge: not only are they more sensitive to noise, but the noise to which they are sensitive is at higher frequencies, so that techniques for mitigating it (i.e. feedback) can prove to be more technically demanding. Notwithstanding, the ratio of super-exchange rate to decoherence rate achieved by the  $^7\text{Li}$  quantum simulator at the time of this writing is large enough to enable experiments in many regimes. In addition, an experimental duty cycle of under ten seconds and robust, repeatable cooling performance should prove useful for densely sampling large parameter spaces in order to reveal the ground state phase diagrams of spin models and other Hamiltonians.

Aside from being the lightest bosonic alkali atom,  $^7\text{Li}$ 's interactions are eminently tunable, due to its Feshbach resonance spectrum. This thesis has discussed experiments in which the interactions between all three of the combinations of the lowest two hyperfine states were measured by exploiting interaction blockades in tightly-confining 3D optical lattice. The results of these measurements are the most precise achieved to date for  $^7\text{Li}$  by any method, and also constitute the first measurement of an inter-state resonance in  $^7\text{Li}$ . It has also been shown how the same interaction blockade effects may be used for coherent preparation of non-trivial combinations of spin states on a lattice site, and for spin- and number-sensitive readout of those combinations. Using these techniques in experiments requires the application of very large yet very stable magnetic fields. The requisite coils and feedback architecture have been described and characterized. As future experiments may further require the same high bias fields with extremely low curvature in order to achieve low external confinement along one or more axes, a prescription for how to create such fields with electromagnetic coils has been developed.

The particular case of the quasi-1D spin-1 Heisenberg model has been shown to provide an excellent proving ground for the unique strengths of the  $^7\text{Li}$  platform. Using the interaction spectroscopy data, a magnetic field has been found at which the combination of interactions in an  $n=2$

Mott insulator of  ${}^7\text{Li}$  implements the isotropic spin-1 Heisenberg model. Further, the surrounding magnetic field regions have been identified with differently ordered magnetic ground states, including  $z$ - and  $xy$ -antiferromagnets and a Spin Mott/paramagnet state, affording ample opportunities to study quantum phase transitions and to adiabatically prepare those states from a BEC. While some concerns about three-body losses remain, this system nonetheless provides a unique opportunity to explore magnetic ordering in bosons and perhaps study some aspects of symmetry-protected topological phases. If initial experiments monitoring population dynamics across the phase transitions seem promising, there may be sufficient arguments to upgrade the apparatus with single-site imaging, inspired by excellent results already achieved in fermionic Lithium [11, 115].

Of course, the  ${}^7\text{Li}$  platform can simulate many other models as well. Another promising avenue is the spin-1/2 system implemented by an  $n = 1$  Mott Insulator, which promises a similarly rich array of magnetically ordered ground states and phase transitions between them, and should provide an interesting bosonic counterpart to recent successes in simulations of fermionic systems. While platforms using fermionic atoms can only implement isotropic exchange interactions, bosons can probe anisotropic models as well, which considerably expands their phase space. Like the spin-1 system, the spin-1/2 system should provide opportunities to study spin dynamics and spin diffusion at high temperature, and adiabatic preparation of magnetically ordered ground states at lower temperatures. These and other experiments will hopefully contribute to the understanding of the truly fascinating quantum materials that exist in nature, and further to the use of adiabatic analog quantum computers as general tools for problem-solving.

# Bibliography

- [1] “Analog.” *Oxford English Dictionary (online ed.)* <https://en.oxforddictionaries.com/definition/analogue>, Accessed: 2019-04-29.
- [2] B. Ulmann, *Analog* (De Gruyter, Berlin, 2013).
- [3] C. Bissell, *IEEE Control Systems Magazine* **27**, 69 (2007).
- [4] “*The Antikythera Mechanism– Identifying its Place of Origin?*” *Electrum Magazine*. <http://www.electrummagazine.com/2015/07/the-antikythera-mechanism-identifying-its-place-of-origin/>, Accessed: 2019-04-29.
- [5] T. Freeth, Y. Bitsakis, X. Moussas, J. H. Seiradakis, A. Tselikas, H. Mangou, M. Zafeiropoulou, R. Hadland, D. Bate, A. Ramsey, M. Allen, A. Crawley, P. Hockley, T. Malzbender, D. Gelb, W. Ambrisco, and M. G. Edmunds, *Nature* **444**, 587 (2006).
- [6] J. H. Seiradakis and M. G. Edmunds, *Nature Astronomy* **2**, 35 (2018).
- [7] R. P. Feynman and R. Leighton, *What do ‘you’ care what other people think?: further adventures of a curious character: as told to Ralph Leighton* (Norton, New York, NY, 1985).
- [8] R. P. Feynman, *Int J Theor Phys* **21**, 476 (1982).
- [9] E. Grumbling and M. Horowitz, eds., *Quantum Computing: Progress and Prospects* (The National Academies Press, 2019).
- [10] W. Hofstetter, J. I. Cirac, P. Zoller, E. Demler, and M. D. Lukin, *Physical Review Letters* **89** (2002).
- [11] A. Mazurenko, C. S. Chiu, G. Ji, M. F. Parsons, M. Kanász-Nagy, R. Schmidt, F. Grusdt, E. Demler, D. Greif, and M. Greiner, *Nature* **545**, 462 (2017).
- [12] F. D. M. Haldane, *Phys. Rev. Lett.* **50**, 1153 (1983).
- [13] F. Pollmann, E. Berg, A. M. Turner, and M. Oshikawa, *Phys. Rev. B* **85**, 075125 (2012).
- [14] E. Manousakis, *Reviews of Modern Physics* **63**, 1 (1991).
- [15] S. Trebst, U. Schollwöck, M. Troyer, and P. Zoller, *Physical Review Letters* **96** (2006).
- [16] L. W. Cheuk, M. A. Nichols, K. R. Lawrence, M. Okan, H. Zhang, E. Khatami, N. Trivedi, T. Paiva, M. Rigol, and M. W. Zwierlein, *Science* **353**, 1260 (2016).
- [17] S. Istrail, in *Proceedings of the thirty-second annual ACM symposium on theory of computing - STOC '00* (2000).
- [18] A. Lucas, *Frontiers in Physics* **2** (2014).
- [19] J.-R. Li, J. Lee, W. Huang, S. Burchesky, B. Shteynas, F. Ç. Top, A. O. Jamison, and W. Ketterle, *Nature* **543**, 91 (2017).

- [20] E. Urban, T. A. Johnson, T. Henage, L. Isenhower, D. D. Yavuz, T. G. Walker, and M. Saffman, *Nature Physics* **5**, 110 (2009).
- [21] H. Weimer, M. Müller, I. Lesanovsky, P. Zoller, and H. P. Büchler, *Nature Physics* **6**, Article, 382 EP (2010).
- [22] H. Bernien, S. Schwartz, A. Keesling, H. Levine, A. Omran, H. Pichler, S. Choi, A. S. Zibrov, M. Endres, M. Greiner, V. Vuletic, and M. D. Lukin, *Nature* **551**, Article, 579 (2017).
- [23] S. Trotzky, P. Cheinet, S. Fölling, M. Feld, U. Schnorrberger, A. M. Rey, A. Polkovnikov, E. A. Demler, M. D. Lukin, and I. Bloch, *Science* **319**, 295 (2008).
- [24] E. Farhi, J. Goldstone, S. Gutmann, and M. Sipser, “Quantum Computation by Adiabatic Evolution”, Unpublished, 2000.
- [25] J. Schachenmayer, D. M. Weld, H. Miyake, G. A. Siviloglou, W. Ketterle, and A. J. Daley, *Phys. Rev. A* **92**, 041602 (2015).
- [26] M. H. Anderson, J. R. Ensher, M. R. Matthews, C. E. Wieman, and E. A. Cornell, *Science* **269**, 198 (1995).
- [27] Davis, K. B. and Mewes, M. -O. and Andrews, M. R. and van Druten, N. J. and Durfee, D. S. and Kurn, D. M. and Ketterle, W., *Phys. Rev. Lett.* **75**, 3969 (1995).
- [28] C. Kittel and H. Krömer, *Thermal physics; 2nd ed.* (Freeman, New York, NY, 1980).
- [29] N. F. Mott, *Proceedings of the Physical Society. Section A* **62**, 416 (1949).
- [30] M. Greiner, O. Mandel, T. Esslinger, T. W. Hänsch, and I. Bloch, *Nature* **415**, 39 (2002).
- [31] C. C. Bradley, C. A. Sackett, and R. G. Hulet, *Phys. Rev. Lett.* **78**, 985 (1997).
- [32] C. Chin, R. Grimm, P. Julienne, and E. Tiesinga, *Rev. Mod. Phys.* **82**, 1225 (2010).
- [33] S. E. Pollack, D. Dries, M. Junker, Y. P. Chen, T. A. Corcovilos, and R. G. Hulet, *Phys. Rev. Lett.* **102**, 090402 (2009).
- [34] N. Gross, Z. Shotan, O. Machtey, S. Kokkelmans, and L. Khaykovich, *Comptes Rendus Physique* **12**, 4 (2011).
- [35] P. S. Julienne and J. M. Hutson, *Physical Review A* **89** (2014).
- [36] J. Amato-Grill, N. Jepsen, I. Dimitrova, W. Lunden, and W. Ketterle, *Physical Review A* **99** (2019).
- [37] D. Das and V. Natarajan, *Phys. Rev. A* **75**, 052508 (2007).
- [38] W. I. McAlexander, E. R. I. Abraham, and R. G. Hulet, *Phys. Rev. A* **54**, R5 (1996).
- [39] J. J. Sakurai, *Modern quantum mechanics; rev. ed.* (Addison-Wesley, Reading, MA, 1994).
- [40] J. Dalibard, in *Proceedings of the international school of physics - enrico fermi*, Vol. 321 (1999), p. 14.
- [41] E. Abraham, W. McAlexander, C. Sackett, and R. G. Hulet, *Physical Review Letters* **74**, 1315 (1995).
- [42] J. M. Gerton, C. A. Sackett, B. J. Frew, and R. G. Hulet, *Phys. Rev. A* **59**, 1514 (1999).
- [43] E. A. Burt, R. W. Ghrist, C. J. Myatt, M. J. Holland, E. A. Cornell, and C. E. Wieman, *Phys. Rev. Lett.* **79**, 337 (1997).
- [44] D. M. Stamper-Kurn, M. R. Andrews, A. P. Chikkatur, S. Inouye, H.-J. Miesner, J. Stenger, and W. Ketterle, *Phys. Rev. Lett.* **80**, 2027 (1998).

- [45] U Schunemann, H Engler, R. Grimm, M. Weidemüller, and M Zielonkowski, Review of Scientific Instruments **70**, 242 (1999).
- [46] H. J. Metcalf and P. Straten, *Laser cooling and trapping*, Graduate Texts in Contemporary Physics (Springer, New York, 1999).
- [47] J. D. Jackson, *Classical electrodynamics; 2nd ed.* (Wiley, New York, NY, 1975).
- [48] W. Ketterle, K. B. Davis, M. A. Joffe, A. Martin, and D. E. Pritchard, Phys. Rev. Lett. **70**, 2253 (1993).
- [49] C. B. A. a V. P. Itkin and M. K. Horrigan, Canadian Metallurgical Quarterly **23**, 309 (1984).
- [50] M. R. Tarbutt, New Journal of Physics **17**, 015007 (2015).
- [51] P. He, P. M. Tengdin, D. Z. Anderson, A. M. Rey, and M. Holland, Physical Review A **95** (2017).
- [52] G. Morigi, J. Eschner, and C. H. Keitel, Phys. Rev. Lett. **85**, 4458 (2000).
- [53] A. Aspect, E. Arimondo, R. Kaiser, N. Vansteenkiste, and C. Cohen-Tannoudji, Phys. Rev. Lett. **61**, 826 (1988).
- [54] M Weidemüller, T Esslinger, M. A Olshanii, A Hemmerich, and T. W Hänsch, Europhysics Letters (EPL) **27**, 109 (1994).
- [55] D. Boiron, C. Triché, D. R. Meacher, P. Verkerk, and G. Grynberg, Phys. Rev. A **52**, R3425 (1995).
- [56] G. D. Bruce, E Haller, B Peaudecerf, D. A. Cotta, M Andia, S Wu, M. Y. H. Johnson, B. W. Lovett, and S Kuhr, Journal of Physics B: Atomic, Molecular and Optical Physics **50**, 095002 (2017).
- [57] A. T. Grier, I. Ferrier-Barbut, B. S. Rem, M. Delehaye, L. Khaykovich, F. Chevy, and C. Salomon, Phys. Rev. A **87**, 063411 (2013).
- [58] W. Ketterle and N. V. Druten, in *Advances in atomic, molecular, and optical physics*, Vol. 37, edited by B. Bederson and H. Walther (Academic Press, 1996), pp. 181 –236.
- [59] H. Wu, E. Arimondo, and C. J. Foot, Phys. Rev. A **56** (1997).
- [60] G. Bird, *Molecular gas dynamics and the direct simulation of gas flows*, Molecular Gas Dynamics and the Direct Simulation of Gas Flows v. 1 (Clarendon Press, 1994).
- [61] R. Grimm, M. Weidemüller, and Y. B. Ovchinnikov, in *Advances in atomic, molecular, and optical physics*, Vol. 42, edited by B. Bederson and H. Walther (Academic Press, 2000), pp. 95 –170.
- [62] C. Kittel, *Introduction to Solid State Physics; 8th ed.* (Wiley, Hoboken, NJ, 2005).
- [63] N. W. Ashcroft and N. D. Mermin, *Solid state physics* (Holt, Rinehart and Winston, New York, NY, 1976).
- [64] W. Kohn, Phys. Rev. **115**, 809 (1959).
- [65] D. Jaksch, C. Bruder, J. I. Cirac, C. W. Gardiner, and P. Zoller, Phys. Rev. Lett. **81**, 3108 (1998).
- [66] D. Jaksch and P. Zoller, Annals of Physics **315**, Special Issue, 52 (2005).
- [67] I. Bloch, J. Dalibard, and W. Zwerger, Rev. Mod. Phys. **80**, 885 (2008).
- [68] D. van Oosten, P. van der Straten, and H. T. C. Stoof, Phys. Rev. A **63**, 053601 (2001).

- [69] F. Gerbier, A. Widera, S. Fölling, O. Mandel, T. Gericke, and I. Bloch, *Physical Review Letters* **95** (2005).
- [70] W. S. Bakr, A. Peng, M. E. Tai, R. Ma, J. Simon, J. I. Gillen, S. Fölling, L. Pollet, and M. Greiner, *Science* **329**, 547 (2010).
- [71] K. Winkler, G. Thalhammer, F. Lang, R. Grimm, J. Hecker Denschlag, A. J. Daley, A. Kantian, H. P. Büchler, and P. Zoller, *Nature* **441**, 853 (2006).
- [72] L. Xia, L. A. Zundel, J. Carrasquilla, A. Reinhard, J. M. Wilson, M. Rigol, and D. S. Weiss, *Nature Physics* **11**, 316 (2015).
- [73] S. Blatt, A. Mazurenko, M. F. Parsons, C. S. Chiu, F. Huber, and M. Greiner, *Phys. Rev. A* **92**, 021402 (2015).
- [74] M. E. Gehm, K. M. O'Hara, T. A. Savard, and J. E. Thomas, *Phys. Rev. A* **58**, 3914 (1998).
- [75] H. Pichler, J. Schachenmayer, A. J. Daley, and P. Zoller, *Phys. Rev. A* **87**, 033606 (2013).
- [76] T. Müller, S. Fölling, A. Widera, and I. Bloch, *Phys. Rev. Lett.* **99**, 200405 (2007).
- [77] J. Bechhoefer, *Reviews of Modern Physics* **77**, 783 (2005).
- [78] L.-M. Duan, E. Demler, and M. D. Lukin, *Phys. Rev. Lett.* **91**, 090402 (2003).
- [79] R. A. Hart, P. M. Duarte, T.-L. Yang, X. Liu, T. Paiva, E. Khatami, R. T. Scalettar, N. Trivedi, D. A. Huse, and R. G. Hulet, *Nature* **519**, 211 (2015).
- [80] P. T. Brown, D. Mitra, E. Guardado-Sanchez, P. Schauß, S. S. Kondov, E. Khatami, T. Paiva, N. Trivedi, D. A. Huse, and W. S. Bakr, *Science* **357**, 1385 (2017).
- [81] E. Altman, W. Hofstetter, E. Demler, and M. D. Lukin, *New Journal of Physics* **5**, 113 (2003).
- [82] C. Cohen-Tannoudji, J. Dupont-Roc, and G. Grynberg, *Atom-photon interactions: basic processes and applications* (Wiley, New York, NY, 1992).
- [83] I. Affleck, T. Kennedy, E. H. Lieb, and H. Tasaki, *Phys. Rev. Lett.* **59**, 799 (1987).
- [84] I. Affleck, T. Kennedy, E. H. Lieb, and H. Tasaki, *Comm. Math. Phys.* **115**, 477 (1988).
- [85] I Affleck, *Journal of Physics: Condensed Matter* **1**, 3047 (1989).
- [86] K. Wierschem and P. Sengupta, *Modern Physics Letters B* **28** (2015).
- [87] X. Chen, Z.-C. Gu, Z.-X. Liu, and X.-G. Wen, *Science* **338**, 1604 (2012).
- [88] T. Senthil, *Annual Review of Condensed Matter Physics* **6**, 299 (2015).
- [89] M. den Nijs and K. Rommelse, *Phys. Rev. B* **40**, 4709 (1989).
- [90] Z.-C. Gu and X.-G. Wen, *Phys. Rev. B* **80**, 155131 (2009).
- [91] T. Sakai and M. Takahashi, *Phys. Rev. B* **42**, 4537 (1990).
- [92] Z.-X. Gong, M. F. Maghrebi, A. Hu, M. Foss-Feig, P. Richerme, C. Monroe, and A. V. Gorshkov, *Phys. Rev. B* **93**, 205115 (2016).
- [93] K. Wierschem and P. Sengupta, *Phys. Rev. Lett.* **112**, 247203 (2014).
- [94] M. J. Mark, E. Haller, K. Lauber, J. G. Danzl, A. Janisch, H. P. Büchler, A. J. Daley, and H.-C. Nägerl, *Phys. Rev. Lett.* **108**, 215302 (2012).
- [95] M. Lysebo and L. Veseth, *Phys. Rev. A* **81**, 032702 (2010).

- [96] C. Senko, P. Richerme, J. Smith, A. Lee, I. Cohen, A. Retzker, and C. Monroe, *Physical Review X* **5** (2015).
- [97] I. Cohen, P. Richerme, Z.-X. Gong, C. Monroe, and A. Retzker, *Physical Review A* **92** (2015).
- [98] T. Busch, B.-G. Englert, K. Rzażewski, and M. Wilkens, *Foundations of Physics* **28**, 549 (1998).
- [99] G. K. Campbell, J. Mun, M. Boyd, P. Medley, A. E. Leanhardt, L. G. Marcassa, D. E. Pritchard, and W. Ketterle, *Science* **313**, 649 (2006).
- [100] W. S. Bakr, P. M. Preiss, M. E. Tai, R. Ma, J. Simon, and M. Greiner, *Nature* **480**, 500 (2011).
- [101] D. Jaksch, J. I. Cirac, P. Zoller, S. L. Rolston, R. Côté, and M. D. Lukin, *Phys. Rev. Lett.* **85**, 2208 (2000).
- [102] Y. O. Dudin, L. Li, F. Bariani, and A. Kuzmich, *Nature Physics* **8**, 790 (2012).
- [103] E. Arimondo, M. Inguscio, and P. Violino, *Rev. Mod. Phys.* **49**, 31 (1977).
- [104] N. Navon, S. Piatecki, K. Günter, B. Rem, T. C. Nguyen, F. Chevy, W. Krauth, and C. Salomon, *Phys. Rev. Lett.* **107**, 135301 (2011).
- [105] C. Schori, T. Stöferle, H. Moritz, M. Köhl, and T. Esslinger, *Phys. Rev. Lett.* **93**, 240402 (2004).
- [106] K. Jachymski and P. S. Julienne, *Phys. Rev. A* **88**, 052701 (2013).
- [107] H. P. Büchler, *Phys. Rev. Lett.* **104**, 090402 (2010).
- [108] S. E. Pollack, D. Dries, and R. G. Hulet, *Science* **326**, 1683 (2009).
- [109] Z. Shotan, O. Machtey, S. Kokkelmans, and L. Khaykovich, *Phys. Rev. Lett.* **113**, 053202 (2014).
- [110] T. Secker and S. J. J. M. F. Kokkelmans, “Private communication”.
- [111] I. Danshita and A. Polkovnikov, *Phys. Rev. A* **84**, 063637 (2011).
- [112] H. Miyake, G. A. Siviloglou, G. Puentes, D. E. Pritchard, W. Ketterle, and D. M. Weld, *Phys. Rev. Lett.* **107**, 175302 (2011).
- [113] E. Altman, E. Demler, and M. D. Lukin, *Phys. Rev. A* **70**, 013603 (2004).
- [114] S. Fölling, F. Gerbier, A. Widera, O. Mandel, T. Gericke, and I. Bloch, *Nature* **434**, 481 (2005).
- [115] M. Boll, T. A. Hilker, G. Salomon, A. Omran, J. Nespolo, L. Pollet, I. Bloch, and C. Gross, *Science* **353**, 1257 (2016).
- [116] E. Berg, E. G. D. Torre, T. Giamarchi, and E. Altman, *Physical Review B* **77** (2008).